1995

A predictive model of the HF noise environment at satellite heights

Marisa McCoy
Iowa State University

Recommended Citation

McCoy, Marisa, "A predictive model of the HF noise environment at satellite heights " (1995). *Retrospective Theses and Dissertations*. 11030.
https://lib.dr.iastate.edu/rtd/11030

INFORMATION TO USERS

This manuscript has been reproduced from the microfilm master. UMI films the text directly from the original or copy submitted. Thus, some thesis and dissertation copies are in typewriter face, while others may be from any type of computer printer.

The quality of this reproduction is dependent upon the quality of the copy submitted. Broken or indistinct print, colored or poor quality illustrations and photographs, print bleedthrough, substandard margins, and improper alignment can adversely affect reproduction.

In the unlikely event that the author did not send UMI a complete manuscript and there are missing pages, these will be noted. Also, if unauthorized copyright material had to be removed, a note will indicate the deletion.

Oversize materials (e.g., maps, drawings, charts) are reproduced by sectioning the original, beginning at the upper left-hand corner and continuing from left to right in equal sections with small overlaps. Each original is also photographed in one exposure and is included in reduced form at the back of the book.

Photographs included in the original manuscript have been reproduced xerographically in this copy. Higher quality 6" x 9" black and white photographic prints are available for any photographs or illustrations appearing in this copy for an additional charge. Contact UMI directly to order.

UMI

A Bell & Howell Information Company
300 North Zeeb Road, Ann Arbor, MI 48106-1346 USA
313/761-4700 800/521-0600

A predictive model of the HF noise environment at satellite heights

by

Marisa McCoy

A Dissertation Submitted to the
Graduate Faculty in Partial Fulfillment of the
Requirements for the Degree of
DOCTOR OF PHILOSOPHY

Department: Electrical and Computer Engineering
Major: Electrical Engineering (Electromagnetics)

Approved:

Signature was redacted for privacy.

In Charge of Major Work

Signature was redacted for privacy.

For the Major Department

Signature was redacted for privacy.

For the Graduate College

Iowa State University
Ames, Iowa

1995

UMI Number: 9606637

UMI
300 North Zeeb Road
Ann Arbor, MI 48103

A predictive model of the HF noise environment at satellite heights

Marisa McCoy

Major Professor: John P. Basart
Iowa State University

The radio noise background is an area of continuing research and measurement. In many cases, the background noise becomes the primary limiting factor in a communication system's sensitivity. The issue of HF (1-30 MHz) interference from terrestrial sources is especially pertinent to space-based low-frequency radio astronomy. Radio astronomy observations in the HF portion of the electromagnetic spectrum could result in new insights into astrophysical processes. However, this particular part of the spectrum is mostly inaccessible from the ground due to the effects of the Earth's ionosphere.

The objective of this research is to determine to what extent terrestrial radio sources would interfere with an Earth-orbiting interferometer. The end result is a first-order global model of ionospheric HF propagation, with inputs for the ionosphere's characteristics, source characteristics, and appropriate perturbations. The model output is a simulated spectrum of the interference with respect to the geographical subsatellite point. The development emphasis has been on reasonable first-order approximations to the global wave propagation problem, since currently, no predictive estimates exist.

The model predictions indicate that it is possible to perform interferometry from Earth orbit at the desired frequencies under certain cases. However, to further develop the modeling completed here, a campaign to collect additional interference data and define the necessary technical characteristics of an Earth-orbiting interferometer is strongly recommended.

DEDICACIÓN

Dedico esta obra a mis estimados padres, quienes me siempre ayudaron, y a mi corazón y alma, mi esposo.

TABLE OF CONTENTS

Page

LIST OF FIGURES

LIST OF TABLES

LIST OF ACRONYMS

AKR:	Auroral Kilometric Radiation
AMPTE/IRM:	Active Magnetospheric Particle Tracer Explorer/Ion Release Module
AWS:	Air Weather Service (Air Force)
CCIR:	International Radio Consultative Committee (translation from French)
DMSP:	Defense Meteorological Satellite Program
FDTD:	Finite Difference Time Domain
foE:	Ordinary mode critical frequency of the ionospheric E layer
foF2:	Ordinary mode critical frequency of the ionospheric F2 layer
foF1:	Ordinary mode critical frequency of the ionospheric F1 layer
HF:	High Frequency
ICED:	Ionospheric Conductivity & Electron Density
IPM:	InterPlanetary Medium
IRI-90:	International Reference Ionosphere (1990 version)
ITF:	Ionospheric Transfer Function
ITS:	Institute for Telecommuncation Sciences
ITU:	International Telecommunications Union
LFSA:	Low Frequency Space Array
LT:	Local Time
PDM:	Phase screen Diffraction Method
OHFRIM:	Orbiting High FRequency Interference Monitor
OTH:	Over The Horizon
RAE:	Radio Astronomy Explorer
R_E:	Radius of the Earth $\equiv$ 6371 km

RV:	Ryle-Vonberg
SCET:	SpaceCraft Event Time
TEC:	Total Electron Content
TID:	Transient Ionospheric Disturbance
UT:	Universal Time (equivalent to Greenwich Mean Time)
VLBI:	Very Long Baseline Interferometry
VLA:	Very Large Array

ACKNOWLEDGMENTS

This work was performed under NASA Training Grant Number NGT-51020 as part of the NASA Graduate Student Researchers Program at the Goddard Space Flight Center. I am most grateful to Dr. Gerald Soffen of the University Programs Office at NASA Goddard for funding my research these past two years. I also thank my advisor at Iowa State University, John P. Basart, for his support and encouragement throughout the process. I especially want to acknowledge the following people for the tremendous assistance they have given to me:

-- William Farrell, my Center advisor at NASA, and his colleagues Michael Kaiser and Michael Desch of the Laboratory for Extraterrestrial Physics, for their encouragement, suggestions, and access to data from WIND.

-- Paul E. Argo, Robert Massey, and Daniel Holden of the Space and Atmospheric Sciences Group at Los Alamos National Labs, for their insight on ionospheric propagation and ray-tracing, which has played a big role in the completion of this work. I am especially grateful for the opportunity they gave me to work with them at Los Alamos during the Fall of 1994.

-- Roland T. Tsunoda at Stanford Research Institute, International, for both his helpful discussions on ionospheric irregularities and providing research material.

-- L. J. Nickisch of Mission Research Corp. for his help with the random media portion of this research, including his suggestions on the use of the phase-screen diffraction method.

-- Kurt Weiler, Namir Kassim, and Andy Clegg of the Naval Research Laboratory, for their discussions and information on HF radio astronomy and the LFSA.

Ryan Marotz very patiently helped me sort through and analyze the WIND data set as part of his undergraduate Honors project at Iowa State University.

CHAPTER 1
INTRODUCTION

1.1 Research Objective

The radio noise background in the Earth's environment is an area of continuing research and measurement. In many cases, the background noise becomes the primary limiting factor in science experiments and communication systems' sensitivity. The issue of the HF (1-30 MHz) background noise at satellite heights is especially pertinent to space-based low-frequency radio astronomy. High resolution radio astronomy observations in the HF portion of the electromagnetic spectrum will lead to new insights into astrophysical processes. However, this particular part of the spectrum is mostly inaccessible from the ground due to the effects of the Earth's ionosphere.

Even though radio astronomy started in the HF band with Karl Jansky's pioneering measurements at 20.5 MHz, the bulk of the effort in radio astronomy has moved to higher frequencies. In fact, radio astronomy has now exploited the majority of the electromagnetic spectrum, with the distinct exception of the HF bands. The two primary reasons for this move away from the HF part of the spectrum are:

1. ionospheric effects -- the phase dispersion, Faraday rotation, and group path delay scale as the inverse frequency squared; other effects scale with the inverse of frequency (Goodman and Aarons, 1990). The ionosphere also exhibits temporal and spatial variations that defeat most attempts at very long baseline interferometry (VLBI) at HF (Basart, 1988).

2. resolution -- Since resolution is proportional to λ/D (where λ is the wavelength and D is the interferometer's baseline length) high resolution imaging can be performed with more compact arrays at higher frequencies.

Supporters of low frequency radio astronomy desire image resolutions on the order of 1 arc second. Such high resolution imaging would require baselines on the order of several thousand kilometers. At these distances, ionospheric horizontal gradients become a concern (see #1 above).

Since the ionosphere is the natural limiting factor for ground-based low frequency radio astronomy, one possible solution is to observe from a location above the Earth's ionosphere, thereby avoiding most of the absorption and phase distortions from the ionosphere. Three alternatives exist: high-Earth orbit, lunar orbit, and lunar surface. An Earth-orbiting low frequency interferometer would be the most technically feasible and cost effective of the three choices. However, in the 1-30 MHz band of interest, the ionosphere is neither a perfect reflector nor is it a perfect transmission medium. The same ionospheric variability that corrupts ground-based observations may allow terrestrial noise to "leak" or break through, making the detection of faint sources difficult. Such an occurrence would essentially raise the background noise level of the interferometer, reducing its sensitivity or introducing spurious signals into the receiver. A lunar-orbiting or lunar-based interferometer would be preferable because the interference would be negligible on the moon's far side. However, cost and technical constraints necessitate examining the potential usefulness of an Earth-orbiting interferometer.

The objective of this research is to determine to what extent terrestrial radio noise would interfere with an Earth-orbiting interferometer. The end result is a first-order global model of ionospheric wave propagation in the 1 - 30 MHz frequency region, with inputs for the ionosphere's characteristics, source characteristics, and appropriate perturbations. The output is a statistically predicted noise intensity with respect to frequency and location above the Earth at satellite heights. The emphasis in the model development is to come up with reasonable first-order approximations to the global wave propagation problem, since currently, no predictive estimates exist (at least in the "white" or unclassified world). The HF noise levels have not been seriously addressed for a number of reasons:

- The overwhelming majority of HF system development occurs for ground-based broadcasting or point-to-point communications;
- Most satellite-based HF systems operate from a "surveillance" perspective, so what we consider HF "noise" or interference are actually the desired signals for these systems.

1.2 Space-Based Radio Astronomy Goals

Since the overall research goal is to develop a predictive HF noise model at satellite heights for use in space-based radio astronomy, the requirements for an orbiting interferometer can be used as guidelines for determining the model's suitability. Observations in the HF part of the electromagnetic spectrum will bring astronomy to the fundamental physical limit below which the Milky Way becomes optically thick (opaque). Although single radio telescopes have operated at the higher end of the HF spectrum, attempts at HF interferometry have resulted in limited success (Basart, et al., 1995). While UHF and microwave frequencies are most commonly used for interferometric radio astronomy observations, there is work in progress in the 100 to 300 MHz frequency range. The Very Large Array (VLA) in New Mexico currently has some rudimentary capability for 74 MHz observations (Kassim, et al., 1993), and more antennas are being retrofitted for this capability. Kassim, et al. (1993) have conducted 74 MHz VLA observations and corrected for the errors due to ionospheric refraction using a dual frequency phase referencing technique, where a reference frequency much higher (330 MHz) than the observing frequency was used during simultaneous observations. Most of the phase fluctuations observed were not due to differential path lengths in the background ionosphere, but rather were caused by horizontal gradients produced by ionospheric disturbances (Kassim, et al., 1993). This phase referencing technique breaks down as the observing frequency decreases because of the nonlinear ($\propto 1/f^2$) phase dispersion in the ionosphere. Also, as the frequency decreases, the ray path becomes significantly more refracted, so that the ray encounters more of the ionosphere. As this happens, the following effects become important:

- Absorption due to particle collisions increases sharply for highly refracted ray paths. In many cases it can be greater than 10 dB.
- Scattering from ionospheric irregularities becomes non-negligible. At night, when the ionosphere is relatively transparent, ionospheric "plumes" are a regular occurrence at mid-latitudes. In the daytime, traveling ionosphere disturbances (TIDs) can cause large phase errors. The wavefront phase and amplitude become so distorted that even the strongest calibration sources become decorrelated (Basart, 1988).

These two effects are the primary reasons for the paucity of observations below 30 MHz and for the difficulties in performing HF interferometry.

The Low Frequency Space Array (LFSA)[1] proposed by a joint team from the Naval Research Lab, NASA Goddard Space Flight Center, and several other organizations would image the entire sky from space at frequencies below 30 MHz (Weiler, et al., 1994). There are a number of scientific programs of interest to the radio astronomy community that would be performed by the LFSA. These will be described briefly in the following paragraphs.

---

[1] The nomenclature is unfortunate, in that the part of the spectrum called high frequency -- HF -- by the radio engineers is termed low frequency by astronomers.

The Sun and Jupiter appear to be the brightest radio sources in the sky, because of their proximity. Extensive Earth- and space-based observations have revealed the complexity and large quantity of Jupiter's nonthermal emissions. No direct information on the location and structure of the Jovian emission exists because of the large amount of refraction introduced by the Earth's ionosphere. Even under the best terrestrial observing conditions, ionospheric effects limit measurements of Jupiter's emissions to above 7 MHz (Carr and Wang, 1990). To date, space-based observations have been confined to individual spacecraft (RAE-1, IMP, ISEE 3, Galileo, Voyager 1 and 2). The hectometric radiation (radiation whose wavelength is about 100 m), which nominally falls within 0.3 - 3 MHz, appears to be correlated with the Jovian rotation, unlike higher and lower frequency radiation components which appear more sporadically. Long term observations of Jupiter's radiation could provide clues on the secular variations of its magnetic field, as well as facilitate the development of a complete theory of the hectometric radiation and its relation to the solar wind.

Ground-based solar observations are also severely limited by ionospheric effects. According to Dulk (1990), almost no solar radiation observations exist between 2 MHz (the upper limit of space-based measurements) and 20 MHz (the lower limit of ground-based measurements). The flux and brightness temperature of the quiet Sun becomes harder to measure at frequencies below about 100 MHz because of the decreased contrast with the galactic background radiation level. According to Dulk, no true images of solar sources exist below 26 MHz. There are also no measurements of solar flux or polarization in the 2 - 20 MHz region, so little is known that could connect the processes dominant at higher frequencies to those observed at lower frequencies. If imaging data at frequencies below about 25 MHz were available, many of these questions could be resolved.

Cosmic rays represent the most energetic form of matter, and permeate our Galaxy, where they form a relativistic component of the interstellar medium. However, the origin of cosmic rays is still unsolved. This particular problem could be the most fundamental issue addressed by the LFSA. Observations at HF can complement gamma ray studies. The population of 150 MeV cosmic rays which produces the cosmic background radiation at 2 MHz (by interacting with the galactic magnetic field) also produces the 150 MeV gamma ray background (by interacting with hydrogen nuclei in the interstellar medium) (Weiler, et al., 1994). Scattering and turbulence studies of the interstellar medium are also possible at HF.

A study of the galactic nonthermal background radiation would also be rewarding. Different frequencies emphasize different physical processes. At the frequencies under consideration for the LFSA, it would be possible to study the interaction of relativistic electrons and interstellar magnetic fields (Weiler, et al., 1994)

Very little is known about the properties of individual radio sources at low frequencies. Observations with the LFSA could be used to catalog thousands of discrete sources (Weiler, et al., 1994). Radio sources are generally characterized by describing the change in flux density S with frequency -- using a spectral index α -- such that $S(f) \propto f^{\alpha}$. The spectral index is also a function of frequency, i.e., $\alpha \rightarrow \alpha(f)$. Very little is known about source spectra at frequencies below 20 MHz; practically nothing has been measured below 10 MHz (Weiler, 1990).

There are some interesting, fast pulsars that have a very steep spectrum and increasing flux densities down to the lowest observed frequency of 10 MHz, whereas most pulsar spectra tend to turn over between 100 and 500 MHz (Weiler, et al., 1988). These fast pulsars, the strongest astronomical sources in the sky at 10 MHz, are non-pulsing at the lower frequencies due to the dispersion in the interstellar medium, which smears out the pulses. To avoid the possibility of containing infinite energy, these pulsar spectra must turn over at frequencies below 10 MHz. Observations would provide information on the spatial structure of the coherently radiating electrons in the pulsars' magnetospheres.

1.3 Terrestrial Interference Impact on an Orbiting Interferometer

Very few direct measurements have been made of the interference environment from Earth orbit. The question of terrestrial interference impacts on an orbiting interferometric array must be dealt with speculatively, since no such array currently exists.

1.3.1 Interferometry basics

Many different types of radio interferometers exist for purposes besides radio astronomy. Interferometer principles are well established. In principle, an interferometer is a array of antennas used to detect radiation from some source. In a correlation interferometer, the signals from each antenna are cross-correlated. An abbreviated form of the theory for a two-element correlation interferometer will be presented here. A simplified illustration is presented in Figure 1-1.

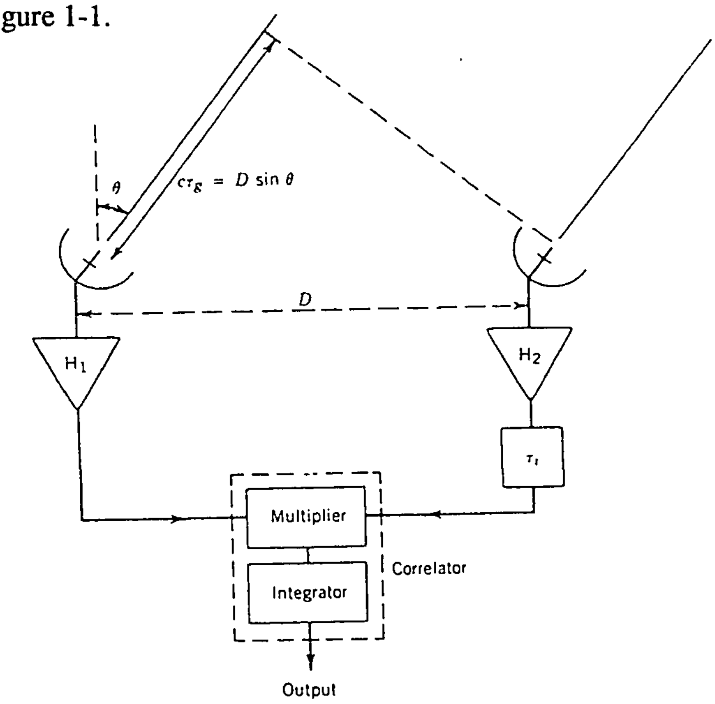

Figure 1-1 Schematic of simple two-element interferometer

A signal from a distant radio source at a frequency ν is incident on the interferometer elements. The elements are separated by a distance D, known as the baseline. The wavefront from the source arrives at angle θ with respect to the baseline normal. Since the source is distant (with respect to the radio wavelength), the wave front can be considered planar. The wave must travel an additional distance D $\sin\theta$ to reach the element on the left, which introduces an additional time delay $\tau_g = (D/c)\sin\theta$. The output of the multiplier is

$$F(\nu) = 2\sin(2\pi\nu t)\sin 2\pi\nu(t - \tau_g) \qquad (1\text{-}1)$$

Using trigonometric identities, F can be redefined in terms of low and high frequency components:

$$F(\nu) = \cos(2\pi\nu t_g) - \cos(4\pi\nu t)\cos(2\pi\nu\tau_g) - \sin(4\pi\nu t)\sin(2\pi\nu\tau_g) \qquad (1\text{-}2)$$

terms containing $\nu\tau_g$ vary much more slowly than terms with νt. The higher frequency terms are filtered out, and the resulting form for $F(\nu)$ is

$$F(\nu) = \cos(2\pi\nu\tau_g) = \cos\left(2\pi\nu\frac{D\sin\theta}{c}\right) = \cos\left(\frac{2\pi D\sin\theta}{\lambda}\right) \qquad (1\text{-}3).$$

$F(\nu)$ is known as the fringe function, since it contains a large number of lobes as the incidence angle θ varies over ± 90°.

1.3.2 Earth-orbiting interferometry

The LFSA is envisioned as an array of four to eight independent spacecraft in high Earth orbit that would form a coherent interferometer. Initial receiver frequencies would be 1.5, 4.4, 13.4, and 25.6 MHz (K. Weiler, personal communication, 1994). The two higher frequencies were chosen because they are within protected radio astronomy frequency allocations (K. Weiler, personal communication, 1995). At the lower end of the observing frequency range, it is assumed that ionospheric shielding will provide some protection from terrestrial interference (Weiler, et al., 1988) At these frequencies, the individual array element antennas (mutually orthogonal dipoles) would have very poor directivity, and no beam pointing control has been proposed. The proposed individual receiver bandwidths would be 50 kHz, which could overlap many adjacent ground-based communication channels. The galactic background radiation will be the dominant noise source for "quiet" observations. At 1 MHz, the galactic background has an equivalent noise temperature of 10^8 K, dropping to 10^4 K at 30 MHz (Spaulding and Hagn, 1978).

The problem of interference in a ground-based interferometer has been addressed (Thompson, 1982). In Report 224-4 (ITU Report 224-4, Geneva, 1978), the International Radio Consultative Committee (CCIR) has specified the levels of interference that would be harmful to radio astronomy to 10% of the rms system noise level. This level is based on single-antenna telescopes. It is known that interferometers that measure the correlation between signals received at spaced antennas tend to respond less strongly to interference. However, the interference can increase the system noise level.

Ground-based interferometers track a source as it moves across the sky. In synthesis arrays, the interferometer outputs from pairs of antennas are combined in such a way that the response is maximum for a source that moves across the sky. An interferer typically remains fixed in location with respect to the array elements, so its effects are minimized. In the case of an orbiting array, this is not necessarily the case. Depending on the array's orbital parameters, interference sources may move into and out of the array's field of view and be confused with signals from astronomical sources.

The proposed LFSA would have a very high Earth orbit (radius greater than 30,000 km) and element separations varying from 1 km (at the beginning of the mission) to over 1000 km. Obviously, there can be no physical signal connections between the elements of the

Table 1-1 Interferometer system parameters -- adapted from Weiler (1990)

Freq (MHz)	T_{sys} [a] (K)	G_{sys} (dB)	A_e[b] (m^2)	τ [c] (sec)	Baseline[d] (km)	BW_{sys} (kHz)
1.5	$3\cdot10^7$	75	2400	$7.5\cdot10^6$	≈ 130	50
4.4	$5\cdot10^6$	75	1000	$3.8\cdot10^6$	≈ 300	50
13.4	$3\cdot10^5$	75	400	$1.5\cdot10^6$	≈ 1000	50
25.6	$3\cdot10^4$	75	175	$1\cdot10^6$	≈ 3000	50

Note: T_{sys} is the system noise temperature in degrees Kelvin; G_{sys} is the overall system gain.

a. Effective system temperature determined by the galactic background radiation level.

b. Total effective array aperture.

c. Integration time = $44.6\cdot10^8$ sec/yr $\cdot .5$ (data loss factor)/directivity.

d. The baselines are limited by the scattering from the interstellar medium, i.e., the useful baselines increase with frequency as the scattering decreases.

LFSA. The received signals must be brought together for correlation after they have been transmitted down to a satellite ground station. The LFSA system parameters are listed in Table 1-1.

Using the parameters given in Table 1-1, the system sensitivity can be found from the following relation (Basart, et al., 1995):

$$S_{rms} = \frac{\sqrt{2}kT_{sys}}{\eta_{ap}A_e\sqrt{\tau BW_{sys}}} \tag{1-4}$$

S_{rms} is the minimum rms flux density detectable by the interferometer; η_{ap} is the aperture efficiency of the array element, which we shall assume to be 50%; k is Boltzmann's constant, $1.38 \cdot 10^{-23}$ J °K. All other quantities have been introduced previously. For the particular system described here, the sensitivities are given in Table 1-2.

Table 1-2 Minimum detectable flux density for an HF interferometer

Frequency (MHz)	S_{rms} (W m^{-2} Hz^{-1})
1.5	$7.97 \cdot 10^{-25}$
4.4	$4.479 \cdot 10^{-25}$
13.4	$1.069 \cdot 10^{-25}$
25.6	$2.99 \cdot 10^{-26}$

Radio astronomical flux densities are typically measured in units of Janskys, where one Jansky is 10^{-26} W m^{-2} Hz^{-1}. For a LFSA, the system sensitivity ranges from about 80 Jy at the lowest frequency to about 3 Jy at 25.6 MHz. Sub-Jansky sensitivities are possible by increasing the directivity of the antennas used in the array. An alternate antenna design with beam pointing capability and high directivity has been proposed; this design would use a microstrip array on an inflatable Kevlar balloon-like structure (Basart, et al. 1994).

The threshold of harmful interference levels can be determined from the given LFSA parameters. Using the criterion that the interference levels must be less than 10% of the system noise levels (Thompson, 1982), the spectral power density is

$$S_I(f) < .4\pi k T_{sys} \left(\frac{f}{c}\right)^2 \sqrt{2\, BW_{sys}} \sqrt{\frac{dw}{dt}} \quad \left(\frac{W}{m^2 Hz}\right) \tag{1-5}$$

the term dw/dt is the average fringe frequency rate. From the parameters in Table 1-1, we can derive the threshold at which terrestrial interference becomes harmful to an interferometer in Earth orbit. The average fringe frequency rate is difficult to determine for an Earth-orbiting interferometer because of the complex geometry (Erickson, 1988). A value of 20 Hz, taken from Basart, et al. (1995), was used as a default value. The true average fringe frequency rate may be markedly different; thus, the true threshold may much higher or lower than the values calculated here. The spectral power density of the galactic background radiation at these frequencies is on the order of 10^{-19} (W/m^{2}Hz). It is clear that the harmful interference levels are 10 to 20 dB above the galactic background level.

Table 1-3 Harmful interference level thresholds for the LFSA

Frequency (MHz)	S_I (W/m^{2}Hz)
1.5	$1.84 \cdot 10^{-17}$
4.4	$2.64 \cdot 10^{-17}$
13.4	$1.47 \cdot 10^{-17}$
25.6	$5.36 \cdot 10^{-18}$

1.4 Overview of Chapters

Because of the number of inter-related subjects covered in this research, a comprehensive literature review would be unwieldy. Previous developments as well as the relevant literature will instead be covered along with the associated topic in the appropriate chapters.

In Chapter 2, we provide an introduction to the ionosphere and its effects on signals that propagate through it. The ionosphere is a complex and continually-changing medium, so the models used to describe its behavior are a critical component of any propagation model. The Ionospheric Conductivity and Electron Density model (ICED) used in developing the transionospheric noise levels will be described. All models have their short-comings. In this case (which holds for all ionospheric empirical models), large-scale perturbations and random turbulence effects known to exist at various latitudes and local times are not included in ICED. We describe how these perturbations are modeled mathematically and included into the overall propagation model.

In Chapter 3, we discuss what is currently understood about the HF noise environment based on satellite observations over the past 25 years or so. Chapter 4 presents a preliminary analysis of data from the HF receiver on-board the WIND spacecraft, which has made the highest quality and most reliable noise measurements to date.

In Chapter 5, we discuss the mathematical modeling of both the sources (ground-based transmitters) and the transionospheric propagation. The source modeling is derived from the modeling efforts in the ground-based HF communications community. The transionospheric propagation modeling is highly dependent on the validity of the ionospheric model, described in Chapter 2, and the mathematical solution to the propagation problem in an inhomogeneous, anisotropic medium. The phase-screen diffraction layer method of handling random perturbations is introduced and its incorporation into transionospheric propagation is explained.

A side-by-side comparison with actual spacecraft data is the true test of any predictive noise model's validity. In Chapter 6, we examine direct comparisons between the transionospheric propagation model and data acquired from the HF receiver on-board the

WIND spacecraft. The model should be able to describe both the spectrum of the expected signals as well as the amplitude characteristics.

Chapter 7 presents a summary of the research performed and the conclusions that can derived from the results. In Chapter 8, suggestions are presented for future improvements in the model, and additional areas of research that may be pursued to develop existing knowledge of the terrestrial component of HF interference in space. Since this model is essentially a first generation effort, approximations and limits have been imposed in its development to maintain a reasonable scope in the project. Further research may focus on improving the interference spectrum models, improving the random variation models, or incorporating an improved ionospheric climatological model into the ray tracing.

CHAPTER 2

THE IONOSPHERIC PROPAGATION MEDIUM

2.1 Basic Ionospheric Characteristics

2.1.1 The quiet ionosphere

The ionosphere is the part of the Earth's upper atmosphere containing free electrons and ions. To a radio wave, the ionosphere looks like a thick shell of free electrons embedded in the neutral atmosphere, starting at about 50 km in altitude and extending up to about 1000 km in altitude. The electron density is approximately equal to the ion density everywhere -- this is known as charge neutrality (Tascione, 1994). The neutral atmosphere is ionized when solar extreme ultraviolet (EUV) strips away the electrons from the atoms. Ionospheric structure arises from the variation in EUV energy with frequency, concentration of neutral atoms and molecules in the atmosphere, and the ionosphere's interaction with the geomagnetic field and atmospheric winds, perturbations, and tidal forces (McNamara, 1991). The overall vertical structure of the day-side ionosphere consists of four regions: the D, E, F1, and F2 layers. Figure 2-1 illustrates the ionospheric layers. Distinct layers exist because the solar energy is absorbed differently at various heights. Also, particle recombination depends on density, which is a function of height. Historically, the D layer is treated as the lowest part of the ionosphere; it usually ranges from 50 to 90 km in altitude. This region has the highest particle collision frequency, so it can contribute a substantial amount of absorption to HF waves that propagate through it. The E layer typically occurs over 90 to 130 km in altitude. The collisions between electrons and neutral particles are not as numerous as in the D layer,

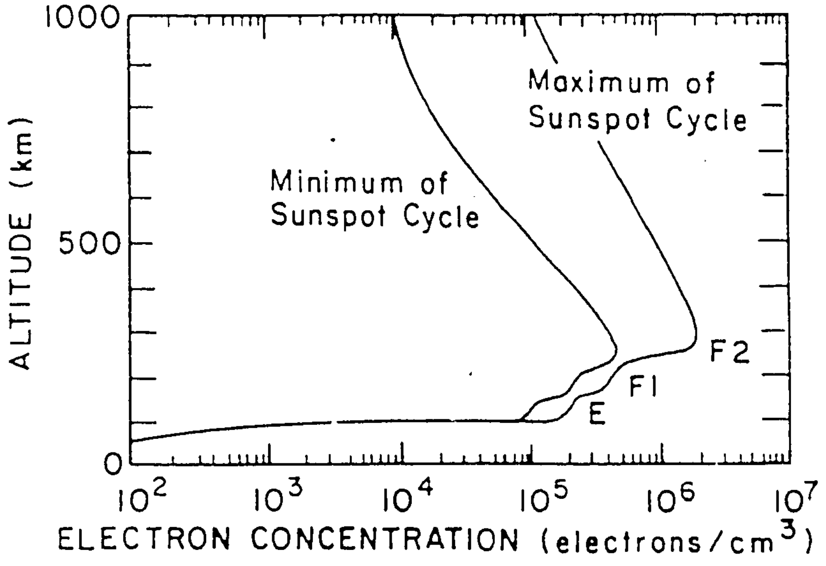

Figure 2-1 Illustration of ionospheric regions for solar minimum and maximum (from Goodman, 1992)

so this region contributes very little to the wave absorption. Within the E layer, regions of anomalous ionization can occur. These are known as the "sporadic-E" layers (Rush, 1986). Sporadic-E will be discussed in more detail in section 2.2. The highest region of the ionosphere is called the F layer, although the lower part of the F layer can behave differently than the upper part. That is why the terms F1 (for the lower part) and F2 (for the upper part) are often used (Rush 1986). Unlike the E layer, the F1 layer can not often be distinguished from the bottom of the F2 layer. Many ionospheric numerical models treat the transition from the E layer to the F layer peak as a smooth transition. This can be seen in Figures 2-2 through 2-4. The F layer is strongly influenced by the dynamic interaction of the geomagnetic field, electrodynamic drifts, and neutral-air winds. These various interactions play a large role in determining the structure of the region, as well as the perturbations commonly found there. The F2 peak has the highest electron density of all the regions in the ionosphere and often has the most effect on HF communications. The perturbations found within the F layer can strongly affect ground-based radio astronomy at frequencies below 100 MHz (Jacobson and Erickson, 1992a; Jacobson and Erickson, 1992b). At higher frequencies, F layer structure can introduce non-negligible scintillation effects (Kelley, 1989).

Because it is solar-generated, the ionosphere has strong diurnal variations. Soon after sunset, the D layer disappears and the F1 and F2 layers merge. The F and E layers remain, although less dense than their daytime forms. Ionospheric behavior can be divided into three geographic regions: the high-latitude, mid-latitude, and equatorial regions. Figures 2-2, 2-3, and 2-4 illustrate the differences in electron density for a model ionosphere. Each plot illustrates a different geographical region: high latitudes (65° N latitude was used); mid-latitudes (35° N); and equatorial (0° N). All simulations used the same longitude (255° E -- or about the longitude of New Mexico, Colorado, and Wyoming). It can be seen from these simulations that the day-time ionosphere varies the most between the summer and winter seasons. The solar zenith angle is a major factor in determining the electron density, and the sun tends to remain higher in the sky during the summer season. Not all that surprisingly, there is little difference between the nighttime ionosphere over the seasons. Two local times (midday -- 2 PM, and night -- 4:30 AM) as well as winter (December 21) and summer (June 21) seasons are represented on each graph. All of these simulations assume a "medium" sunspot number of 60. The electron density simulations were performed using IRI-90 (Rawer and Piggott, 1990), one of the more mature models freely available for general research. The FORTRAN code for this model is available via anonymous FTP (ftp nssdca.gsfc.nasa.gov, then cd to models) from the NASA Goddard Space Flight Center.

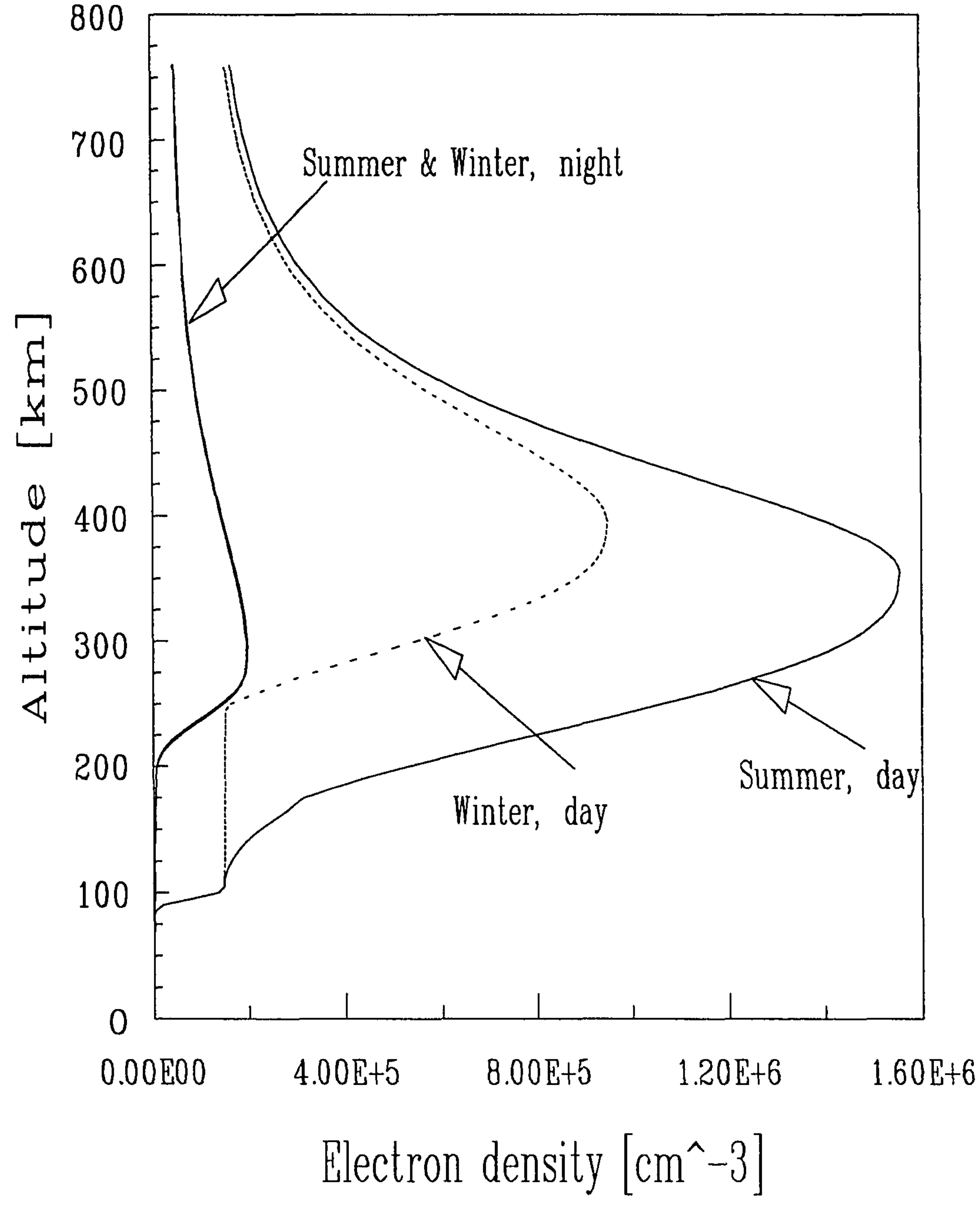

Figure 2-2 Electron density vs. height at latitude 60°N (from IRI-90)

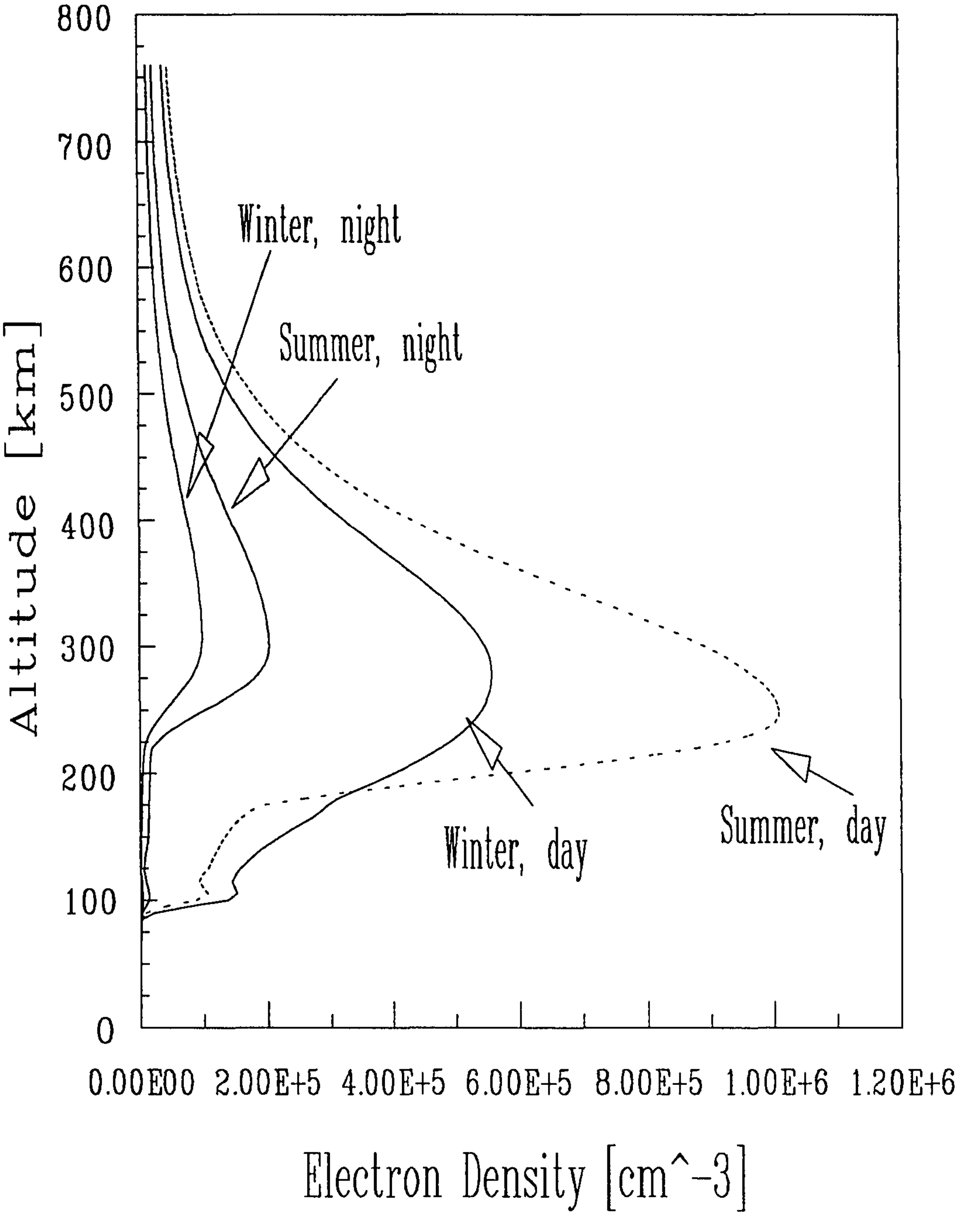

Figure 2-3 Electron density vs. height at latitude 35°N (from IRI-90)

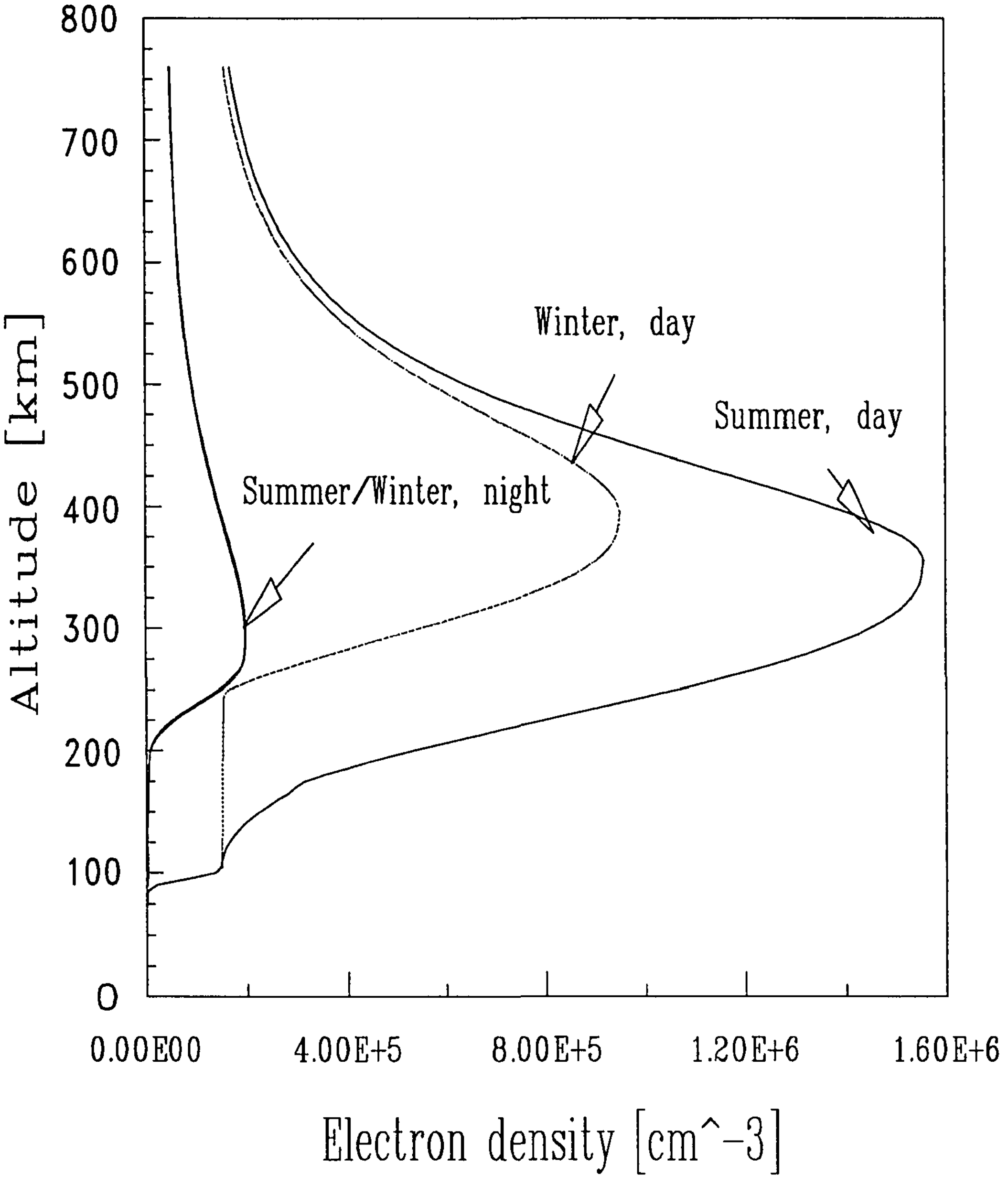

Figure 2-4 Electron density vs. height at latitude 0°N (from IRI-90)

Because the ionosphere is a plasma, perturbations due to plasma instabilities or plasma turbulences in the E and F regions may exist (Zuo, 1990). The large-scale variations in ionospheric structure fall into five distinct categories:

1. diurnal -- electron densities vary throughout the day;
2. seasonal -- three seasons exist: winter, summer, and equinoctial;
3. location -- with respect to both geographic and geomagnetic coordinates;
4. solar -- 11 year solar cycle plus solar disturbances;
5. altitude.

The structure and variations listed above are essentially for the ionosphere in its undisturbed state. Additional fluctuations in electron density are possible due to perturbations within the atmosphere, solar bursts, or geomagnetic storms. A majority of the daytime perturbations are caused by either acoustic gravity waves or plasma instabilities. Properties of acoustic gravity waves have been studied using the Very Large Array near Socorro, New Mexico (Jacobson and Erickson, 1992a; Jacobson and Erickson, 1992b). When a mass of air is compressed, the pressure change will act as a restoring force, so that acoustic waves are created in the atmosphere. At night, plasma instabilities appear to play the dominant role in generating ionospheric structure. These irregularities and their structure will be discussed in more detail later in this chapter.

2.1.2 Ionospheric climatological models

While the ionosphere's behavior can often times be described qualitatively, many applications, such as the research describe herein, require a quantitative description of the electron density in the ionosphere. In fact, for satellite tracking or radio communications, it is absolutely essential. A considerable amount of effort has been made to model the ionosphere's behavior over time, geographic location, and solar output. A large number of ionospheric climatological models exist; D. Bilitza compiled a fairly comprehensive listing in a recent issue of *Planetary and Space Science* (D. Bilitza, 1992). L. D. Brown, et al. (1991), evaluated six publicly available ionospheric models for their accuracy in predicting total electron content (TEC) for a range of latitudes, longitudes, and solar activity. Each model represented foF2 (ordinary mode F2 layer critical frequency) accurately, but failed to predict an accurate TEC when compared to measurements. It has been well known within the ionospheric physics community that most ionospheric climatological models are very poor predictors of the ionosphere's structure for a specific time and place; the existing perturbations and fluctuations can not be determined a priori. At best, the climatological model provides a description of the average state of the ionosphere under the given input conditions. This helps explain the continuing research to improve the current state of the art in ionospheric modeling.

The remainder of this section will describe the model, the Ionospheric Conductivity and Electron Density Model (ICED), used in the ray tracing analysis part of the research. A new model (PRISM) based on ICED will allow the user to incorporate daily updates of ionospheric conditions from worldwide ionosonde measurements, thereby improving the accuracy of the predictions.

ICED was originally developed by the Air Force Air Weather Service (AWS) for near real-time ionospheric specifications of the mid-latitudes and auroral zone of the northern hemisphere (Daniell, et al., 1992; Goodman, 1992). The version incorporated into the ray tracing contains distinct algorithms for the different geographical regions of the Earth (Argo, et al., 1994). The geomagnetic field used with ICED is a simplified dipole model, ignoring the irregularities of the true field. The ICED code is driven by two inputs: SSN (the sunspot index, ranging from 1 to 200) and Q (the auroral activity index, ranging from 1 to 10). This model is a parameterized, physical model based on the "first principles" of ionospheric characteristics. The ionosphere is divided into five distinct regions, corresponding to regions exhibiting distinct ionospheric variability. Physical models for each of these regions are taken from a number of sources (see Daniell, et al., 1992). Daniell, et al., parameterized the physical models for the distinct regions in terms of geophysical, environmental parameters. Databases of ions density profiles on a latitude/longitude and universal time grid were produced for high. medium, and low values of the fundamental parameters. Since these datbases are large and computationally unwieldy, semi-analytic functions were used to fit the data. Discrete, orthonormal functions were fitted to the altitude profiles of ion density. The coefficients of these functions were the eigenvectors of the covariance matrices of the density profiles (Daniell, et al., 1992). Each universal time and magnetic latitude represented by a nine term Fourier series. The horizontal variations appear to be well-represented by such an approximation (Daniell, et al., 1992). The algorithms describing the various ionospheric regions are described in detail in Argo, et al. (1994), Kelley (1989), and Tascione, et al (1988).

2.1.3 Ionospheric index of refraction

Once given the description of electron density variations within the ionosphere, how are the governing interactions with electromagnetic fields derived? When a time-harmonic electric field is applied, the free electrons in a plasma (such as the ionosphere) will oscillate. Resonance occurs at the angular plasma frequency, ω_p, where

$$\omega_p^2 = \frac{N_e q^2}{\varepsilon_0 m} \qquad (2\text{-}1)$$

N_e is the electron density of the plasma, q is the electron charge, ε_0 is the permittivity of free space, and m is the electron mass in SI units (Budden, 1985). The maximum plasma frequency of a particular ionospheric layer or region is called the critical frequency, with f_c (MHz) $\approx 9\times10^{-6}\, N_m^{1/2}$, N_m in electrons per cubic meter (McNamara, 1991). Radio waves with frequencies higher than a layer's critical frequency will penetrate that layer. At frequencies below the critical frequency, the radio wave will be reflected. The critical frequencies of the E, F1, and F2 layers are denoted foE, foF1, and foF2 respectively.

Magnetoionic theory is a complex subject, so the derivation of the basic equations for the ionosphere will be kept brief. For detailed treatments of this subject, the reader is referred to Budden (1985) or Kelso (1964). Consider first an infinite, homogeneous, and isotropic plasma with a concentration of N electrons per m^3, yet with enough ions to ensure electrical neutrality. The effects of an externally applied electric field were as mentioned previously. When the field is applied, the electrons are displaced a finite distance d, thus polarizing the medium. The polarization P = Nqd; if the externally applied electric field is time harmonic with an angular frequency ω, then

$$P = -N_e q^2/(m\omega^2)\cdot E. \tag{2-2}$$

The flux density $D = P + \varepsilon_0 E$, which can be rewritten as

$$D = (1 - N_e q^2/(m\omega^2))\varepsilon_0 E. \tag{2-3}$$

The relative permittivity of the collisionless plasma is defined as

$$\varepsilon_r = 1 - \frac{N_e q^2}{\varepsilon_0 m\omega^2} = 1 - \frac{\omega_p^2}{\omega^2} = 1 - X \tag{2-4}$$

the index of refraction is defined as $n = \sqrt{\varepsilon_r}$. Note that the index of refraction for a plasma is always less than 1. This differs from tropospheric index of refraction, which it is always greater than or approximately equal to 1. The plasma is dispersive because of the ω^2 term in the denominator of the permittivity expression. However, an arbitrarily polarized wave entering an isotropic plasma will not have its polarization changed as it propagates through the medium. In an anisotropic plasma (produced by applying an external magnetic field), the polarization of the incident wave does matter.

Radio waves in the ionosphere are attenuated because the particle motions are damped through collisions. The simplest explanation is that the damping of the electron motion occurs because of a retarding force -mνV (Budden, 1985), where **V** is the part of the electron's velocity associated with the motion imposed by the applied electromagnetic field, m is its mass, and ν is the effective collision frequency between electrons. Attenuation due to electron collisions with other particles can be significant in the D region, but drops off approximately exponentially with increasing altitude. If the particle collision frequency ν is nonzero, then the relative permittivity is no longer strictly real:

$$\varepsilon_r = 1 - \frac{Ne^2 \big/ \left(\varepsilon_0 m \omega^2\right)}{1 - j\,\nu/\omega} = 1 - \frac{X}{1 - jZ} = 1 - \frac{X}{U} \qquad (2\text{-}5).$$

The complex denominator incorporates the attenuating effect of the particle collision frequency.

The plasma becomes anisotropic when an external, static magnetic field ($\mathbf{B}_0$) is applied. The refractive index is now a function of the direction of wave propagation. The electron's equation of motion must be modified to include the effects of the static field $\mathbf{B}_0$.

Electrons in a magnetized plasma will move in a circular orbit around the B-field lines, with an angular frequency of

$$\omega_h = q\,|\mathbf{B}_o|/m, \tag{2-6}$$

where ω_h is known as the angular gyrofrequency or cyclotron frequency. The normalized gyrofrequency $Y = \omega_h/\omega$. The vector quantity $\bar{Y}$ has magnitude Y and the same angle as $\mathbf{B}_o$. The electric displacement **D** is related to **E** through the constitutive relation

$$\mathbf{D} = \varepsilon_o\mathbf{E} + \mathbf{P} = \varepsilon_o\varepsilon\mathbf{E} \tag{2-7}$$

where the relative permittivity tensor is

$$\varepsilon = \begin{pmatrix} \varepsilon_{xx} & \varepsilon_{xy} & \varepsilon_{xz} \\ \varepsilon_{yx} & \varepsilon_{yy} & \varepsilon_{yz} \\ \varepsilon_{zx} & \varepsilon_{zy} & \varepsilon_{zz} \end{pmatrix} \tag{2-8}$$

To proceed further, some assumptions must be made. Assume the incident electromagnetic wave is a TEM plane wave ($D_z \equiv 0$, $H_z \equiv 0$); the z dependence of all field components is strictly through the factor exp{-jknz}, where n is the refractive index and k is the wave number. For operations on any field component, $\partial/\partial x \equiv 0$, $\partial/\partial y \equiv 0$, and $\partial/\partial z \equiv -jkn$. Applying Maxwell's equations and substituting the field relations between the E and H components into equation (2-7), we end up with three equations:

$$\begin{aligned} \left(\varepsilon_{xx} - n^2\right)E_x + \varepsilon_{xy}E_y + \varepsilon_{xz}E_z &= 0 \\ \varepsilon_{yx}E_x + \left(\varepsilon_{yy} - n^2\right)E_y + \varepsilon_{yz}E_z &= 0 \\ \varepsilon_{zx}E_x + \varepsilon_{zy}E_y + \left(\varepsilon_{zz} - n^2\right)E_z &= 0 \end{aligned} \qquad (2\text{-}9).$$

For a solution to exist, the determinant of the E field coefficients must be zero. Up to this point, no physical meaning has been attached to the components of the relative permittivity. We could redefine the permittivity tensor as

$$\varepsilon=\begin{pmatrix} \frac{1}{2}(\varepsilon_1+\varepsilon_2)\cos^2\Theta+\varepsilon_3\sin^2\Theta & {}^{j}\!/_{2}(\varepsilon_1-\varepsilon_2)\cos\Theta & ({}^{1}\!/_{2}(\varepsilon_1+\varepsilon_2)-\varepsilon_3)\cos\Theta\sin\Theta \\ {}^{-j}\!/_{2}(\varepsilon_1-\varepsilon_2)\cos\Theta & {}^{1}\!/_{2}(\varepsilon_1+\varepsilon_2) & {}^{-j}\!/_{2}(\varepsilon_1-\varepsilon_2)\sin\Theta \\ ({}^{1}\!/_{2}(\varepsilon_1+\varepsilon_2)-\varepsilon_3)\cos\Theta\sin\Theta & {}^{j}\!/_{2}(\varepsilon_1-\varepsilon_2)\sin\Theta & \frac{1}{2}(\varepsilon_1+\varepsilon_2)\sin^2\Theta+\varepsilon_3\cos^2\Theta \end{pmatrix} \qquad (2\text{-}10)$$

where

$$\begin{aligned} \varepsilon_1 &= 1-{}^{X}\!/_{U+Y} \\ \varepsilon_2 &= 1-{}^{X}\!/_{U-Y} \\ \varepsilon_3 &= 1-{}^{X}\!/_{U} \end{aligned} \qquad (2\text{-}11),$$

and Θ is known as the Briggs-Parkin angle, or the angle between the wave's propagation vector and the external magnetic field, $\mathbf{B}_0$. Substituting this definition of the relative permittivity into the determinant expression and multiplying it out results in a quadratic equation for n^2 in the form of $An^4 - 2Bn^2 + C = 0$. The coefficients A, B, and C are functions of X, Y, and U. Solving this quadratic produces an equation known as the Appleton-Hartree equation:

$$n^2 = 1-\frac{X(1-X)}{1-X-\frac{1}{2}Y^2\sin^2\Theta\pm\left\{\frac{1}{4}Y^4\sin^4\Theta+Y^2\cos^2\Theta(1-X)\right\}^{1/2}} \qquad (2\text{-}12).$$

The Appleton Hartree formulation for the ionosphere's refractive index is one of the fundamental equations used in raytracing (see Chapter 5). This equation is strictly valid for homogeneous media, but is still mostly correct for slowly varying media. For magnetized plasmas, $Y \neq 0$, and two distinct values of the refractive index exist. This leads to two characteristic modes of propagation in the ionosphere, called ordinary (O) and extraordinary (E); these modes propagate independently of each other in the ionosphere. The ordinary and extraordinary modes also correspond to circularly polarized waves with opposite senses of rotation propagating in the anisotropic medium. The polarization of the resultant wave becomes a function of position along the propagation path.

2.2 The Perturbed Ionosphere

HF waves are strongly affected by the plasma density irregularities within the ionosphere. Large scale gradients introduce refractive effects on the HF electromagnetic wave; ray theory can effectively model these effects (Basler, et al., 1988). Smaller scale perturbations, such as field-aligned irregularities, must be modeled using scattering models. Both theory and measurement for HF propagation have not been developed as thoroughly as in VHF and UHF propagation (Basler, et al., 1988).

The primary regions for ionospheric perturbations are the E and F2 layers. Geographically, the high latitudes and equatorial regions tend to be more active than the mid-latitudes. The motivation for most of the research into naturally-occurring F layer irregularities is that these irregularities act as out-door test beds for models of nuclear plasma structure evolution (L. J. Nickisch, personal communication, 1995). Sporadic E, mentioned earlier in this chapter, affects all latitudes (Tascione, 1994). It is a layer of transient dense ionization 1 to 2 km thick and tens to hundreds of km long. At midlatitudes (where it least occurs), sporadic E has been associated with intense thunderstorms or squall lines (Tascione, 1994), although the exact connection is still unknown. One common name applied to F layer irregularities is "spread-F", taken from the appearance of the ionogram trace. When spread F is present, the ionogram trace appears thicker than a normal F layer, so it is said that the F layer has "spread" in depth (Tascione, 1994). The total electron content within a spread F irregularity can vary by 2 to 3 orders of magnitude within kilometers; this introduces strong scintillation effects in transionospheric signals.

Ionospheric irregularities have been regularly studied using radar systems operating at 40 MHz and above. Since these frequencies are appreciably higher than the peak plasma frequencies of the ionospheric layers, most of the energy in the transmitted radar pulse is radiated out into space (Fejer and Kelley, 1980). Some of the transmitted energy is reradiated by the free electrons; this is the basis of the incoherent scatter radars. The total scattered power is a function of the electron density, Debye length, and ratio of electron and ion temperatures. The incoherent scatter return is typically many orders of magnitude lower than the transmitted pulse. Radars can detect only one particular spatial Fourier component of the electron density perturbation (Fejer and Kelley, 1980). This spatial component has a wavelength of

$$\lambda_0 \Big/ (2\sin(\theta/2)) \tag{2-13}$$

where λ_0 is the radar wavelength and θ is the angle between transmitted and received electromagnetic wave vectors. For backscatter observations θ is 180°, so the detected spatial wavelength of the perturbation is simply $\lambda_0/2$. It has been shown that equatorial and high latitude irregularities are strongly aligned along the geomagnetic field lines. For maximum visibility, the radar's wave vector must be perpendicular (or nearly so) to the geomagnetic field lines (Fejer and Kelley, 1980).

Irregularity properties can also be deduced by examining the effects of these perturbations on the amplitudes and phases of transionospheric signals at various frequencies.

The bulk of the research performed in modeling scintillation has been at the UHF and higher frequencies.

Scintillations caused by electron density irregularities of various scale sizes are a phenomena existing at all latitudes, although equatorial latitudes tend to experience the strongest scintillations. As the name implies, it is essentially the "twinkling" -- or random variation -- of the radio signal over time. As a random process, it is best described by a temporal or spatial power spectrum. Phase screen theory (discussed in Chapter 5) is connected with this process. The log spectra of scintillation are often linear with the log of the frequency. This slope, p, is a key parameter in describing the scintillation (Afraimovich, et al., 1994).

F region irregularities play a large role in transionospheric propagation. These electron density variations impose random phase fluctuations across the wavefront of the signal (Basu and Basu, 1993). The emerging wavefront with phase fluctuations develops into intensity scintillations.

2.2.1 High latitude perturbations

The high latitudes are one of the most highly perturbed regions of the ionosphere. Depletion irregularities in the bottomside F layer can trap, guide, and reflect HF waves (James, 1995). The irregularities are field-aligned regions of cylindrical electron density depletions. Since the dimensions are many wavelengths long at HF, ray theory can be applied to study the propagation through such regions (James, 1995).

Scintillations are commonly observed in the nightside auroral oval. These are produced by irregularities that are locally generated by auroral particle precipitation (Basu and Basu, 1993). Also, within the polar cap area, the interplanetary magnetic field (IMF) dictates the type of plasma structures detected there: the orientation of the field plays a role in the development of large scale, complex structures (Basu and Basu, 1993). Observations over the past ten to fifteen years have shown that the wintertime polar cap F layer contains a variety of large scale structures (Decker, et al., 1994). When the IMF points southward, patches of enhanced ionization drifting across the polar cap have been detected (Decker, et al., 1994). These patches have a wide variety of shapes and scale sizes that ranges from a few hundreds to a thousand kilometers. The typical patch has an electron density enhancement of ten times above the background ionization.

2.2.2 Mid-latitude perturbations

Atmospheric disturbances can often excite acoustic-gravity or acoustic waves which radiate energy from the source. Some of this energy may reach the ionosphere. At these altitudes, the acoustic gravity waves produce wave-like fluctuations in the plasma density that can travel for appreciable distances; these disturbances are then called Traveling Ionospheric Disturbances, or TIDs (Soicher, 1988). At VHF and above, the effects of large scale perturbations are largely described using the quantity known as Total Electron Content (TEC), defined as

$$\mathrm{TEC} = \int_{\mathrm{path}} Ne(z)\, dz \qquad (2\text{-}14),$$

where the integration is performed along the propagation path. TIDs can be viewed as large scale wavelike perturbations to the TEC. These perturbations have a characteristic wavelength, phase velocity, and amplitude. Observations by Soicher at Haifa, Israel indicate that TIDs are frequent; their occurrence are the rule rather than the exception at the mid-latitudes. The equinoxes appeared to have the minimum number of TIDs. At solar maximum, TIDs tend to have higher amplitudes than all TIDs at solar minimum.

An observing campaign at the Very Large Array (VLA) near Socorro, NM, by W. C. Erickson and A. R. Jacobson was able to determine the transient signatures of TIDs. Previous observations by others used interfereometers whose maximum baselines (≤ 3 km) were much shorter than the typical horizontal wavelength of the observed TID (Jacobson and Erickson, 1992b). Under those circumstances, it was not possible to measure the horizontal phase velocity or amplitude of the TID. The TID can be modeled as a periodic perturbation to the electron density. At 330 MHz -- the frequency Jacobson and Erickson used at the VLA -- the primary effect of the electron density fluctuations is on the phase of the radio wave propagating through it. In this sense, the TID acts as a thin, periodic phase screen (Jacobson and Erickson, 1992b). Images formed from waves that have propagated through this phase screen will be translated and blurred. In fact, the motivation for this work was to determine the feasibility of a dynamic compensation method (Jacobson and Erickson, 1992b).

The phase variations measured during the passage of a TID had periods ranging from less than 200 seconds to greater than 4000 seconds. The longer time period TIDs contained large-amplitude electron density disturbances, with horizontal velocities on the order of 0.5 km/sec, which can be explained by atmospheric acoustic gravity waves (Jacobson and Erickson, 1992a). Shorter period disturbances appear to less easily attributed to AGWs. These waves are too fast to be plasma irregularities but too slow to be strictly attributed to acoustic. Their phyiscal origin has not yet been determined (Jacobson and Erickson, 1992a).

Midlatitude scintillations caused by small-scale electron density perturbations also exist. This particular region has not been the focus of an extensive amount of scintillation research activity. Recent measurements by E. L. Afraimovich, et al. (1994), indicate that midlatitude scintillation is primarily a night time phenomena. For scintillations in 150 MHz signals, the cross sectional dimensions of the irregularities are on the order of hundreds of meters (MacDougall, 1992).

E layer irregularities have been extensively studied at both equatorial and polar regions. However, mid-latitude observations have been limited. From existing studies, Yamamoto, et al. (1994), have found that these irregularities are closely associated with sporadic E. The investigations using the MU (Middle/Upper atmosphere) radar have found nighttime sporadic E layers with altitude modulations. Previous measurements were limited in resolution, so that fine structure in the radar echoes could not be detected. The sporadic E altitude modulations have been attributed to acoustic gravity waves interacting with the sporadic E (Tsunoda, et al., 1994).

2.2.3 Equatorial perturbations

Plasma "bubbles" or plumes are the most common form of irregularity in the equatorial nighttime ionosphere, ocurring within ± 15° of the geomagnetic equator (Basu and Basu, 1993); they are typically several hunddreds of kilometers in height and tens of kilometers in width (R. T. Tsunoda, personal communication, 1995). They were first discovered in 1973 from *in situ* satellite measurements. Since then, their existence has been verified by numerous incoherent scatter radar and rocket measurements. For many years after their discovery, the generating process and spatial structure of these "bubbles" was not clearly understood. Even the name given to this form of irregularity presupposes a particular type of structure.

For equatorial irregularities, the fundamental controlling process is the Rayliegh-Taylor instability (Tsunoda, 1980 and references therein). In Rayleigh-Taylor theory, depleted regions of plasma with scale sizes on the order of tens of kilometers transverse to the geomagnetic field are formed at the bottomside F layer. Since the bubbles are less dense, they bouyantly rise upward into the topside F layer. By definition, a plasma bubble is a localized electron density depletion having spatial dimensions on the order of tens to hundreds of kilometers (Tsunoda, et al., 1982). The plasma density within the bubble can be as much as three orders of magnitude less than the peak plasma density of the F layer. The shape of the bubble has been predicted by numerical models of the nonlinear Rayliegh-Taylor instability (R. T. Tsunoda, personal communication, 1995). Numerical simulations of the collisional Rayliegh-Taylor instability show a vertically elongated depletion region that extends from the bottomside F layer all the way up through the topside F layer. The dimensions of the bubble correspond to the outer scale L_0 of the spatial irregularity spectrum of the bottomside F layer. The theory has been strongly supported by measurements of the nighttime equatorial ionosphere. Through ALTAIR incoherent scatter radar measurements, Tsunoda (1980) has presented direct evidence that bubbles are geomagnetic-field aligned and that they can extend over 10° of magnetic latitude. In these measurements, the radar beam was transverse to the local geomagnetic field of the radar site.

Low Earth-orbiting satellite (*in situ*) and radar backscatter measurements have shown that these bubbles are not truly self-contained depletion regions (such as we would imagine them to be), but rather appear to be vertically elongated depletion regions that resemble tilted wedges (Tsunoda, et al. 1982). Measurements of the depletion in the "neck" region show that it is an integral part of the bubble structure, not just a result of the plasma turbulence in the wake of the rapidly rising bubble. Figure 2-5 is a plot of radar scatter from an equatorial bubble, as measured by the ALTAIR radar. Tsunoda has shown that this two-dimensional structure is consistent with numerical simulations of the nonlinear, collisional Rayliegh-Taylor instability (R. T. Tsunoda, personal communication, 1995) which is believed to dominate the bubble development. These bubbles, being lighter than the surrounding plasma, also move faster than the **E**×**B** motion of the bulk background plasma; the speed depends on the percentage depletion, with can range from two to three orders of magnitude.

These scinitllation-causing irregularities typically are distributed over a 200 km thick layer around a mean altitude of 350 km. Occasionally, irregularities which are not "fully" developed become confined within a thin layer in the bottomside F layer, producing a sinusoidal spatial structure. The corresponding scintillation spectra have Fresnel oscillations (Basu and Basu, 1993).

The implications for transionospheric propagation are that from the perspective of an Earth-orbiter, these bubbles can appear as "holes" of much lower plasma density than the surrounding ionosphere. At certain ray launch angles, the rays will penetrate the bubble and break through the ionosphere. Figures 2-6, 7, 8, and 9 illustrate a simulation of an equatorial bubble. Figure 2-6 is the unperturbed ionosphere at a local time of 1:00 AM (for the receiver on the spacecraft) to 2:14 AM (for the transmitter on the ground). A moderate sunspot number of 75 was chosen for the simulation. The peak plasma frequency for this simulation is 7 MHz. The ionosphere appears fairly smooth. In Figure 2-7, a fan of rays at 10 MHz is launched to illustrate the unperturbed propagation. (The actual ray tracing will be developed in detail in Chapter 5.) In Figure 2-8, the ionosphere is now perturbed by an elongated depletion region. The bubble is artificially created by "stacking" smaller depletions to achieve the elongated shape of a naturally occurring equatorial bubble. The electron density depletion regions are created by inserting Barium releases at specific altitudes and times into the model ionosphere. The legend at the top of the figure is the time after the releases occurred. It is critical to let sufficient time elapse after the Barium release to let the depletion region grow. Figure 2-9 shows the resulting effect of the equatorial irregularity on transionospheric rays at 10 MHz. The ray tracing near the bubble is highly sensitive to the ray angle as it reaches the irregularity. It is clear that equatorial depletions can produce a defocusing effect and scatter the energy from a relatively narrow beam over a large area, so that the received power would be much lower than in an unperturbed case.

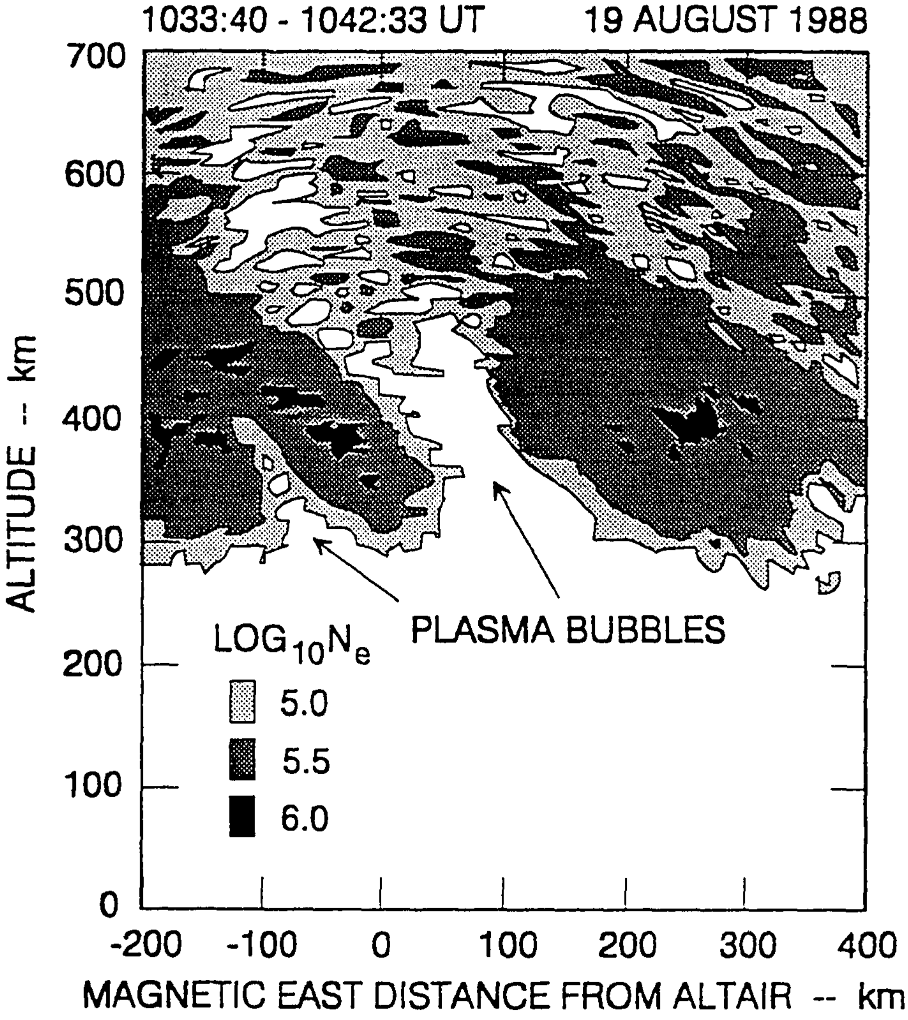

Figure 2-5 Radar backscatter from an equatorial bubble (courtesy R. T. Tsunoda, SRI)

The simulated bubble illustrated in the following figures was created by introducing a man-made chemical release into the ionosphere. This is commonly done in attempts to recreate certain propagation conditions which may be present in nuclear events (P. E. Argo, personal communication, 1994). The electron density depletions are also created by releasing a quantity of CF_3Br over a range of altitudes, starting at 300 km. Argo, et al. (1992) describe the effects of such a chemical release on long distance propagation paths during the NICARE I experiment. The simulations using three-dimensional raytracing were consistent with the data collected during the experiment.

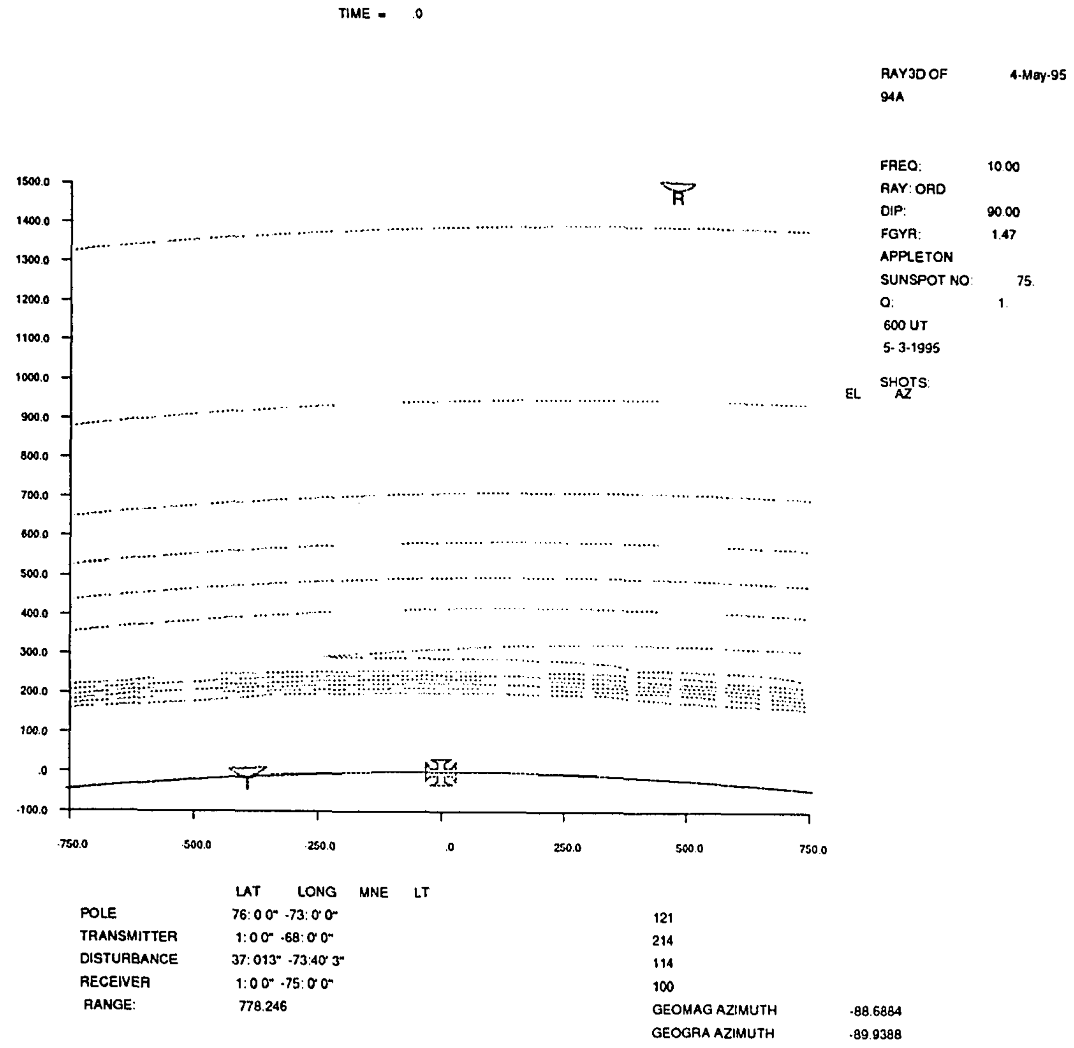

```
RAY3D OF          4-May-95
94A

FREQ:             10.00
RAY: ORD
DIP:              90.00
FGYR:              1.47
APPLETON
SUNSPOT NO:          75.
Q:                  1.
 600 UT
 5- 3-1995

   SHOTS:
EL   AZ

               LAT      LONG    MNE   LT
POLE          76: 0 0"  -73: 0' 0"                    121
TRANSMITTER    1: 0 0"  -68: 0' 0"                    214
DISTURBANCE   37: 013"  -73:40' 3"                    114
RECEIVER       1: 0 0"  -75: 0' 0"                    100
 RANGE:        778.246                                GEOMAG AZIMUTH      -88.6884
                                                      GEOGRA AZIMUTH      -89.9388
```

Figure 2-6 Unperturbed ionosphere: transmitter and receiver setup (using LANL TRACKER)

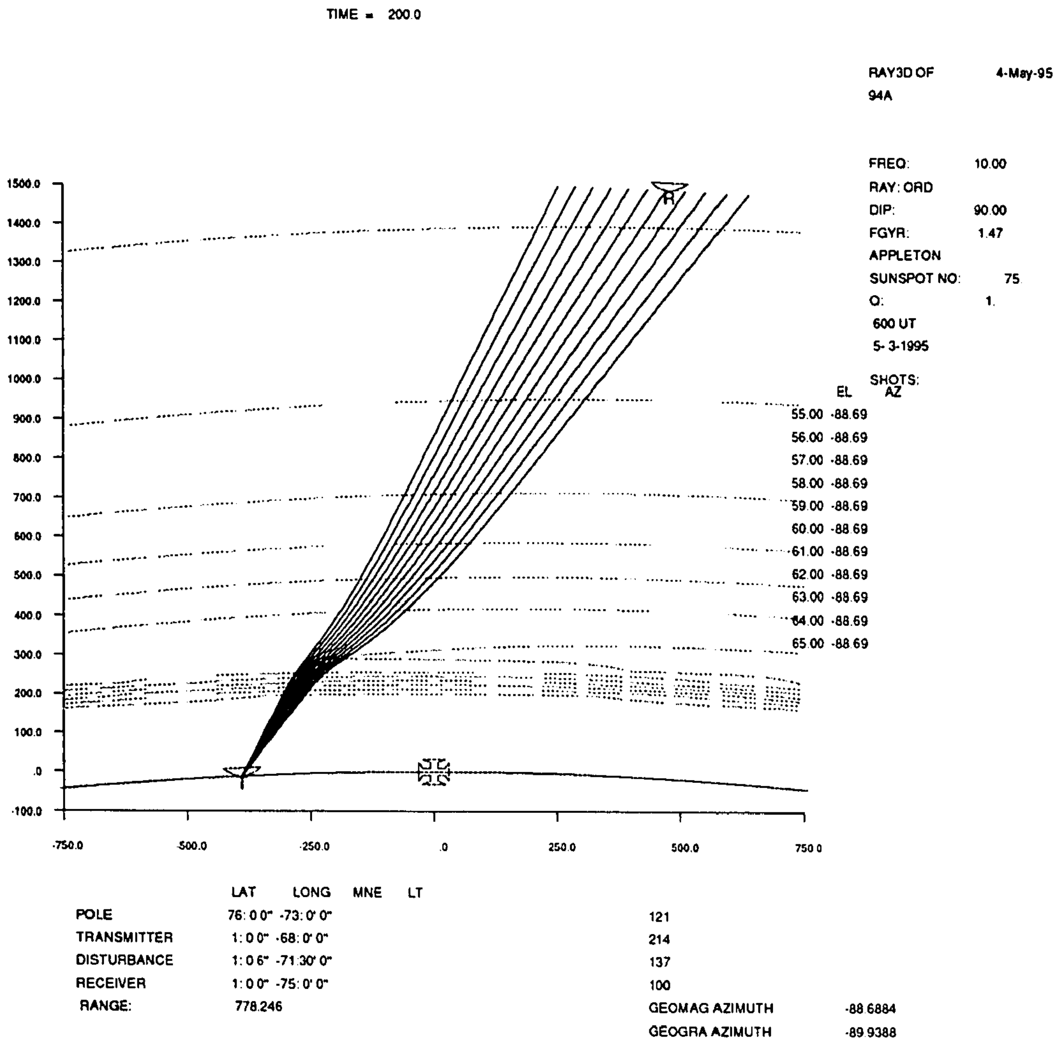

Figure 2-7 Unperturbed ionosphere: ray tracing from transmitter to receiver (using LANL TRACKER)

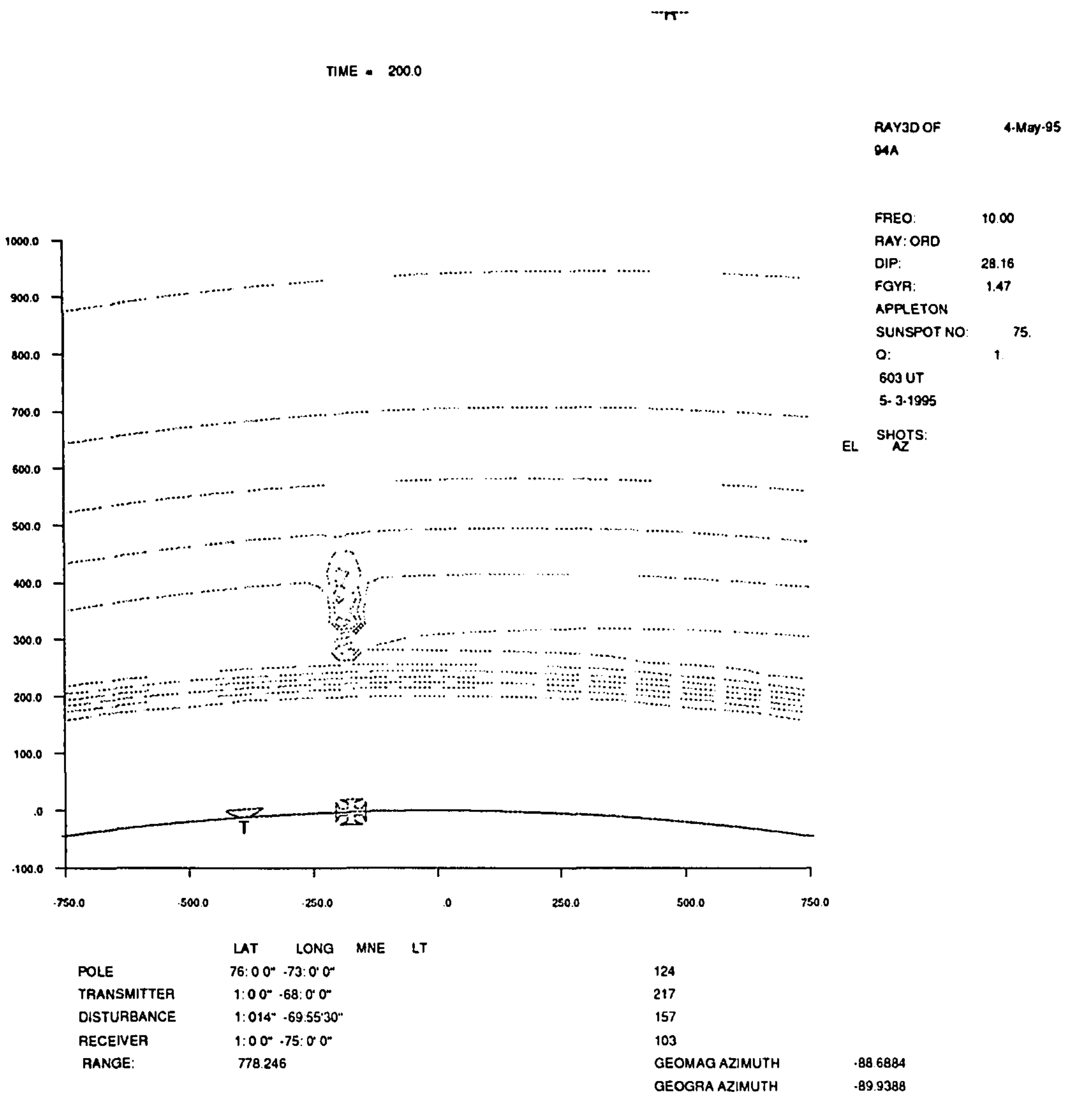

```
RAY3D OF          4-May-95
94A

FREO:             10.00
RAY: ORD
DIP:              28.16
FGYR:              1.47
APPLETON
SUNSPOT NO:          75.
Q:                  1.
 603 UT
 5- 3-1995

 SHOTS:
EL  AZ
```

```
                 LAT       LONG    MNE    LT
POLE             76: 0 0"  -73: 0' 0"                      124
TRANSMITTER       1: 0 0"  -68: 0' 0"                      217
DISTURBANCE       1: 014"  -69:55'30"                      157
RECEIVER          1: 0 0"  -75: 0' 0"                      103
 RANGE:           778.246                                  GEOMAG AZIMUTH     -88.6884
                                                           GEOGRA AZIMUTH     -89.9388
```

Figure 2-8 Perturbed ionosphere: equatorial bubble configuration (using LANL TRACKER)

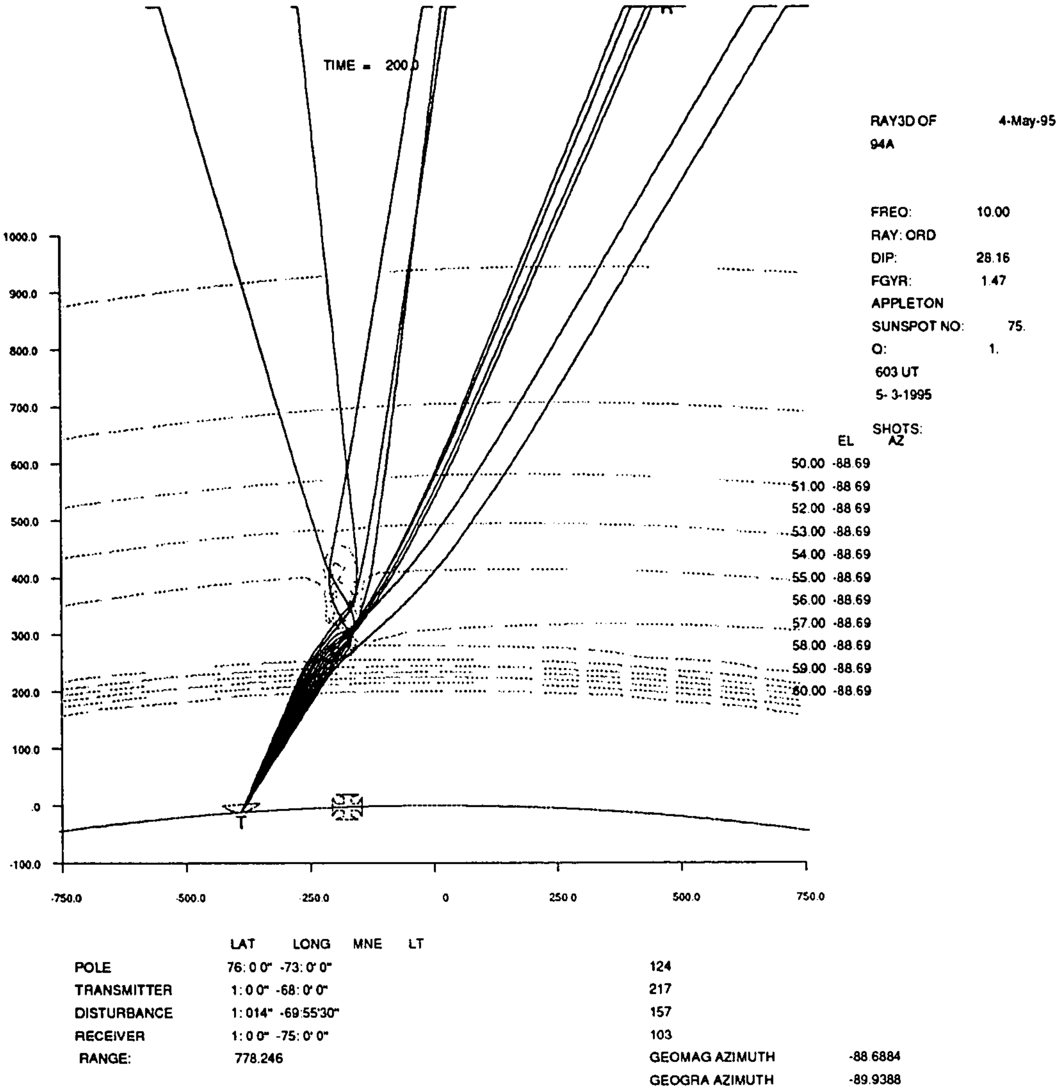

Figure 2-9 Perturbed ionosphere: beam defocusing caused by equatorial bubble (using LANL TRACKER)

CHAPTER 3

HF NOISE IN SPACE

3.1 Introduction

The terrestrial radio noise environment has been actively studied over the past several decades. For specific examples, the proceedings of the Fourth and Fifth international conferences on HF radio systems and techniques (IEE, Edinburg, Scotland) or the proceedings of the Ionospheric Effects Symposia (generally held every three years in Crystal City, Virginia) are excellent resources on the state-of-the-art in HF systems. On the ground, the signals detected in the HF band are a mixture of the desired signal, atmospheric (naturally-occurring) noise, random man-made noise, and other transmitters. All of this is a consequence of the fact that skywave propagation can be very low loss under certain conditions. Ground-based radar measurements of the HF background noise have shown a clear solar cycle variation (Ward and Golley, 1991), with larger diurnal variations at solar maximum.

The Institute for Telecommunication Sciences (ITS) has been refining a spectrum utilization model to determine the optimum capacity of HF communications channels (Rush, et al., 1988). One of the most important considerations is the degree to which services can coexist without causing undue degradation to other operations. The frequencies allocated for HF broadcasting are 6, 7, 9, 11, 13, 15, 17, 21, and 26 MHz. Powerful broadcast transmissions are interspersed throughout the HF spectrum, although the majority of broadcasters are clustered about the 6, 7, and 9 MHz region.

Measurements of the noise environment from satellite altitudes are, unfortunately, not so common. Any measurements made have largely been secondary to the spacecraft's intended goals. Two payloads have been proposed to specifically address the need for detailed data on the spectral and temporal characteristics of the HF noise environment. The Orbiting High Frequency Interference Monitor -- known as OHFRIM -- is being developed by the Remote Sensing Division at the Naval Research Lab (Weiler, et al., 1994). A similar payload was proposed by a joint group from the Physics and Astronomy Department at the University of Iowa and the Departments of Electrical & Computer Engineering and Aerospace Engineering at Iowa State University (Calvert, et al., 1994).

If successful HF radio astronomy is to be accomplished from earth orbit, the man-made component of the interference and noise must be studied and understood.

3.2 The Radio Astronomy Explorers

The man-made component of the HF noise environment at satellite heights had not been explored prior to the launch of the Radio Astronomy Explorer (RAE) I satellite in 1968. In fact, little thought had been given to the interference problem at that time. The RAEs were principally designed for radio astronomy applications: to determine the cosmic noise spatial and spectral structure, to measure low frequency solar radio bursts, to study Jovian low frequency noise, and attempt to detect discrete cosmic noise sources (Kaiser, 1991). RAE-1 was placed in a circular orbit at about 6000 km, well above the F2 layer peak. One of its most unexpected discoveries - strong terrestrial HF radio emissions - led to the placement of RAE-2 in a lunar orbit. Figure 3-1, taken from RAE-2, clearly indicates that the noise is terrestrial in origin.

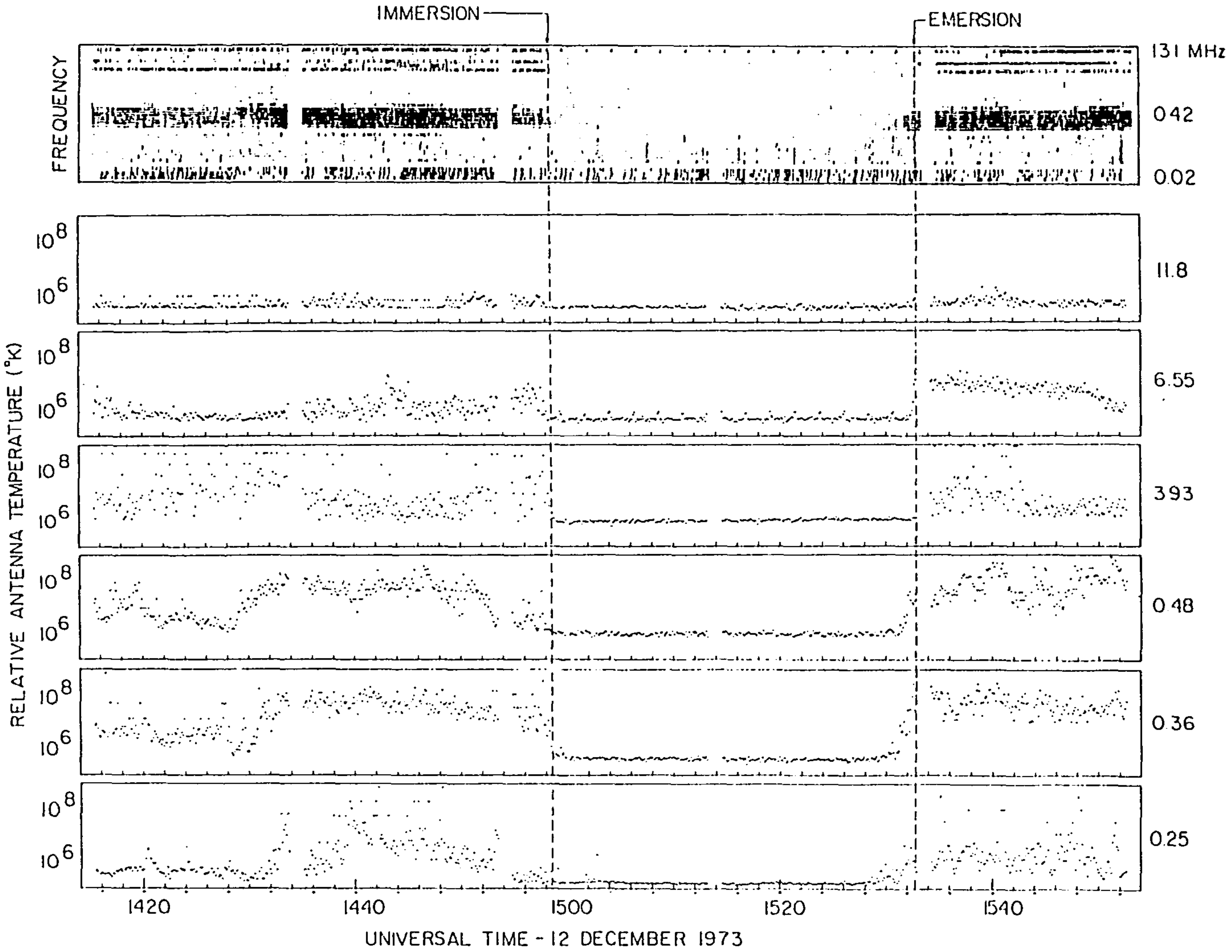

Figure 3-1 Change in noise levels with immersion and emersion for lunar-orbiting RAE-2 (from Alexander, et al., 1975)

RAE-1 was in a circular Earth orbit with an inclination of 121º, allowing it to cover from 59º S to 59º N in geographic latitude (Herman, et al., 1973). Its retrograde orbit allowed it to pass close to a given point on Earth every five days (Herman, et al., 1975). Two different types of receivers where placed on board the spacecraft. The burst receiver (BR) swept continuously through 0.202 - 5.4 MHz. Also on board were two Ryle Vonberg (RV) receivers which sequentially tuned to nine frequencies in the 0.2 - 9.18 MHz range (Weber, et al., 1971). Each channel was sampled for two consecutive four second periods. The tuning sequence was repeated every 72 seconds (Herman, et al, 1975). These fixed frequency receivers had a 200 kHz bandwidth, which can encompass a number of broadcast channels. Only data collected by the four highest frequency channels (3.9, 4.7, 6.55, and 9.18 MHz) are germane to the discussion of HF noise. During the 1968 measurements, the dayside plasma frequency was greater than 9 MHz, so the antenna temperatures for dayside measurements did not include any terrestrial noise contributions. The principal investigators appear to have used these levels (10^5 K) as a baseline.

Each receiver was fed by a 229 meter long vee antenna, gravity stabilized so that the upper vee had a continuous view of the celestial sphere and the lower vee had a continuous view of the Earth. Each vee antenna had a front-to-back ratio of 15 dB, with a power gain that increased slightly with frequency (Herman, et al., 1975). Only data from the lower vee setup will be discussed here. Both antennas detected terrestrial noise, with the amplitudes at the lower vee greater by an amount equal to the upper vee's front-to back ratio.

The interference detected at any point in space has a direct component (local in origin) and an indirect component (noise arriving through skywave propagation) (Herman, et al., 1973). Three distinct noise sources were identified:

1. atmospheric -- lightning and other atmospheric electrical discharges;
2. urban areas -- noise from electrical equipment, power lines, ignition systems, etc.;

3. discrete terrestrial radio sources.

From the combination of spacecraft orbit and antenna beamwidth, Herman, Caruso, and Stone were able create a contour map of antenna temperature (in dB above 288º K) with respect to subsatellite point. However, since the basic data from the RV receivers consisted of 32 second averages, the relative contributions of each of these three primary sources could not be isolated (Herman, et al., 1973). Additional information on the spatial and temporal distributions of the noise had to be included to extract the components. RAE-1 also observed a characteristic increase in detected noise when over the nightside of the Earth, when the ionosphere's plasma frequency was about 4 MHz.

The noise from atmospheric phenomena and urban areas was found to be broadband, and extended past 9 MHz. The atmospheric noise was most pronounced over the equatorial land masses (inferring that lightning from equatorial thunderstorms were the greatest contributor of atmospheric noise at these locations). Data gathered from other sources imply that lightning storm complexes appear to be more prevalent over the equatorial land masses (Herman, et al., 1973). An attempt was made to analyze the noise contribution from thunderstorm activity by combining the RAE-1 ephemeris with storm data from the World Data Center in Asheville, North Carolina (Herman, et al., 1975). Herman, Stone, and Caruso found that the median antenna temperature increased by about an order of magnitude (with respect to control passes) when RAE-1 passed over areas in the continental United States having thunderstorms in progress. From this analysis, they deduced that the minimum nighttime noise level (over the United States) is fixed by the manmade noise. If an active thunderstorm is in progress, the noise level increases by about 6 to 12 dB.

In Figure 3-2, note the 50 dB increase in antenna temperature starting at 0300 hours Greenwich Mean Time (GMT). At this point, the spacecraft was crossing north central Africa, going toward the Atlantic Ocean.

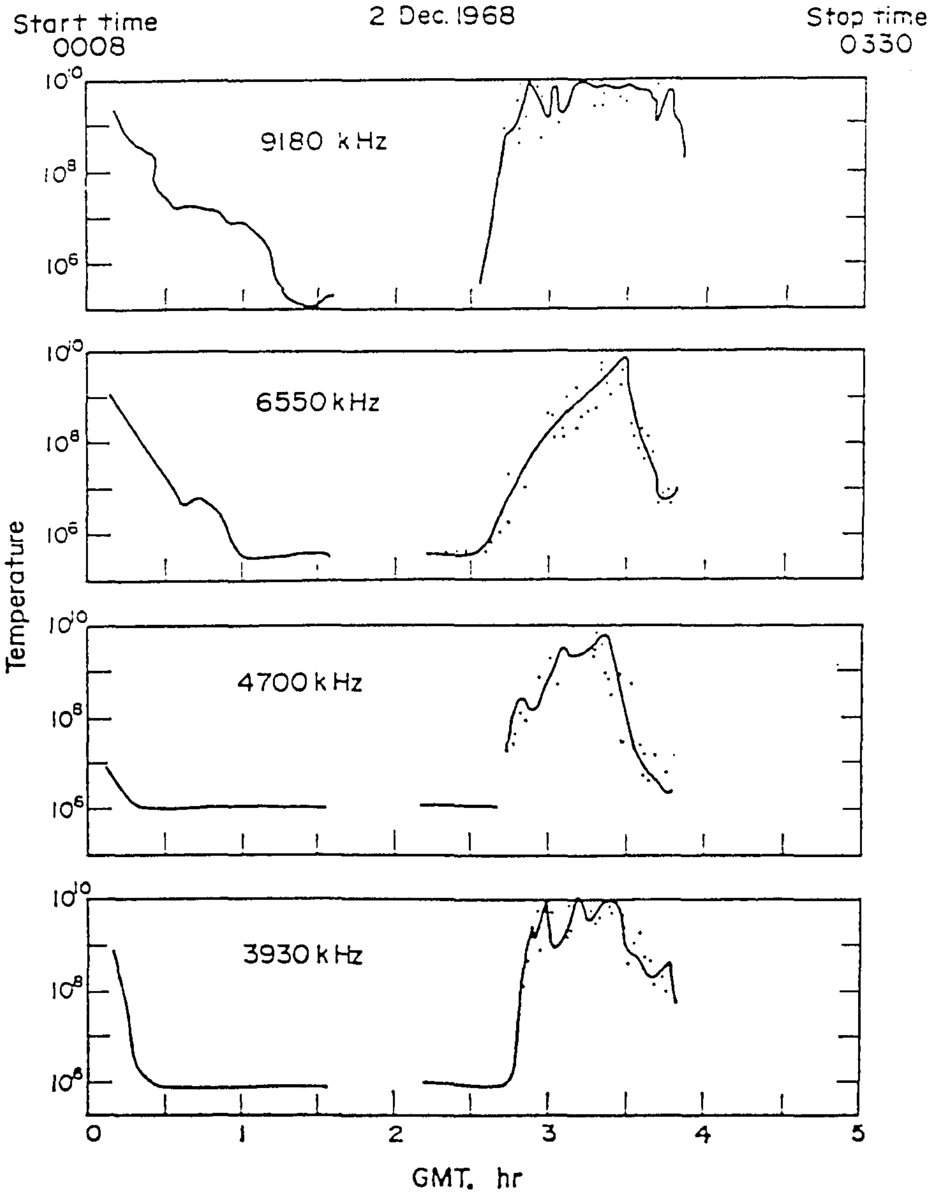

Figure 3-2 RAE-1 antenna temperature variations (from Herman, et al., 1973)

As to be expected, the discrete radio sources were narrowband and distributed throughout the entire spectrum. The discrete radio transmissions and broadband man-made noise tended to peak when the satellite was over populated areas, especially. The noise contours (in dB above 288 K) for 9.18 MHz are illustrated in Figure 3-3. Herman, Caruso, and Stone limited the data points to those collected between 00 and 08 hours local time (LT) (pre-daybreak, thus ensuring a transparent ionosphere). This map was the first worldwide view of the terrestrial radio noise as seen from space.

As seen in Figure 3-3, the data indicates that the most intense noise coincides with the major land masses, while the South Pacific is the fairly quiet. The data was taken in December, where it is winter in the northern hemisphere and summer in the southern hemisphere. There are intense noise regions over the landmasses, most likely coinciding with nighttime thunderstorms. For the northern hemisphere, few thunderstorms occur in December, so the detected noise appears to originate from urban areas. The highest level recorded was over China and the Eastern Mediterranean, where a number of higher power HF transmitters were located. It appears that discrete signals from ground-based transmitters were the primary noise sources over Eastern Europe and China.

Unfortunately, the data sets for both RAE-1 and RAE-2 satellites are no longer available for analysis (M. L. Kaiser, personal communication, 1994). Some RAE-2 hardcopy data was located at NASA Goddard Space Flight Center by the author, but its usefulness was marginal at best. In the more than 20 years ensuing since the RAE observations, the magnetic data tapes have deteriorated beyond use.

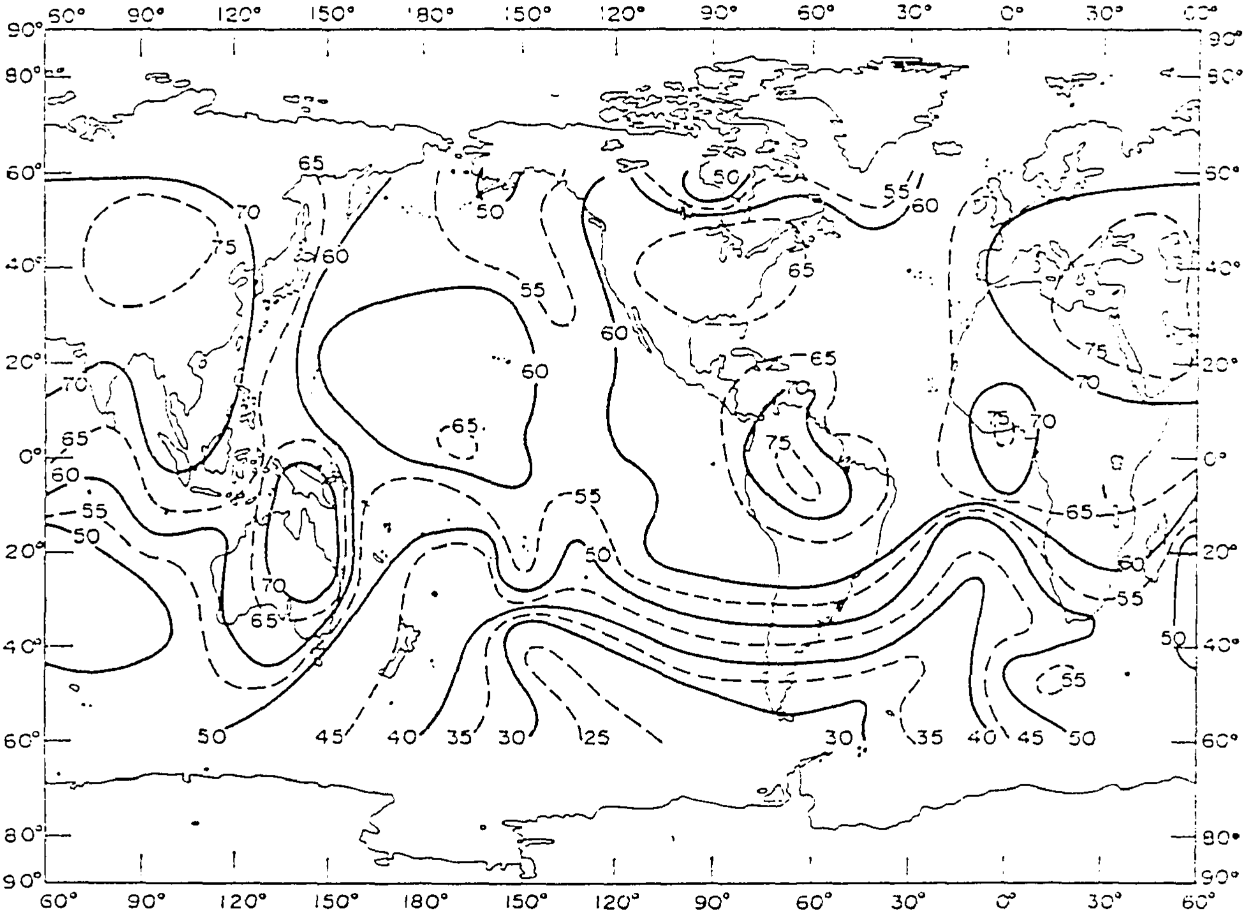

Figure 3-3 Worldwide noise contours at 9.18 MHz for 00 to 08 LT (from Herman, et al., 1973)

3.3 The Defense Meteorological Satellite Program (DMSP) HF Receiver

Terrestrial radio noise at satellite heights had also been studied using one of the Defense Meteorological Satellite Program (DMSP) series of satellites, launched in 1977. An experimental HF receiver on board was intended to measure terrestrial noise over the range of 1.2 to 13.9 MHz. The data would be used to extract the ionosphere's foF2 at the subsatellite point (Rush, et al., 1978). The goal for the DMSP HF payload was to provide a more complete measurement of the global foF2 than was available at that time from ionosondes. The satellite was placed in an almost sun-synchronous orbit at 860 km in altitude, well above the peak of the ionosphere's electron density. Its orbital inclination was such that it could cover between ±70° in geographic latitude (which include almost all major cities and industrial centers on the planet). The satellite passed over locations containing known ionosondes. C. M. Rush and the other investigators were able to isolate 22 cases where the satellite was close enough (in time and space) to allow a direct comparison of the satellite observation with ground data. The DMSP measurement of foF2 was within 1.0 MHz of the ground measurements more than 80% of the time (Rush, et al., 1978).

The data was processed to create maps of signal strength (in terms of receiver terminal voltage) as a function of satellite location. The receiver continuously swept through the entire frequency range in 100 kHz steps (total of 128 channels); each scan took 32 seconds. The antenna used was a 1 meter dipole, which is very short (electrically) at HF. One of the major limitations with the DMSP data was that no overall system calibration was possible. All of the analysis was performed strictly in terms of receiver terminal voltage because no knowledge of the antenna's performance in the topside ionosphere was available. This has limited the observations to qualitative assessments of the spatial and temporal dependencies of the HF noise.

Rush, et al. (1980) presented their analysis of the DMSP measurements for 4.0 - 13.9 MHz, and found that the results were consistent with the hypothesis that the primary emission sources were discrete terrestrial transmitters. It is known that the ionosphere acts as a highpass filter, allowing only frequencies greater than the critical frequency of the F2 layer (foF2) to pass through. This filtering effect is also somewhat affected by the longitudinal separation of the ground-based source and the receiver in Earth orbit. Energy from a signal source would only reach a satellite if it were radiated from a point on the surface that was a function of the satellite orbit, ionospheric structure, and emission frequency. Because the ionosphere has horizontal gradients, it is possible for energy at a frequency lower than the subsatellite ionospheric foF2 to reach a satellite. Radio waves could also reach the satellite through ducting or multiple reflections, and this energy would appear to come from the vicinity of penetration, even though its original source could be located quite far away. That noise was reaching the satellite via these propagation methods was supported by the DMSP receiver measurements. Rush, et al., expected that was especially true for conditions at dawn, when large horizontal electron density gradients are present.

Three month averages of the DMSP data supported the RAE discoveries, and accounted for some of the noise characteristics. The greatest noise intensity was found over Eurasia and Eastern Asia. These areas had consistently high overall noise levels, with "hot spots" at different frequencies. The DMSP receiver detected the strongest signals for those frequencies closest to those allocated to the fixed communications services (broadcasters). Australia was the quietest land mass, although it too had large noise densities at 12, 13, and 13.5 MHz. The North American hot spots were located along the coasts, which also happen to be the locations of several HF broadcasters.

The DMSP receiver discovered that noise levels were highest near bodies of water and the noise peaked for those receiver frequencies closest to the maritime mobile frequency allocations. The ocean areas were the least noisy. C. M. Rush had surmised that if the predominant noise source was from discrete terrestrial transmitters, then the receiver output should peak over populated land areas (personal communication, 1994). The intensity of man-made emissions is related to the amount of industrial activity, and this, in turn, is a function of technological sophistication.

Rawer (1967) had estimated the intensity of man-made emissions for the topside of the ionosphere, and concluded that at that time, the noise from industrial activity was less than the atmospheric noise contribution. The DMSP noise measurements showed little agreement with the CCIR world maps of radio noise. The HF receiver integrated out any bursts shorter than 250 milliseconds in duration, so it was much less sensitive to atmospheric electrical discharges. On the other hand, manmade industrial noise and discrete spectral components from broadcasting services would tend to be turned on for periods longer than 250 milliseconds. Overall, there was a general agreement between the measured noise levels and the allocated HF spectrum.

Data from the HF receiver was never archived (C. M. Rush, personal communication, 1994), since it was considered an experimental payload. Because of the calibration difficulties associated with the HF antenna, the principal investigators for this project never pursued any follow-on HF payloads to the DMSP series.

3.4 The AMPTE/IRM Plasma Wave Receiver

Until November, 1994, the AMPTE/IRM noise observations were the only archived data on terrestrial HF noise. The Active Magnetosphere Particle Tracer Explorer/Ion Release Module (AMPTE/IRM) spacecraft was not intended to study the terrestrial noise environment

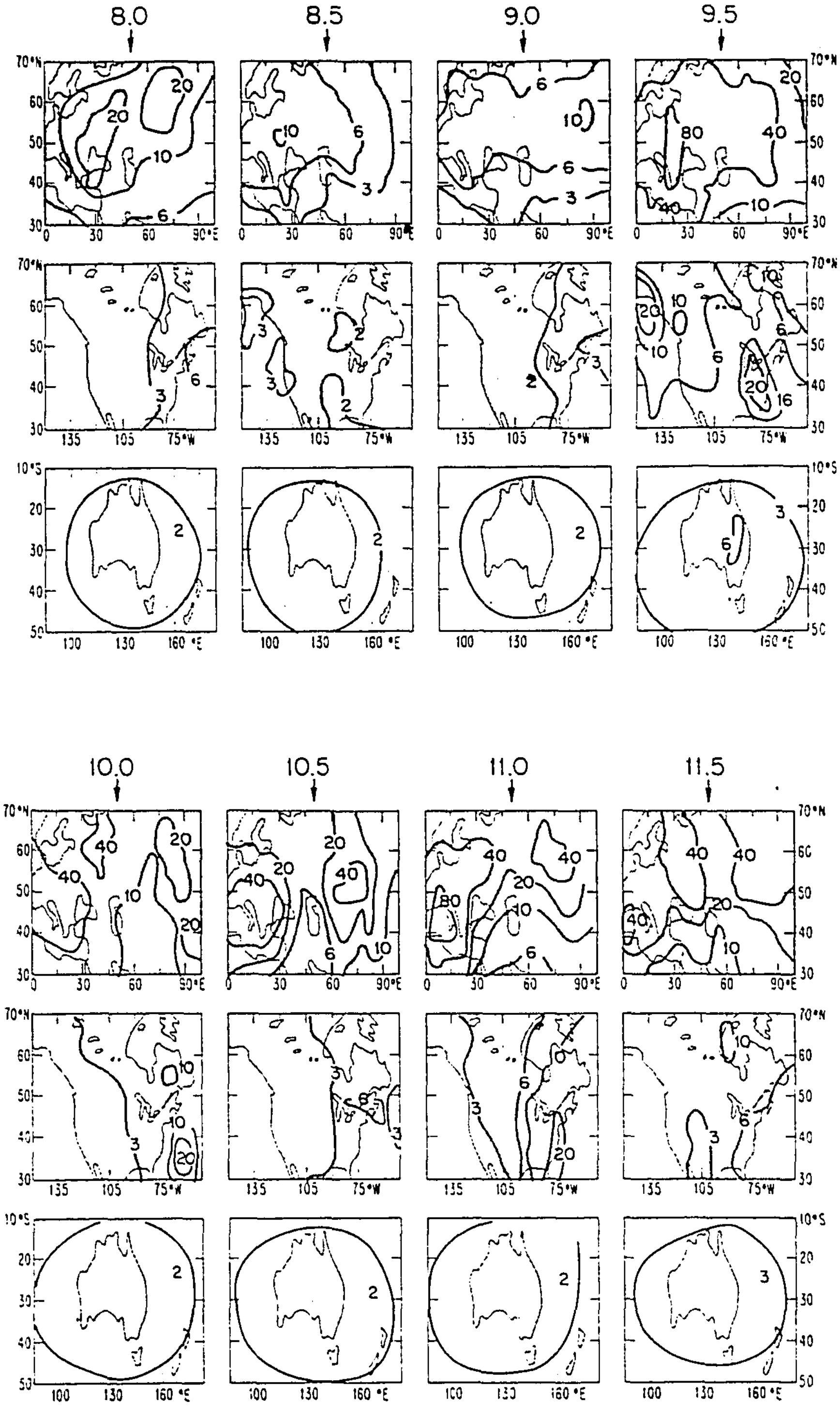

Figure 3-4 DMSP HF noise contours (from Rush, et al., 1980)

(LaBelle, et al., 1989), but its Plasma Wave receiver did detect some interesting signals which could only be terrestrial in origin. This satellite, designed to study the dynamics of the ionosphere and magnetosphere, was placed in a highly elliptical orbit: the apogee was 18 R_E (120,000 km) and perigee was 550 km. Part of the satellite's mission was to measure the Auroral Kilometric Radiation (AKR) and its harmonics, so its operating frequency range was set at .1 - 5.6 MHz. However, during times when the AKR was very weak or absent, AMPTE detected bursts of noise at frequencies between 3.0 - 5.6 MHz which were 35 dB higher than the galactic background. The satellite was also equipped to release materials which generated plasma clouds, allowing for a controlled study of plasma waves (Häusler, et al., 1985).

The Plasma Wave payload on board the AMPTE/IRM spacecraft was dedicated to measuring dc electric fields, electrostatic, and electromagnetic waves in the magnetosphere and solar wind environment (Häusler, et al., 1985). The antenna used was a 47 meter (tip-to-tip)dipole. The HF stepped-frequency receiver operated from 100 kHz to 5.6 MHz in 42 discrete steps; each receiver center frequency had a 10 kHz bandwidth. The frequencies of particular interest to the terrestrial HF noise issue are 3.23 MHz to 5.65 MHz, comprising seven channels, approximately 400 kHz apart (E. Lund, Dartmouth College, personal communication, 1994).

The burst data was processed by taking 10 minute averages of the 1.0 - 5.6 MHz spectrum for 2- to 3-hour periods, at two or three day intervals, for an entire year. Times of strong AKR were excluded. Radial distance effects were minimized by considering only data at 15-18 R_E. Wave intensities for the 2.0 - 3.0 MHz part of the spectrum remained fairly constant throughout the year; there appeared to be very little variation between the 10 minute averages. However, for data collected between 3.2 - 5.6 MHz, there is a distinct time dependence. When the satellite was near local noon time (a time when the ionosphere is densest), measurements from these channels were at almost uniformly minimum values; away from local noon time, the wave intensities were larger, with higher variations between the 10 minute intervals and bursts of constant frequency lasting from a few minutes to many hours. This can be attributed to the influence of ionospheric shielding; at times away from local noon, the ionosphere will be less dense, allowing more interference to penetrate.

An extensive survey of all data collected during times of weak or non-existent AKR have led LaBelle, et al. to conclude that the Plasma Wave instrument data at 2.82 MHz and below is most likely due to the galactic background noise.

At 3.23 MHz and above, the noise bursts detected have higher amplitudes when the satellite is closer to Earth, indicating a source related to the Earth. Also, the sharp slope of the turn-on and turn-off implies ionospheric breakthrough of just a few transmitters in each particular band. Stray signals from over-the-horizon radar, which operate at high power levels in this frequency range, would also be consistent with these measurements. Some sample two-minute averaged data are shown in Figure 3-5.

The Plasma Wave instrument data is currently archived in the Physics and Astronomy Department of the University of Iowa[1].

3.5 Summary

A direct comparison between the RAE-1, DMSP, and AMPTE/IRM data is difficult at best. The RAE results are in terms of antenna temperature, with no assumptions regarding the source. The DMSP receiver data were presented in terms of receiver output voltage;

---

[1] Access arrangements can be made through R. R. Anderson at (319) 335-1924.

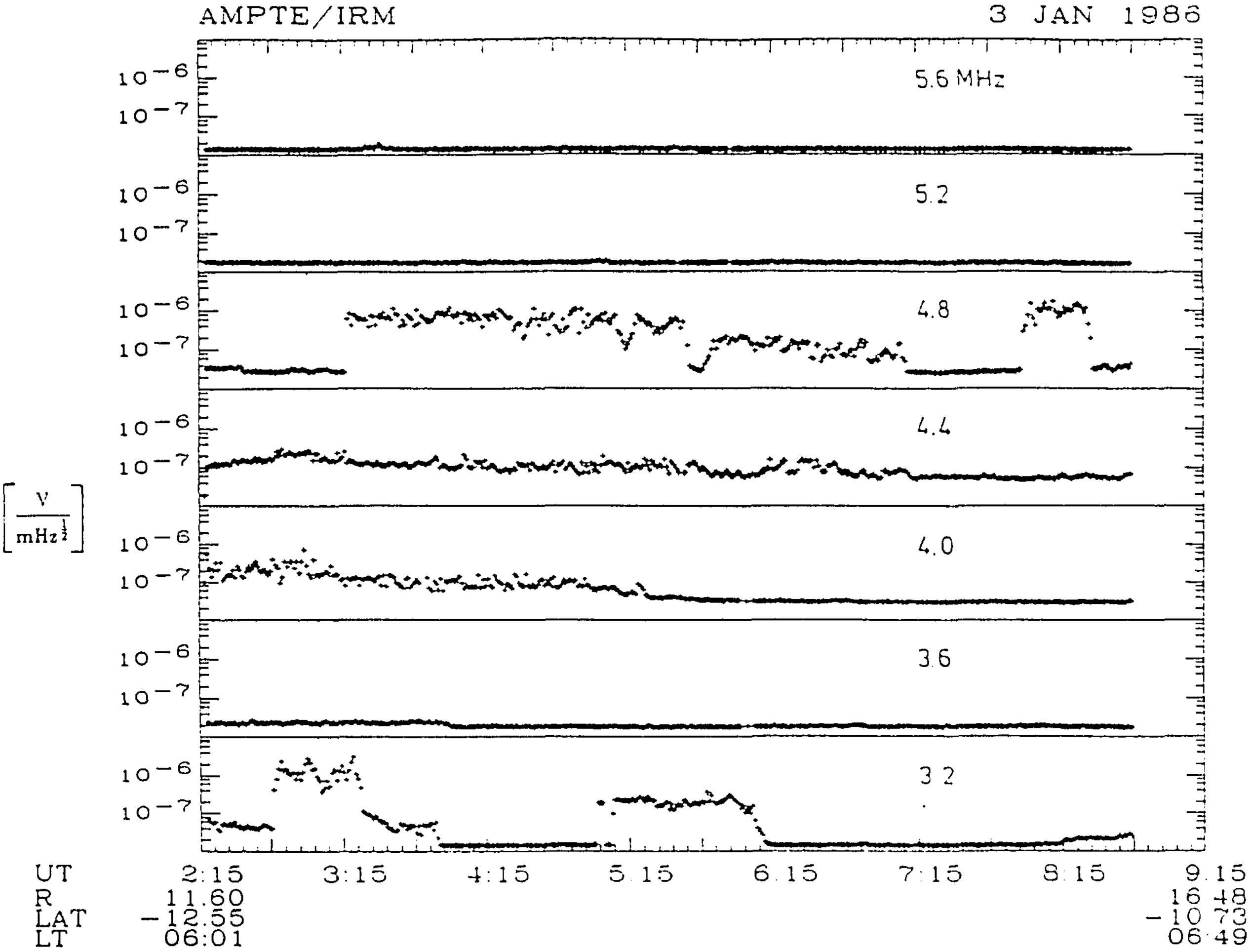

Figure 3-5 AMPTE/IRM Plasma Wave HF multichannel data (January 3, 1986) (from LaBelle, et al., 1989)

operational constraints prohibited obtaining the DMSP antenna performance, so noise temperature or field strength calculations can not be performed on the data (Rush, et al., 1980). The AMPTE/IRM data is in rms spectral density ($V/\sqrt{MHz}$). LaBelle has made some assumptions regarding the sources detected by RAE-1 in order to attempt a comparison between the AMPTE and RAE measurements. The RAE receiver recorded antenna temperatures of 10^9 - 10^{10} K as the satellite passed over the Earth's night side, and receiver temperatures of 10^6 K on the day side (Herman, et al., 1973). LaBelle assumed that the daytime levels measured by RAE were equivalent to the galactic background level -- making the key assumption that the ionosphere was essentially opaque to terrestrial noise on the day side. The nighttime RAE power levels were then adjusted according to this assumption. Further scaling to adjust the flux densities to those expected at 15 R_E gives approximate RAE measurements of 1.3×10^{-18} W/m^2Hz. In comparison (adjusting for different filter bandwidths and averaging times), the maximum level measured by AMPTE is approximately 1.5×10^{-16} W/m^2Hz. Despite the adjustments, there is still a 20 dB difference between the two measurements. The conclusion reached by LaBelle is that either the levels detected by RAE are quite a bit below the actual terrestrial noise levels or the background noise levels have increased by about 20 dB in the 15 or so years between the RAE and AMPTE measurements. Given the increase in technological development in the ensuing years, it is highly likely that the increase in detected noise is real.

CHAPTER 4
HF NOISE DETECTED BY WIND

4.1 The WIND Mission

The WIND spacecraft was launched into Earth orbit on November 1, 1994 to study the solar wind (hence its name) and geospace. Onboard the satellite is a payload called WAVES, which contains a number of scientific instruments. The WAVES investigation provides a comprehensive coverage of radio and plasma wave phenomena in the magnetosphere and interplanetary medium (IPM) (Bougeret, et. al., 1995). The WAVES payload was a joint effort of the Paris-Meudon Observatory, the University of Minnesota, and the NASA Goddard Space Flight Center. A photograph of WIND can be found in the IEEE Spectrum magazine, June, 1995 (p. 67).

The instruments in WAVES cover frequencies from fractions of a Hertz up to almost 14 MHz. One aspect of the scientific mission of WIND is to study the acceleration of particles in the solar wind created by solar active regions that continuously eject mildly energetic electrons. These events can be detected by their associated radio emissions, which fall in the ≈ 1-14 MHz frequency range. The instrument's HF receiver (known as RAD2), which covers the 1.075 - 13.825 MHz frequency range, was designed to study the electromagnetic signatures of these events. Note that this frequency coverage nicely overlaps with the terrestrial noise measurements discussed in Chapter 3.

Prior to the spacecraft's reaching its intended position at the Lagrangian L1 equilibrium point between the Sun and Earth, WIND made a number of highly elliptical orbits for a gravity assist to the L1 point (M. L. Kaiser, personal communication, 1995). The orbit apogee was approximately 80 Earth radii (R_E) and the perigee was approximately 1.5 R_E. Figure 4-1 illustrates the WIND orbit for November 16 through November 30, 1994. The x and y axes of the plot are in units of R_E. The days are marked by their calendar day number (November 16 is day number 320). The spacecraft is oriented such that its spin axis is always pointed toward the ecliptic pole. Coolers are located on the "top" and "bottom" of the spacecraft, pointed away from the Sun to avoid damage to its cooling capability (M. L. Kaiser, personal communication, 1995).

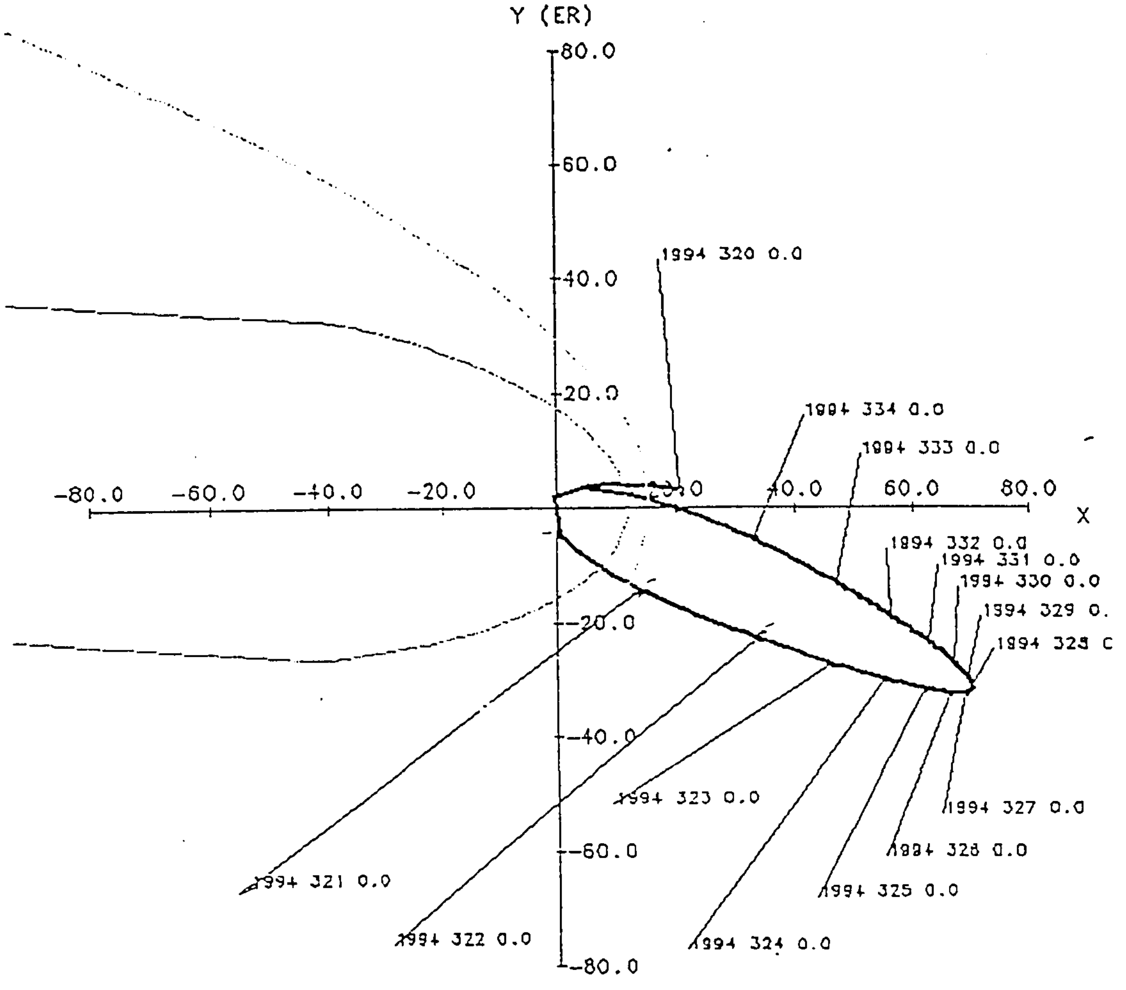

Figure 4-1 WIND spacecraft orbit configuration

The electromagnetic sensors on board use three mutually orthogonal dipoles. Two, denoted E_x and E_y, are in the spin plane of the spacecraft. The third, E_z, is along the spin axis. E_x is 100 meters tip-to-tip and used for the low frequency FFT and thermal noise receivers in WAVES. E_y is 15 meters tip-to-tip. The spin axis dipole, E_z, is 12 meters tip-to-tip and pointed toward the South ecliptic pole. Each antenna has a preamplifier located as close to its base as possible to minimize the effect of the antenna's base capacitance (Bougeret, et. al., 1995). The two short dipoles (E_y and E_z) are used as inputs to RAD2. Two modes exist, SUM (the two antenna inputs are summed together) and SEP (the two antenna inputs are kept separate). All data analysis has been carried out using the SEP mode. A simple functional diagram for RAD2 is shown in Figure 4-2.

The most important RAD2 characteristics are listed in Table 4-1 below. As can be seen from Figure 4-2, the RAD2 receiver is a superheterodyne receiver; it uses a dual conversion scheme with an intermediate IF of 21.425 MHz.

Table 4-1 Important RAD2 performance parameters

Antenna lengths	Ey = 15 meters Ez = 12 meters
Frequency	start = 1.075 MHz stop = 13.825 MHz
Channel characteristics	number of discrete channels = 256 3 dB bandwidth = 20 kHz spacing = 50 kHz
Scan time (all 256 channels)	18 seconds
Sensitivity	7 nV/√Hz

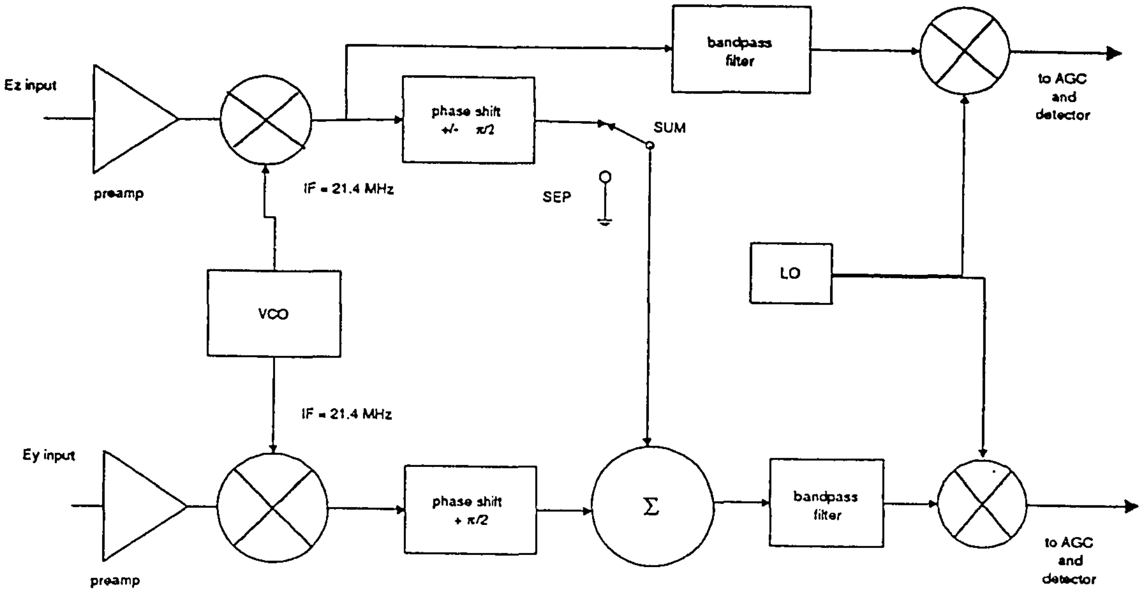

Figure 4-2 WIND spacecraft HF receiver (RAD2) functional diagram (adapted from Bougeret, et al., p. 18)

For the entire frequency sweep, the channel numbering scheme is

$$\text{chan} = {}^{(\text{freq} - 1.075)}\!\diagup_{.05} \tag{4-1}$$

where chan is the channel number (ranging from 0 to 255), and freq is the input frequency in megaHertz. The factor of .05 represents the 50 kHz spacing between channels. Valid receiver frequencies are limited to 1.075 MHz plus multiples of 50 kHz. The SUM mode, which combines the signals from the Ey and E_z antennas, essentially synthesizes an inclined dipole. For a spin-stabilized spacecraft such as WIND, this mode is typically used to determine the direction of arrival of the received radiation (Bougeret, et. al., 1995). A frequency table is normally used to select 16 out of 256 possible frequencies for the measurements. However, from November 12 through December 3, the HF receiver continuously scanned all 256 channels to check out the functions of the receiver on board. It was during this three week period that RAD2 collected some very interesting data on terrestrial interference. The IF signal in RAD2 is amplified, detected, and digitized into an 8 bit word.

4.2 Data Calibration

The HF interference data detected by the RAD2 receiver on WIND is received in the form of telemetry units, which have a range of 0-255, corresponding to the 8 bit digitization. These telemetry units must be converted into something more meaningful, such as power spectral density. The group that built the RAD2 (University of Minnesota) has performed gain curve calibrations over the receiver's entire input frequency range. The gain curve response of the receivers has been modeled as a form of log law response (Bougeret, et. al., 1995):

$$y = A_2 \log_{10}\left[\left(10^{\frac{(A_1-x)}{10}} + 10^{-A_4}\right)^{\frac{1}{4}} + A_3\right] \tag{4-2}$$

where x is the input and y is the output of the receiver (in units of μvolts/$\sqrt{}$Hz). The factors A_1, A_2, A_3, and A_4 are calibration parameters that have been computed by numerically fitting the calibration data at 17 discrete frequencies. The calibration as it is performed at the NASA

Goddard Space Flight Center differs from that described in Bougeret, et. al., 1995. The calibration procedure as it is implemented by the principal investigators at the Laboratory for Extraterrestrial Physics at Goddard converts the raw receiver output telemetry numbers into the equivalent signal in microvolts at the input to the receiver preamplifiers (i.e., at the base of the antenna). Only three A parameters are used, two of which are constant. These parameters are interpolated from the ground calibration data collected at the 17 discrete frequencies across the receiver's operational band. The calibration equation for the signal V′ in µV/√Hz is

$$V' = \mathrm{Voz2(f)} * 10\wedge\left[2 \cdot \log_{10}\left(10\wedge\left(\frac{\mathrm{TLM} - \mathrm{A3z2}}{\mathrm{A2z2}}\right) + 1\right) - \frac{\mathrm{A1z2(f)}}{20}\right] \tag{4-3}$$

A2z2 and A3z2 are the A2 and A3 factors for the E_Z mode of RAD2; these A factors are constant with frequency for this mode, although each mode for the RAD2 has a different set of A2 and A3 values. TLM is the telemetry signal value (in the range of 0 to 255). A1z2 is an array of 256 values interpolated from the ground calibration data; Voz2 is a frequency dependent conversion factor based on reference voltages measured across the operational frequency band (M. L. Kaiser, personal communication, 1995). These parameters are included with tables of antenna calibration parameters in an array called `cal_data` to calibrate the RAD2 output. Additional factors are included to convert from µV/√Hz to other physical units. The calibration and conversion routines were performed by scientists at the Laboratory for Extraterrestrial Physics and external consultants fro the WIND spacecraft.

Because the response is nonlinear, the calibration program used at Goddard includes the warning that telemetry data values greater than 240 (out of 255) may be invalid. Usually, at intensities this high, there is a high probability that the data may be corrupted by the receiver's own nonlinearities. When that happens, other data channels would also be affected.

4.3 Data Analysis

1994 and 1995 are years that happen to fall at a solar cycle minimum. The ionosphere's peak plasma frequency during the day is about 5-6 MHz. At night, it falls to 1-2 MHz. As a consequence of WIND's orbit, at all times except perigee, the spacecraft always viewed the daylit side of the Earth. The subsatellite point usually was at 0900 - 1000 (LT). At perigee, the spacecraft was on the nightside. A cursory view of the RAD2 spectrograms illustrates the effect of the plasma frequency. Intensity is displayed on a scale of black (weakest) to red (strongest). For example, in Figure 4-3, note that the lowest frequency reliably observed is about 6 MHz. In Figure 4-4, the brighter section of the spectrogram represents the data collected during a perigee pass. At this point, the receiver has gone into saturation and all data channels are "blinded" by the strong HF interference. The implications of these spectrograms will be discussed in the following section. The x axis of the spectrograms is "spacecraft event time" (SCET), which is essentially the same as Universal Time (UT) (also equivalent to Greenwich Mean Time). Local time (LT) can be determined by adding 1 hour to UT for every 15° longitude separation. The y axis of the spectrogram is frequency. While impossible to discern from the plots directly, all 256 channels are displayed. An overall summary of the interference characteristics are presented in Table 4-2.

It is important to be able to analyze the data and manipulate it to extract meaningful information on terrestrial interference. The data was read in using the IDL data analysis package and processed along with the `cal_data` array, and the results presented in terms of log flux density (in dB above Galactic background noise). The appendix has a listing of `rad2dsp.pro`, the IDL routine which produces the spectrograms. This program was written by Michael Kaiser of the Laboratory for Extraterrestrial Physics at Goddard Space Flight Center. All results are presented using the Galactic background noise level as a reference.

Table 4-2 Interference characteristics

Frequency range	Interference range[a]	Percent time[b]	Earth location
0 - 6 MHz	0 -7 dB	12%	Asia, India, FSU[c]
6 - 8 MHz	5 - 20 dB	75%	Europe, Asia
8 - 10 MHz	5 - 20 dB	75%	Europe, Asia
10 - 12 MHz	15 - 30 dB	90%	Europe, Asia
12 - 13.875 MHz	0 - 15 dB	50 %	Eastern Europe, Asia

[a] In dB above the galactic background level.
[b] Over 24 hour period.
[c] FSU stands for the states of the former Soviet Union.

(M. Kaiser, personal communication, 1995). The Galactic background level is highly variable over the 1-14 MHz range covered by the RAD2 receiver (Novaco and Brown, 1978). Rather than applying a mathematical model of the background emission, the background is calculated directly from the data set prior to conversion from telemetry units to spectral density. A histogram of the signal intensity is generated for each receiver channel. Figures 4-5 and 4-6 are examples of such a histogram and the time series of the associated signal. The channel shown is 7.25 MHz on November 17, 1994. Note that the histogram is bimodal; the Galactic background level is the sharp peak of intensities at the smaller telemetry unit values (M. Kaiser, personal communication, 1995). The broader, lower peak is the distribution of signal intensity associated with the man-made signal. The underlying assumption is that the minimum signal level from the "quiet" channels is the nonthermal Galactic background radiation (M. L. Kaiser, personal communication, 1995). The principal investigators on the WAVES payload have determined that using the data itself to extract the galactic background level may be the best way to provide a reference for the RAD2 signals. This method eliminates the requirements for models (empirical or other) of the galactic background. An analysis of raw telemetry data histograms has verified that the behavior of the sharp peak thought to be associated with the galactic background radiation appears to follow the frequency dependence described by Novaco and Brown (1978).

The time behavior of specific channels must also be considered, since it can allow extraction of quantitative data on the intensity of the HF interference. Additional analysis routines for the RAD2 data were written in the IDL programming language by the author to extract specific data channels or instances in time and study their behavior. These programs are also listed in Appendix A. While the spectrograms are useful in determining an overall structure to the interference intensities, they are not very useful for direct comparisons with the measurements taken by the previous spacecraft. To this end, specific channels were extracted from the data sets and analyzed for specific characteristics. For comparison, time series from channels closest in frequency to the RAE-1 RV receiver (3.925, 4.725, 6.525, and 9.225 MHz) for December 2, 1994 are shown in Figure 4-7. Note that the start and stop times are the same as those presented for RAE-1. Refer to Figure 3-2 for the RAE-1 antenna temperature variations. The behavior, however, is not the same as that detected by RAE-1. One factor to consider is the distance of the WIND spacecraft from the Earth. At the times shown for December 2, 1994, the spacecraft was moving radially away from the Earth. From 0000 to 0500 hours UT, it was approximately 20 to 25 RE away. This will introduce an additional attenuation of about 26 dB. However, total intensity aside, the shape of the signals over the time period shown does not appear similar either. The general trend over the frequencies covered also does not appear to be similar. This can be attributed to the fact that the field of view for the WIND spacecraft is an entire hemisphere, unlike the field of view for the RAE-1. Consequently, a number of differennt sources are detected within WIND's field of view during the dwell time of the receiver.

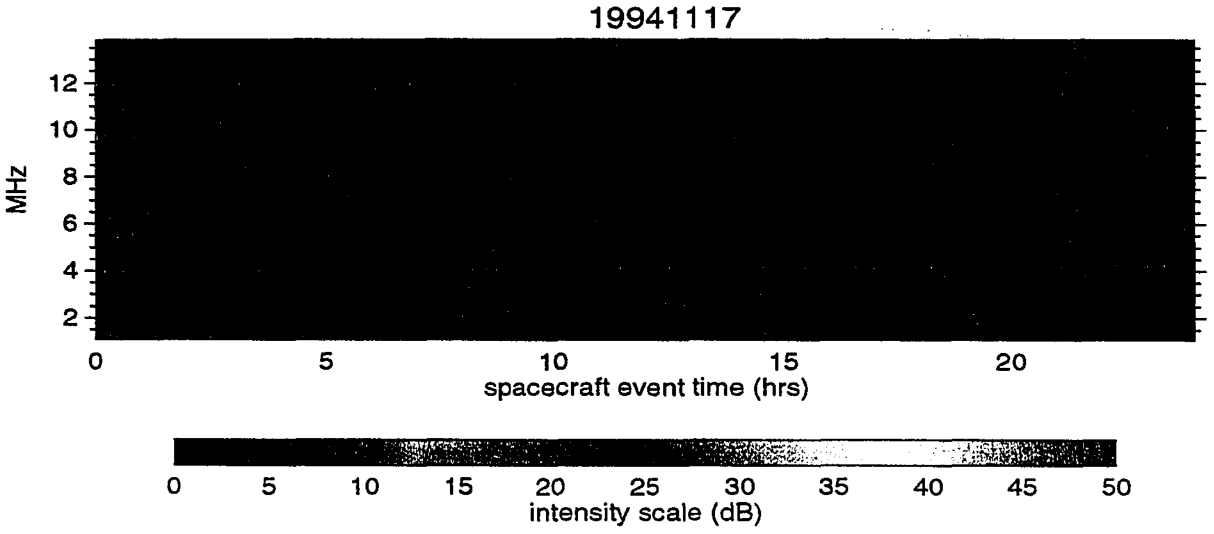

Figure 4-3 WIND RAD2 spectrogram for Nov. 17, 1994 (typical observation day)

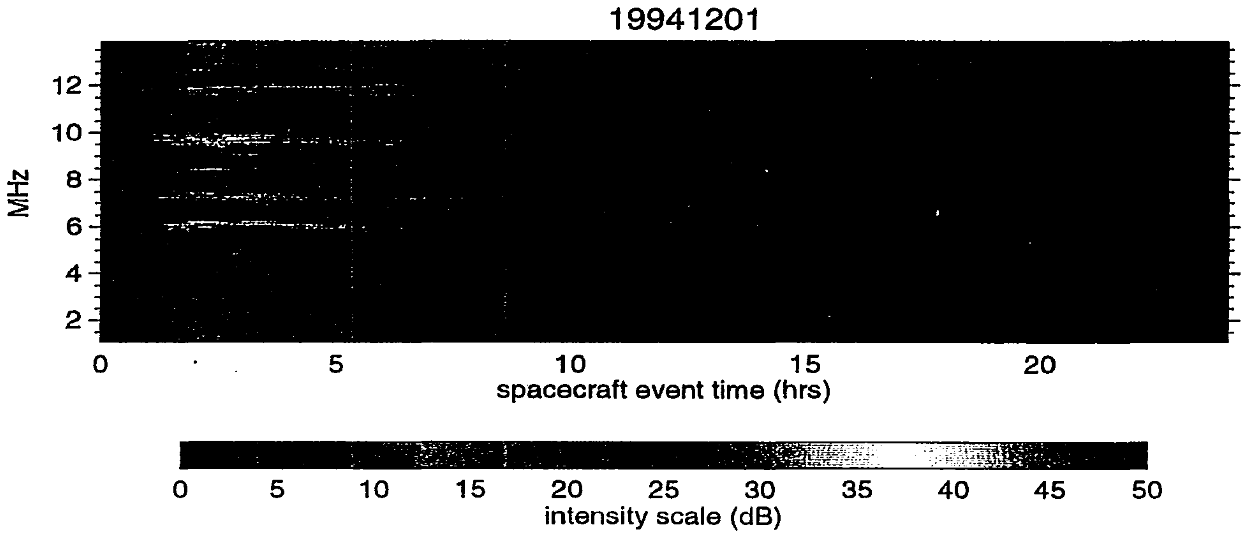

Figure 4-4 WIND RAD2 spectrogram for Dec. 1, 1994 (perigee pass)

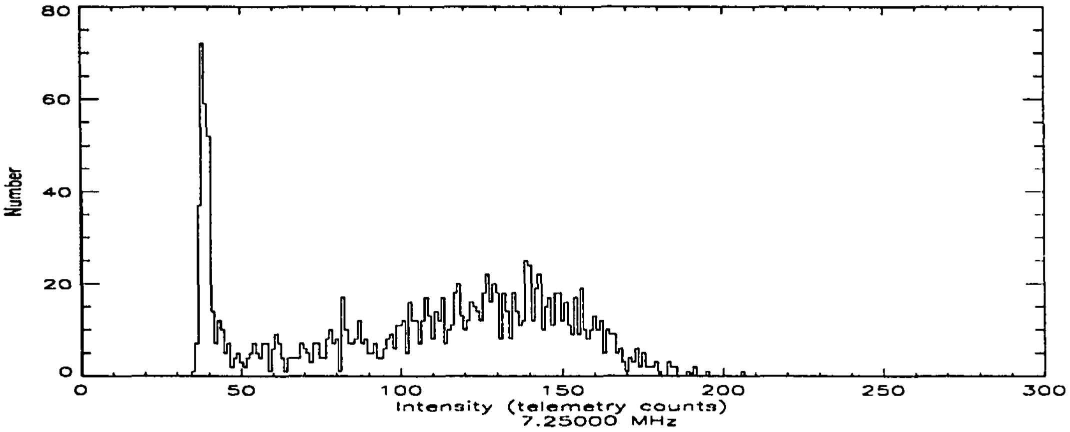

Figure 4-5 Histogram for 7.25 MHz signal detected on November 17, 1994

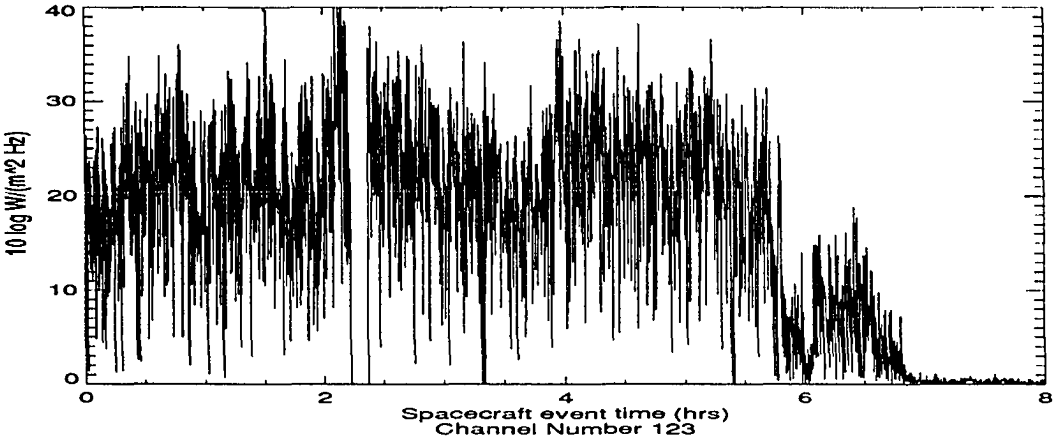

Figure 4-6 Time series for the 7.25 MHz signal

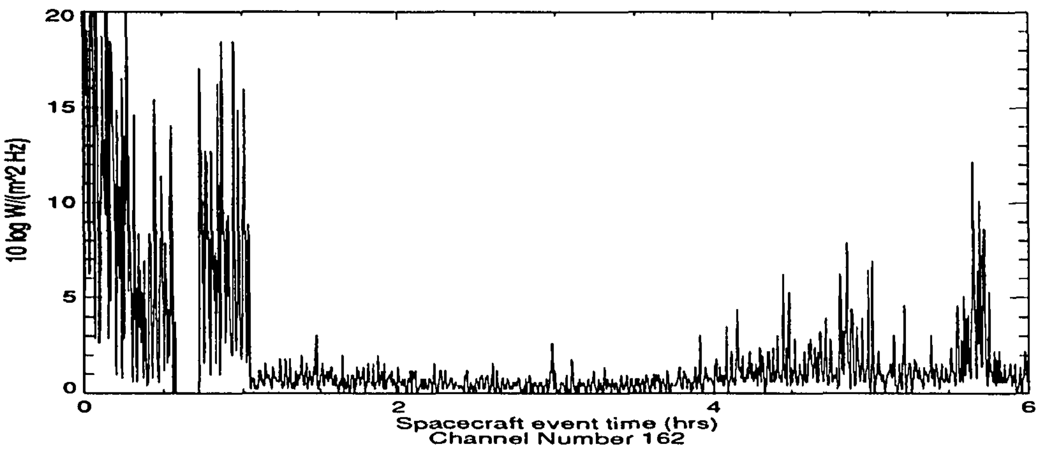

(a)

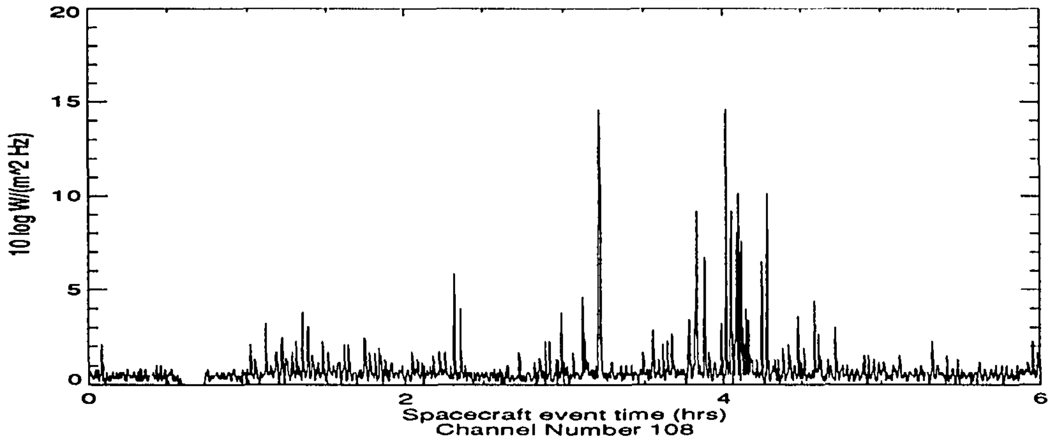

(b)

Figure 4-7 Time series extracted from RAD2 data: a) 9.225 MHz; b) 6.525 MHz

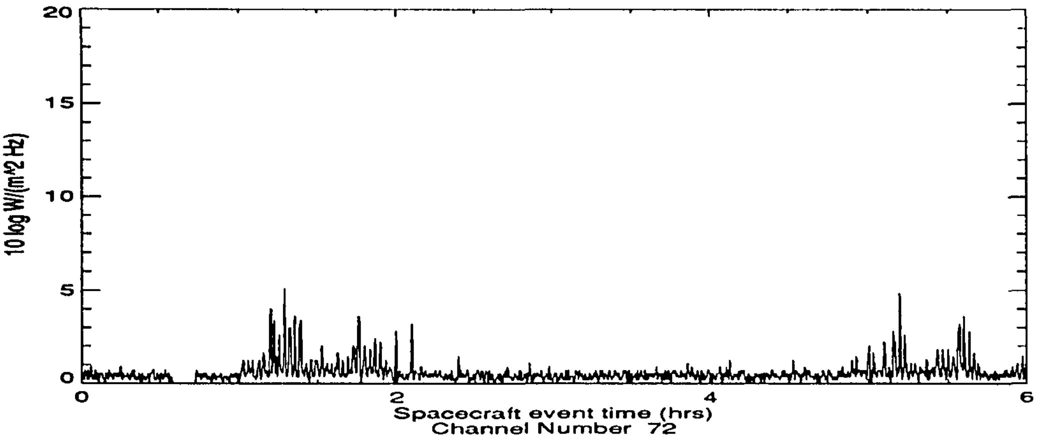

(c)

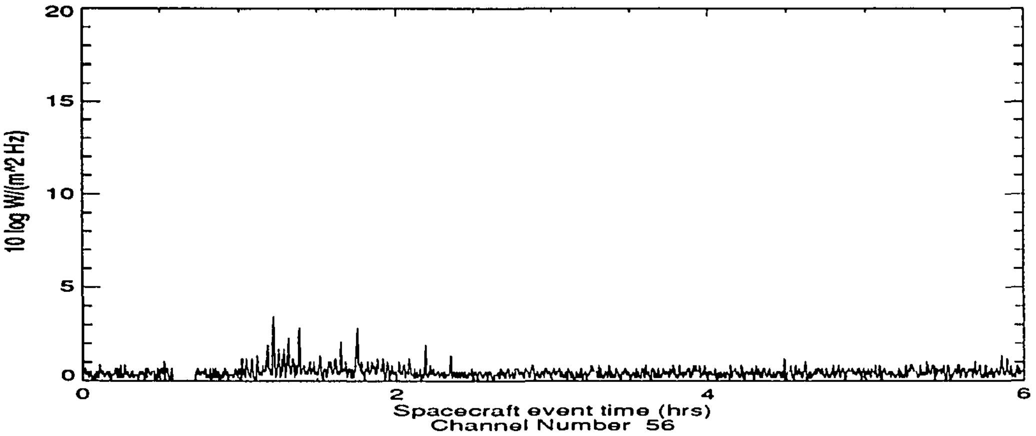

(d)

Figure 4-7 (continued): c) 4.725 MHz; d) 3.925 MHz

There are other examples in the data where a distinct turn-on and turn off phenomena can be observed. The fall times for such cases can not be attributed to the sources simply moving out of view of the spacecraft. Signals have also been observed turning on and off at specific times, implying a signal source with a broadcast schedule. Such behavior rules out the possibility of natural phenomena that may be turning on or off within view of the spacecraft. The signal fall times occur within one frequency scan period (18 seconds), as illustrated in Figure 4-8. This signal was detected by RAD2 while the WIND spacecraft was over North America. It has been identified as a BBC relay station in Delano, CA, transmitting 250 kW at 6.130 MHz. The broadcast time has been verified by the station engineer (M. L. Kaiser, personal communication, 1995).

A 24 hour scan for one of the common broadcast channels is presented in Figure 4-9. The large spike near 0200 hours is anomalous. It is in almost every data set at approximately the same spacecraft event time. This spike may be a byproduct of the spacecraft's downlink coupling into the experiments. The other amplitude variations can be attributed to terrestrial broadcast signals .

The data correlation was also questioned during the analysis. Autocorrelations were performed on select channels to determine the stationarity of the noisy signals and possibly determine what effect the variable ionosphere had on the signals propagating through it. The autocorrelation was performed using the formula (Chatfield, 1989)

$$r_k = \frac{\sum_{t=1}^{N-k}(x_t - \overline{x})(x_{t+k} - \overline{x})}{\sum_{t=1}^{N}(x_t - \overline{x})^2} \tag{4-4}$$

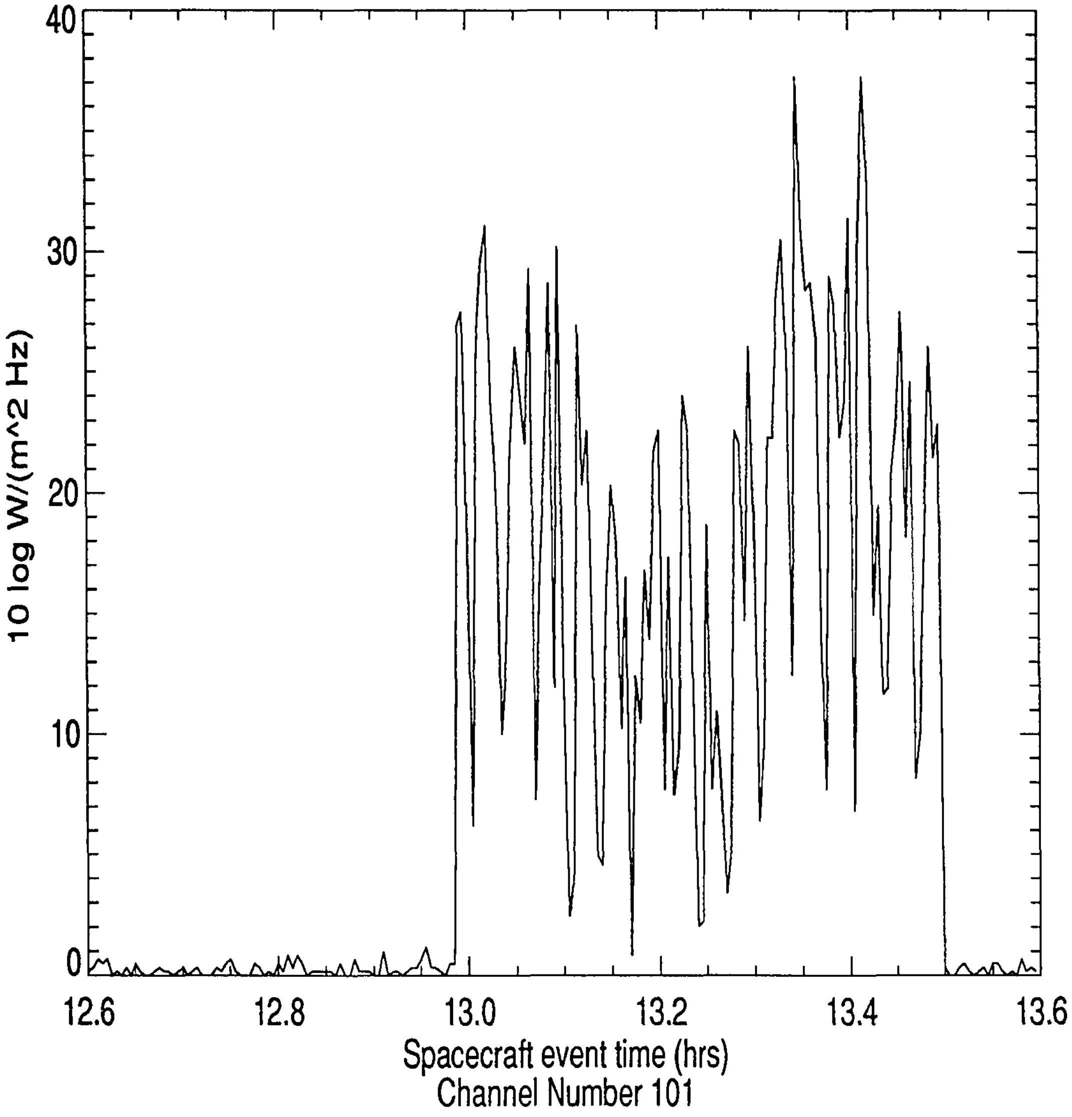

Figure 4-8 BBC (6.125 MHz) radio signal detected by RAD2 on December 2, 1994

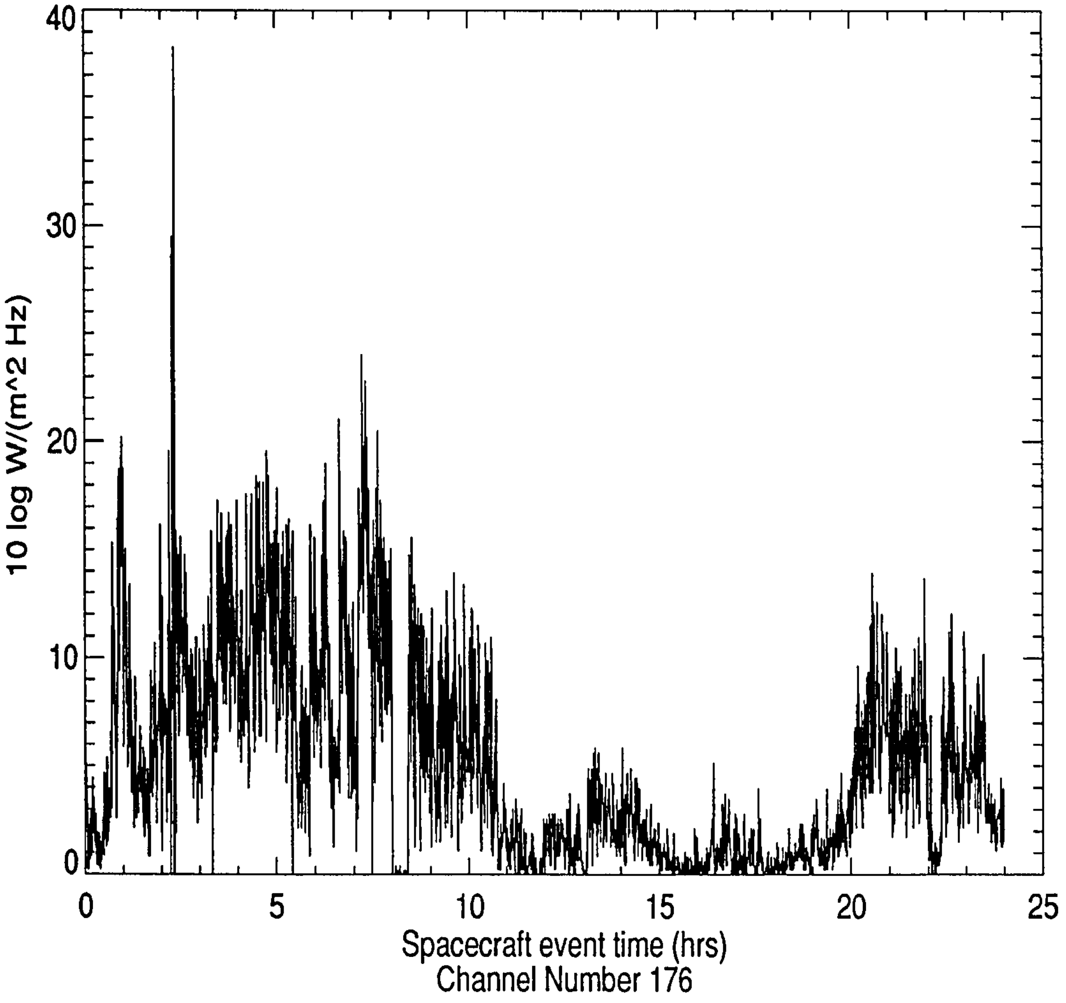

Figure 4-9 Time series extracted from RAD2 data: 24 hour scan of 9.9 MHz channel

where $\bar{x}$ is the mean, and the autocorrelation coefficient r_k plotted against the time lag k. The maximum value of k was chosen as (maximum number of data points)/3. Using the finest time resolution available in the data (18 seconds), this works out to a maximum k of 1600.

Examples of autocorrelations for November 17, 1994 are shown in Figures 4-10 (quiet channel) and 4-11 (noisy channel). The time series for quiet channel, 4.425 MHz, displays amplitude variations that appear random, except for a few weak, short-lived spikes. The autocorrelation supports this observation (the peak at lag $k = 0$ is not clearly visible on this scale). On the other hand, the noisy channel (7.225 MHz) shows a strong time variation, with some amplitude fluctuations that can clearly be attributed to terrestrial interference. The autocorrelation for this noisy channel indicates that these amplitude fluctuations are not solely due to random noise bursts. The autocorrelation is high for time lags less than 100. It is also important to remember that in this analysis, each correlation lag step represents a time delay of 18 seconds. For the correlation to remain high for a time lag of about 100 implies that the signal is somewhat correlated on time scales of less than 30 minutes -- approximately the duration of most of the broadcasts. The correlation has a smaller peak near $k = 450$, which corresponds to the broadcast signal near SCET = 2 hours.

Another factor that must be considered is how the signal variations in one channel correlate with other channels. This is especially true when strong signals at multiple frequencies are incident at an RF system containing active devices such as mixers and preamplifiers. The issue of the RAD2's nonlinear response is not a trivial one. An examination of the RAD2 spectrograms (Figures 4-3 and 4-4) seems to imply a relationship between several of the channels (e.g., 12, 10, and 2 MHz in 4-3 or 12, 8, and 4 MHz in 4-4). The existence of intermodulation distortion in the RAD2 output would complicate extracting meaningful results from the data sets. The distortion caused by the nonlinearities are usually

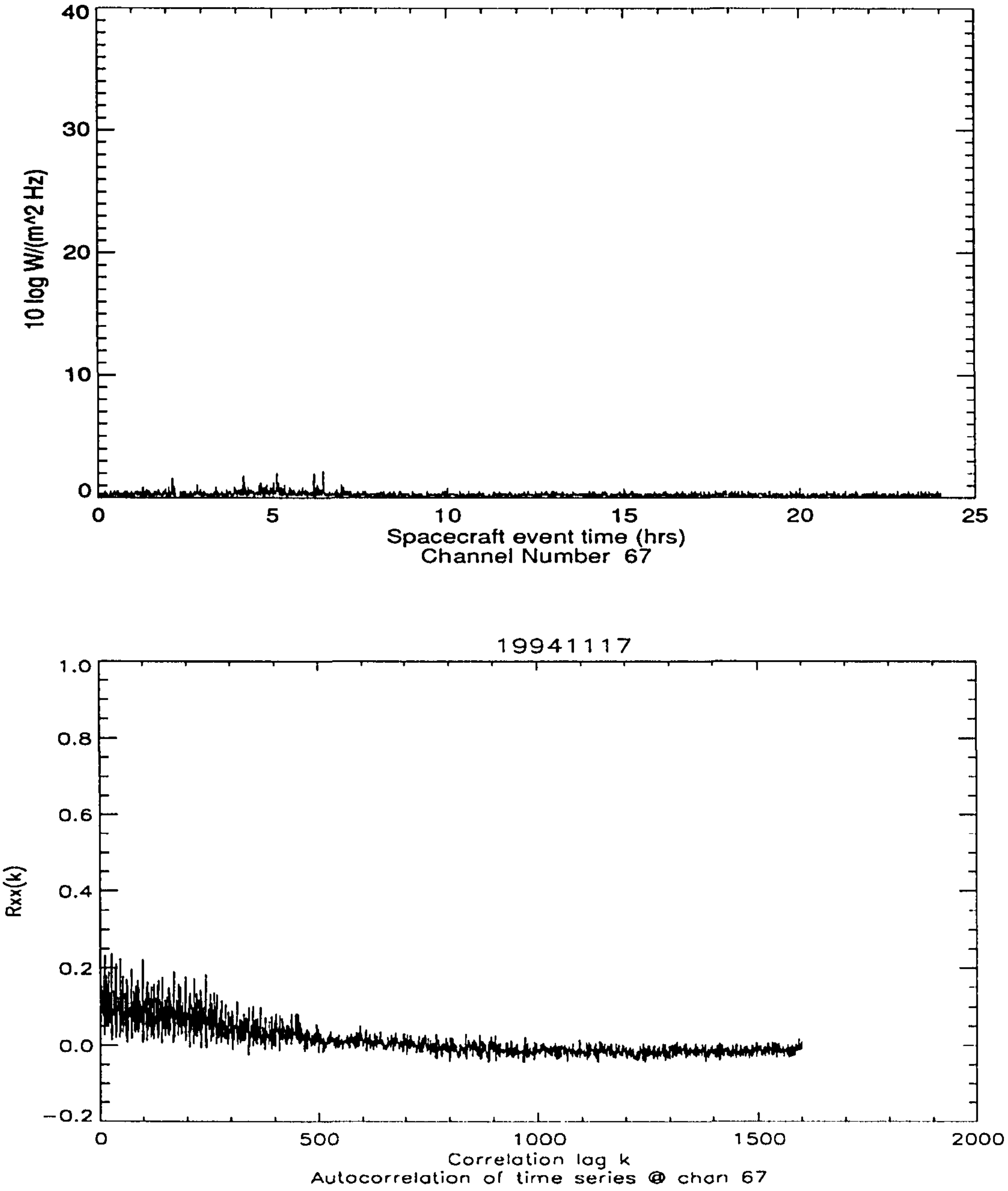

Figure 4-10 Time series (top figure) and autocorrelation (bottom figure) for 4.425 MHz

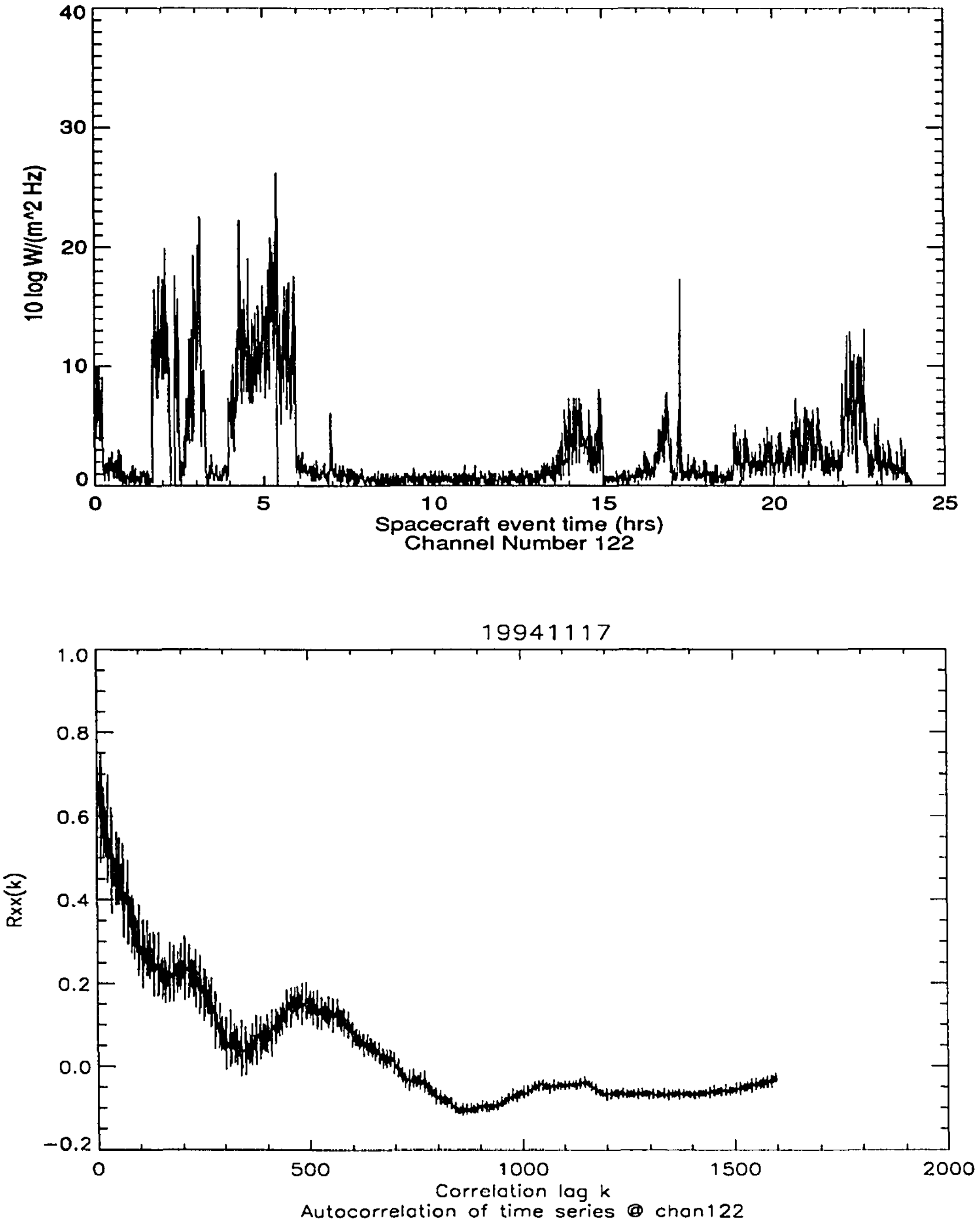

Figure 4-11 Time series (top figure) and autocorrelation (bottom figure) for 7.225 MHz

undesired, since intermodulation products and harmonics may often be confused for desired signals.

Intermodulation distortion is a result of the nonlinear character of active RF devices. A simple nonlinearity can be expressed as a three term power series (Ha, 1981)

$$e_o = k_1 e_i + k_2 e_i^2 + k3 e_i^3 \tag{4-5}$$

where e_i is the input to the nonlinear device or system, e_o is the output, and k_1, k_2, and k_3 are the coefficients controlling the nonlinear response of the device or system. In most devices or systems, the intermodulation output that causes most concern is the third order distortion output. Consider an input containing two signals of similar, large amplitudes but different frequencies, ω_1 and ω_2: $e_i = A(\cos \omega_1 t + \cos \omega_2 t)$. The output will contain a combination of the desired frequencies ω_1 and ω_2, as well as harmonics of the input frequencies, second order intermodulation products ($\omega_1 \pm \omega_2$), and third order intermodulation products ($2\omega_1 \pm \omega_2$ and $\omega_1 \pm 2\omega_2$).

The first concern in analyzing the data was whether intermodulation distortion was causing the apparent relation between certain channels. The harmonics of the input frequencies for the strongest terrestrial interference signals are outside the passbands of the filters in RAD2, so these are not an issue. This also applies to the second and third order intermodulation sum products. The RAD2 channelization is such that the second order difference product does not coincide with valid RAD2 channels. For example, if strong interence is present at 11.425 and 9.575 MHz, the second order intermodulation difference product would fall at 1.85 MHz, which is not a valid center frequency for RAD2. In fact, this frequency would not even fall within the passband of the IF filter used in RAD2. The situation is worse for the third order difference product. Considering again the two strong interference frequencies 11.425 and 9.575 MHz. Their third order difference products would be 13.275 and 7.725 MHz, both valid RAD channels.

This concern prompted a search for potential trouble spots in the data. The cross correlation was performed using the following formula (Chatfield, 1989):

$$r_{xy}(k) = \frac{\sum_{t=1}^{N-k} (x_t - \bar{x})(y_{t+k} - \bar{y})}{\sqrt{\sum_{t=1}^{N} (x_t - \bar{x})^2 \sum_{t=1}^{N} (y_t - \bar{y})^2}} \qquad (4\text{-}6)$$

$$k = 0, 1, \ldots N-1$$

Plots of the cross correlations for several channels taken from the December 1, 1994 data set (illustrated in Figure 4-4) are presented in Figures 4-12 through 4-15. The start time for the time series used in the cross correlation analysis differs from that used in previous time series. Data before 1000 hours will not be used because so many channels are occupied in the time span of 0000 to 1000 hours that any cross correlation could lead to false conclusions. The two noisy channels selected are 6.025 and 6.225 MHz. Two tone third order intermodulation products, if they existed, would be at 2(6.025)-6.225 = 5.825 MHz and 2(6.225)-6.025 = 6.425 MHz.

A visual inspection of the time series for each channel confirms that the signals do not appear correlated, despite the peaks at lags greater than 0. The peaks can be attributed to the general similarity in shape of the terrestrial interference. Large lag times correspond to large longitudinal separations (since 1 hour difference in UT is equivalent to 15° separation inlongitude) between the signal sources in the cross correlated channels, so it is unlikely that

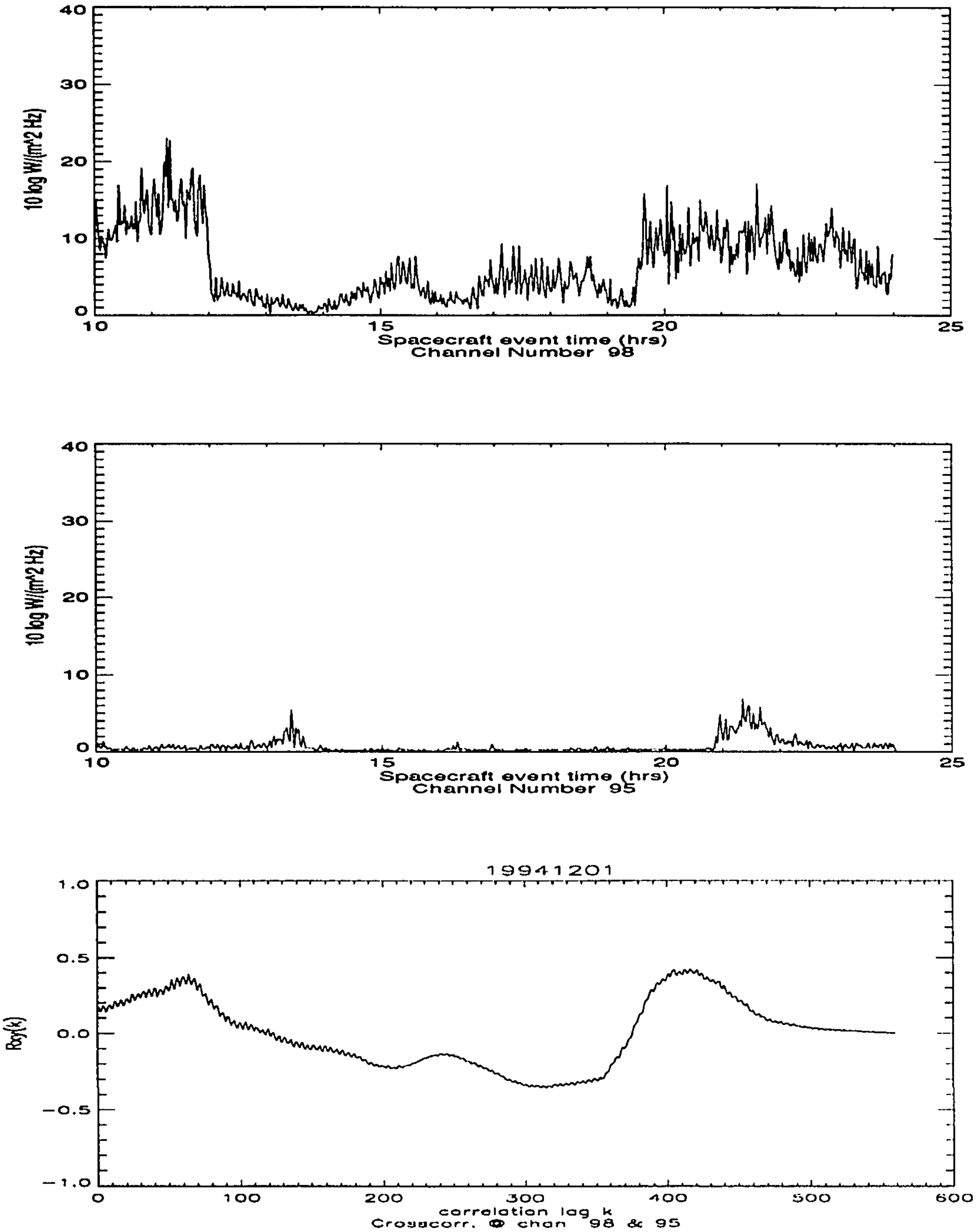

Figure 4-12 6.025 MHz (top) and 5.825 MHz (middle) time series and their cross correlation (bottom)

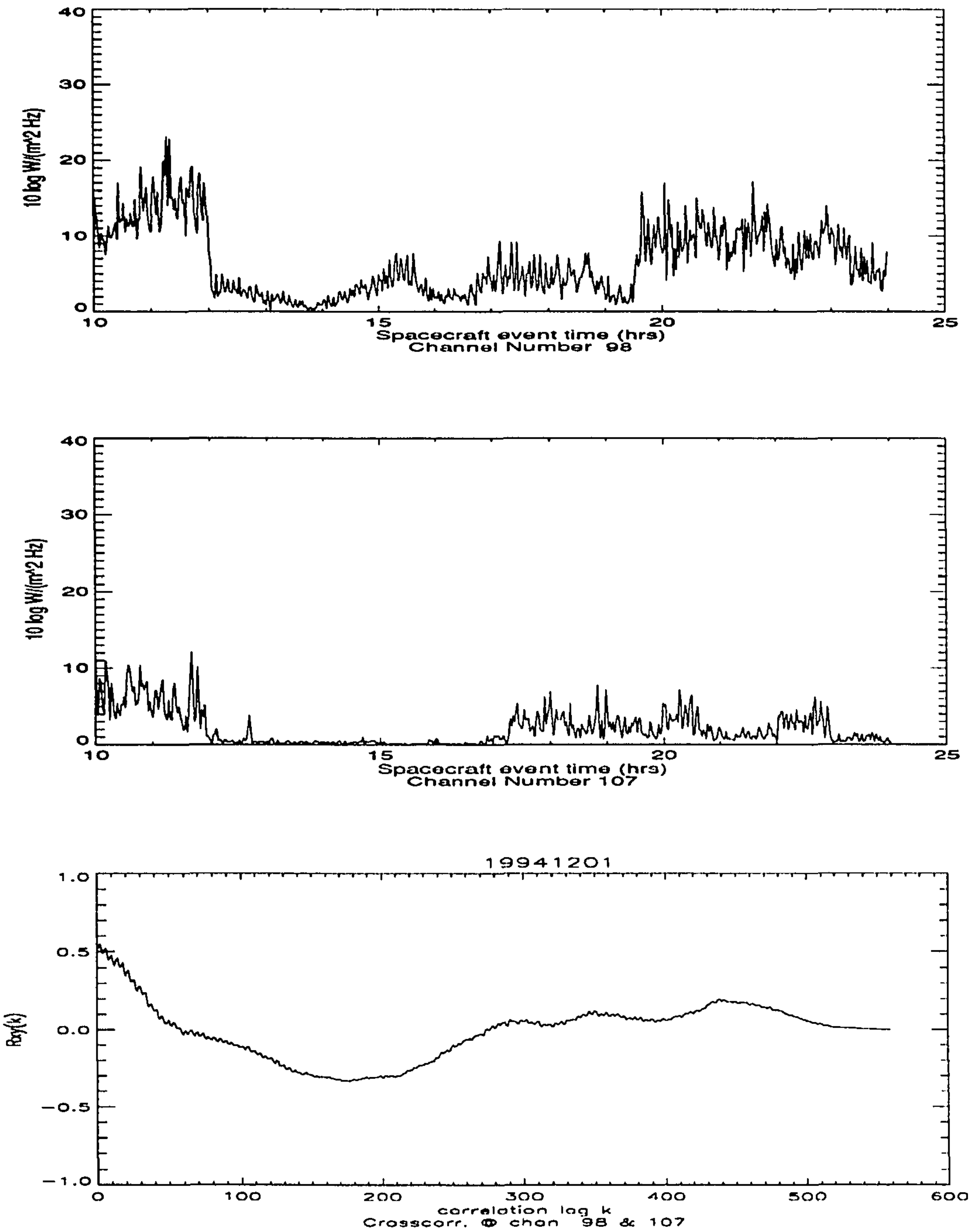

Figure 4-13 6.025 MHz (top) and 6.425 MHz (middle) time series and their cross correlation (bottom)

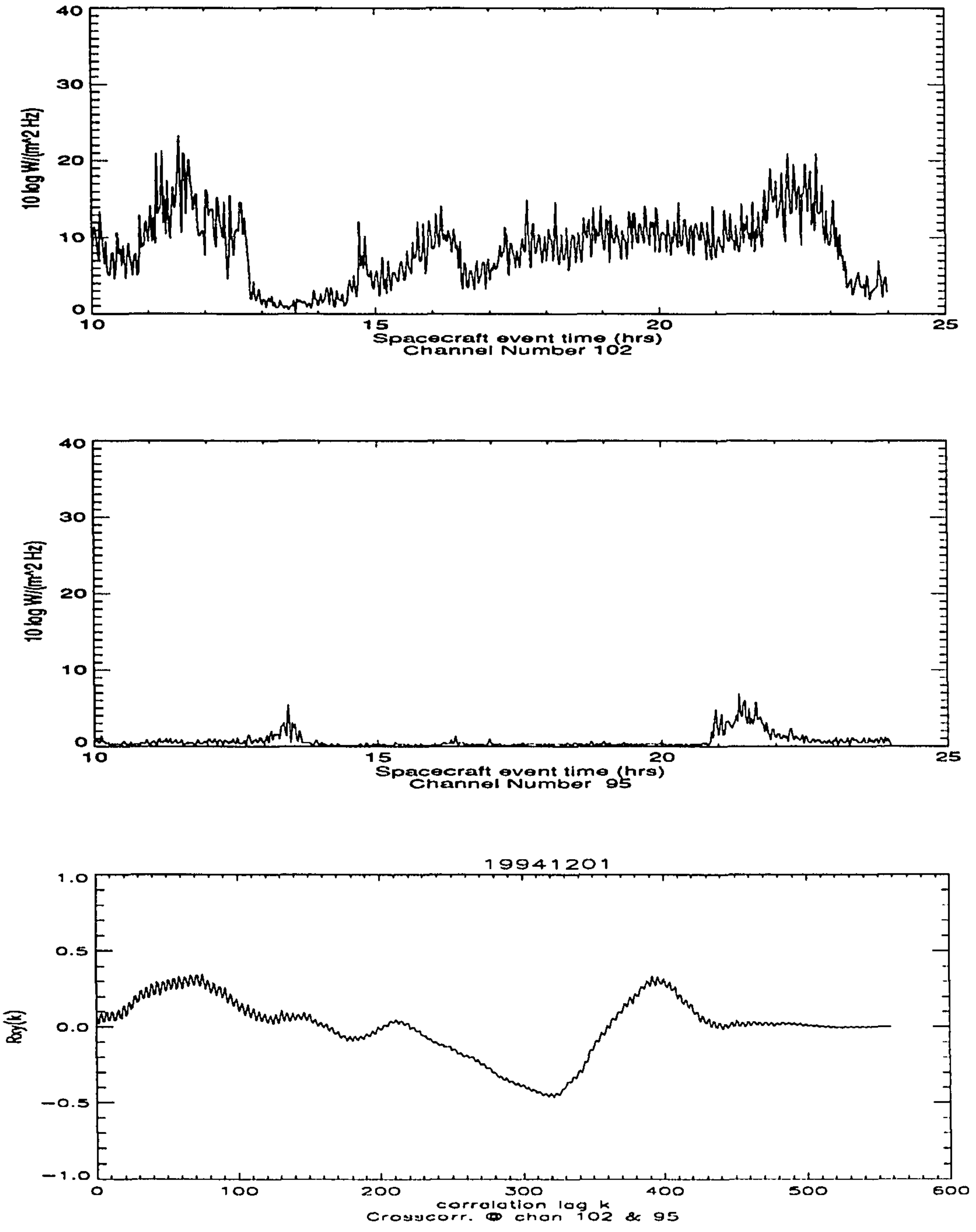

Figure 4-14 6.225 MHZ (top) and 5.825 MHz (middle) time series and their cross correlation

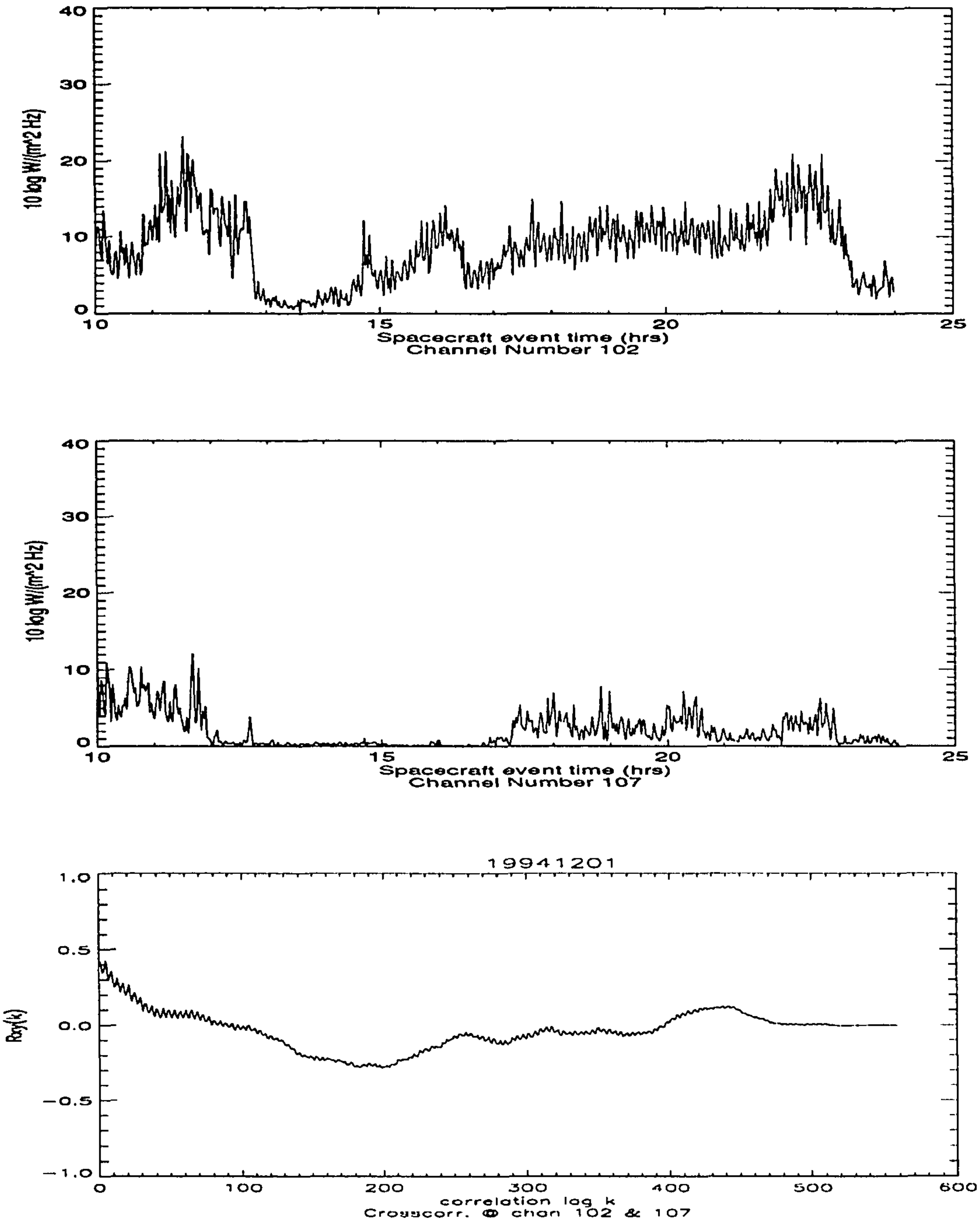

Figure 4-15 6.225 MHZ (top) and 6.425 MHz (middle) time series and their cross correlation the signals could truly be related. If channels corresponding to the intermodulation product frequencies did contain intermodulation distortion, one would expect stronger similarities at times when the terrestrial interference is present. As shown in Figures 4-12 through 4-15, this is not the case.

The data discussed in this chapter is representative of the set collected over three weeks by RAD2. In the latter part of the data set, type III solar bursts covering all 256 channels could be seen in the spectrograms. Although the duration of the data set is limited, a great deal of analysis on the nature of terrestrial interference could yet be done.

Unfortunately, the data itself is of little use in extracting details on the ionospheric irregularities which contribute to the amplitude fluctuations. There are several contributing factors, primarily involving the way the data itself is collected in RAD2. First, only the signal amplitude has been measured. Without phase fluctuation information, the data set is incomplete with respect to performing a scintillation study. On a related note, there is no way of knowing the phase reference for the received interference signals, since (in most cases) no single source has been identified. The resolution available (18 second time step and 50 kHz frequency) is too low to identify the types of the electron density irregularities causing the amplitude fluctuations. The local time of most measurements was between 9:00 to 10:00 AM, a period where the mid-latitude and equatorial ionosphere remain relatively calm.

4.4 Data Interpretation

One of the many tasks associated with the data analysis was to determine if the frequency channels proposed for an HF interferometer, 4.4 and 13.4 MHz, were at all contaminated by terrestrial interference. The process of determining this contamination involved searching through all channels adjacent to the desired frequencies, and noting any cases where interference appeared to be terrestrial in origin.

With the exception of data collected during a perigee pass, the channels encompassing the 4.3 - 4.5 MHz band appear to be empty of terrestrial interference. Signals that may be terrestrial in origin are not much stronger than the galactic background radiation level. Figure 4-16 illustrates a typical data set for 4.425 MHz. It is important to keep in mind that the daytime ionosphere helped shield the spacecraft from transmissions at frequencies lower than about 6 MHz. This effect would be even more marked during periods of higher sunspot number.

Unfortunately, even though the frequencies 13.36 -13.41 MHz are assigned strictly for use in radio astronomy (**Tables of Frequency Allocations and Other Extracts From: Manual of Regulations and Procedures for Federal Radio Frequency Management,** NTIA, September, 1989 edition) there are many days where it appears that terrestrial signal levels may be high enough to interfere with high sensitivity interferometry. The worst cases were observed while the spacecraft was in view of Eastern Europe, the former Soviet Union, the Indian subcontinent, and China (hours 00 to 1000 UT). Figure 4-16 illustrates a typical noisy channel (at 13.375 MHz, within the protected 13.36 to 13.41 MHz allocation). This time series was extracted from the December 3, 1994, data set. These measurements indicate that the allocated 13.4 MHz channel could not be reliably used by an orbiting interferometer even when the spacecraft is on the sunlit side of the Earth.

An additional analysis performed with the data was to determine if other channels were suitable for use by an orbiting interferometer. A number were identified, on the basis of the RAD2 findings, that appeared sufficiently "quiet". These are listed in Table 4-3, and corresponding time series are shown in Figures 4-18 through 4-22.

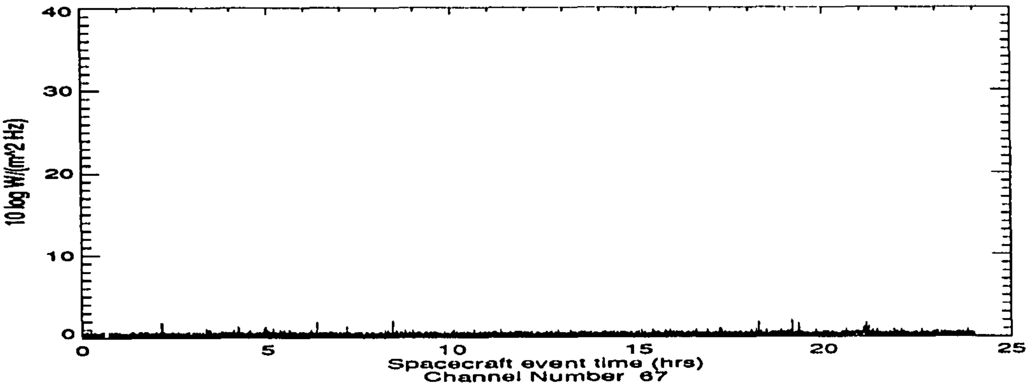

Figure 4-16 4.425 MHz data extracted for December 3, 1994

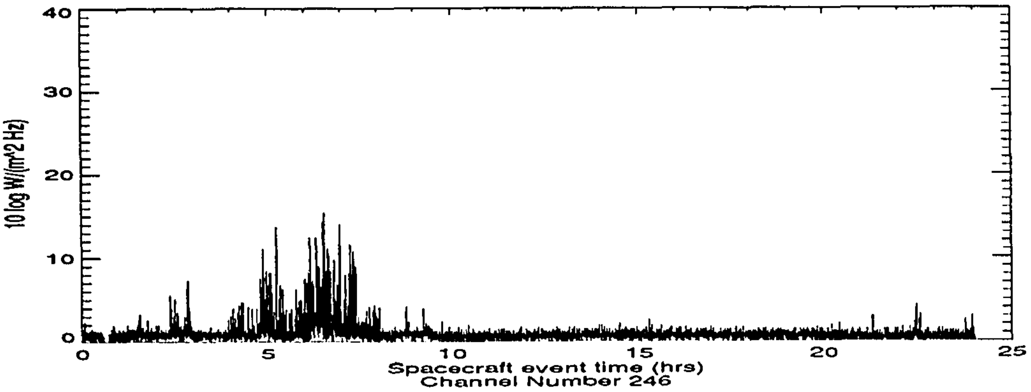

Figure 4-17 Terrestrial interference within the protected 13.4 radio astronomy band

Table 4-3 Alternate observing frequencies for an orbiting interferometer

Frequency (MHz)	Interference level (dB)[a]	Potential "hot spots"[b]
1.275	< 0.5/1.5	none
2.875	< 0.5/1.5	none
3.125	< 0.5/1.5	none
8.225	< 1.0/4.0	India/Asia
11.375	< 1.0/6.0	Eastern Europe

a. Interference levels are specified with respect to the galactic background radiation level. Number format is typical/worst case

b. "Hot spots" are areas that can be clearly discerned as having higher than usual interference.

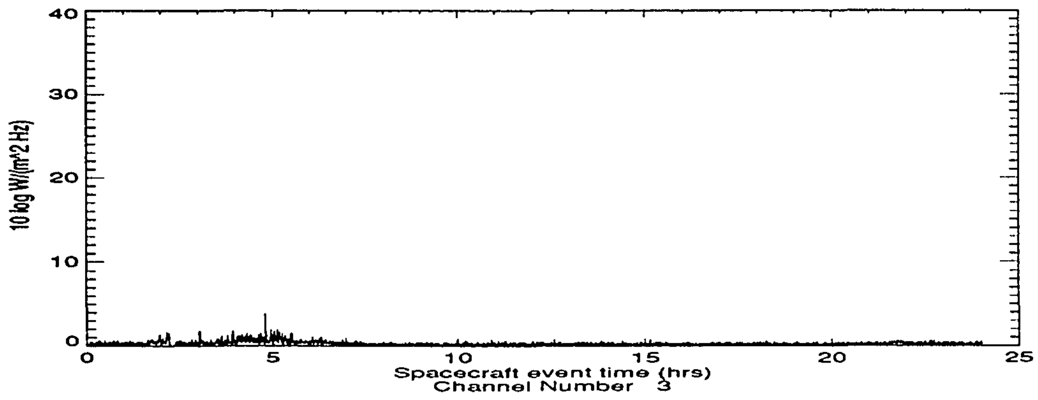

Figure 4-18 1.275 MHz channel behavior for November 17, 1994.

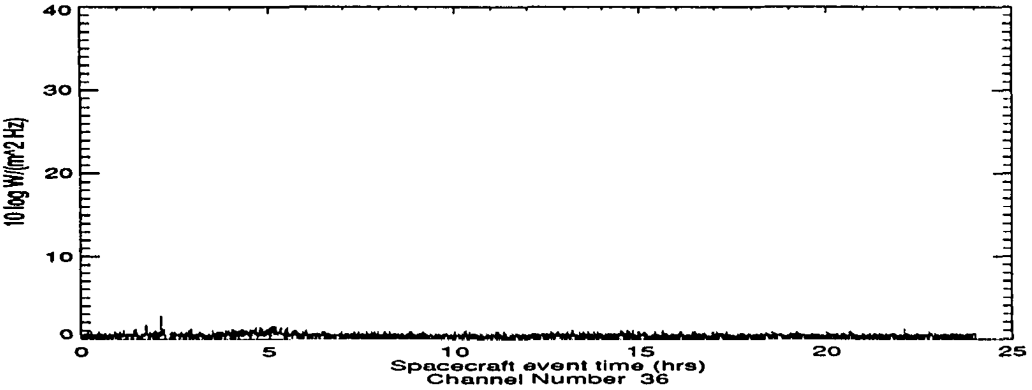

Figure 4-19 2.875 MHz channel behavior for November 17, 1994.

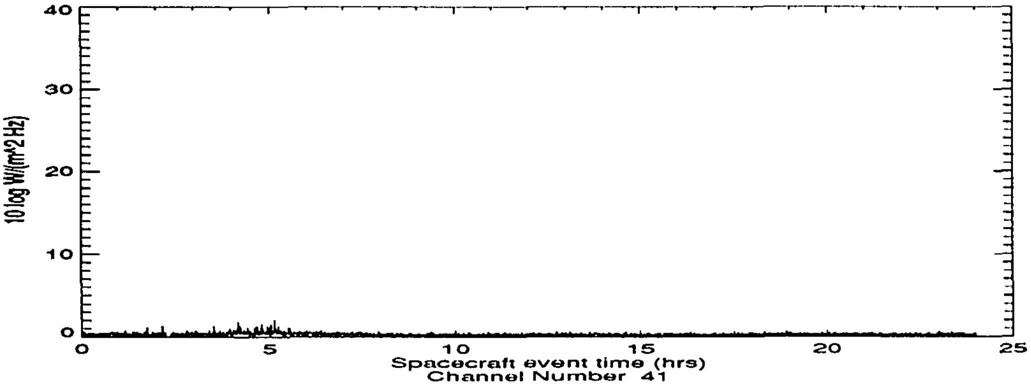

Figure 4-20 3.125 MHz channel behavior for November 17, 1994.

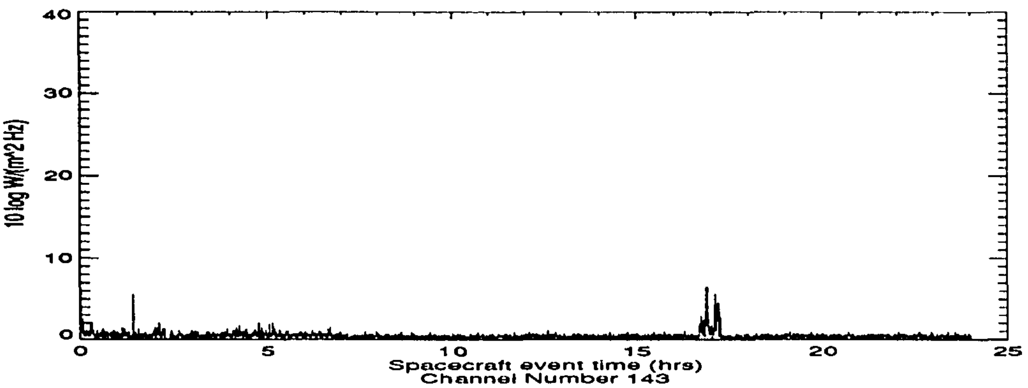

Figure 4-21 8.225 MHz channel behavior for November 17, 1994.

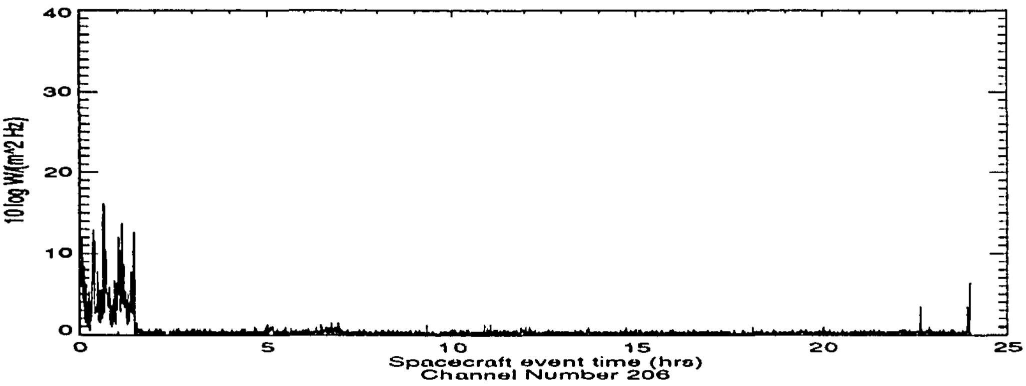

Figure 4-22 11.375 MHz channel behavior for November 17, 1994.

The 1.275 MHz frequency is close to the medium wave broadcast allocations of 1.27 and 1.278 MHz. The majority of medium wave broadcasters are low power, e.g. 10 kW or less. A few notable exceptions exist (almost exclusively in Europe, Eastern Europe, and the states of the former Soviet Union) where the broadcasters have the capability to transmit up to 500 kW. The 2.875 and 3.125 MHz channels also appear promising, since the few broadcasters licensed to operate near those frequencies use low power transmitters. For the 8.225 MHz channel, there are no broadcast allocations within 100 kHz of the channel, although it does appear to be used in Figure 4-21. One broadcaster is currently using the 11.375 MHz channel, thus limiting the interference potential to those areas within the station's intended service.

This is still a preliminary analysis of potential alternate observation channels. The analysis performed on the WIND data must be corroborated with additional ground- and space-based measurements. This information could be combined into a database so that a better allocation of observing frequencies may be made. The large differences in orbit configuration complicate extending the WIND results to channel availability for an interferometer in high Earth orbit. Terrestrial interference may actually exist in the recommended channels, yet the additional free space attenuation from 40,000 km to 125,000 km is enough to drop the signal level below the RAD2 sensitivity.

Another interesting observation is that no radar signals have been clearly identified in the data sets. Within the various time series analyzed, there are cases where spikes 10 to 20 dB above the galactic background appear. Identification of these spikes is difficult, since they appear randomly. Discussions with L. J. Nickisch of the Mission Research Corporation, S. J. Franke at the University of Illinois, and Chris Meek of the University of Saskatoon have raised the issue of whether radar pulses could be detected with the RAD2 receiver. The upper atmosphere radars operated by the University of Illinois and the University of Saskatoon usually transmit 25 to 50 kW (peak) at night at frequencies within 2.0 - 2.7 MHz (S. J. Franke, personal communication, 1995; C. Meek, personal communication, 1995). Since WIND only views a daylit Earth (with the exception of the perigee passes, which occur at local midnight), these radars could not be the source of the randomly occurring spikes. Over-the-horizon (OTH) radars would be many times more powerful than the atmospheric research radars discussed here. However, many OTH radars were used for military projects that are no longer funded (T. J. Fitzgerald, personal communication, 1994), so the potential for interference from these radars is much less than in the past.

It is also useful to compare the AMPTE/IRM observations (for the few frequencies that overlap) with the WIND results; the AMPTE/IRM time series data is illustrated in Figure 3-5. Much of the terrestrial interference detected by the receiver onboard AMPTE occurred in western Europe (LaBelle, et al., 1989). This is consistent with the fact that the majority of the HF spectrum users are located in Europe. However, there is a very important difference between the AMPTE and WIND interference measurements in that AMPTE data was collected near 0600 hours local time, which is before sunrise in the winter season, when the ionospheric electron density is most tenuous. WIND is in view of western Europe from 0800 to 1100 hours UT, at around 9:12 AM local time. Over the three hour period that WIND views Europe, no interference such as that detected by AMPTE was found. The entire data set has produced very consistent results in this comparison.

According to the latest ephemeris tables, the WIND spacecraft will be approaching the Earth sometime around August, 1995. Three highly elliptical orbits, similar to the orbits used in November, 1994, are planned. During this time, the instrument will scan its entire 256 channels again to collect additional information on terrestrial interference. As illustrated in Figures 2-2, 2-3, and 2-4, the Winter season peak plasma frequency is much lower than the Summer peak plasma frequency. With the large variation in electron density distribution between Summer and Fall seasons, the spectra collected during the August passes should be sufficiently different from the November, 1994 passes. Interesting conclusions may be drawn from a thorough comparison of data taken from the two distinct times of year.

CHAPTER 5

SOURCE AND PROPAGATION MODELING

5.1 Overview of Interference Research

There have been a number of papers published on the spectrum occupancy problem in HF (Gott, et al., 1994; Gibson and Arnett, 1994; Vincent and Lott, 1994; Lott, et al., 1994; Goutelard and Caratori, 1991; Laycock, et al., 1988; Perry and Abraham, 1988; Dutta and Gott, 1982). Most of the research has originated in the UK or Europe, where HF spectrum usage is significantly greater.

The interference in HF communication channels can often be characterized by the measurement of congestion ($Q \in \{0,1\}$), which is the probability of finding interference exceeding a specified threshold within a particular bandwidth (Moulsley, 1985). In many measurements, the specified bandwidth is as low as 100 Hz (Dutta and Gott, 1982; Moulsley, 1985) but 1 kHz is typically used (Gott, et al.,1994; Laycock, et al., 1988). For wideband spread spectrum HF communications, the interference from a number of emitters within the band can dominate atmospheric and other noise sources (Perry and Abraham, 1988). Most of the models derived from measurements focus on short-term forecasting of channel "clearness" (the complement of congestion, i.e., 1-Q). These models are functions of frequency, time, bandwidth, threshold level, type of user allocation, and geographical location (Gott, et al., 1994). The most recent model developed by Gott, et al. (1994), has parameters for the 95 separate user allocations in the HF spectrum. The congestion Q is defined as (Laycock, et al., 1988)

$$Q_k = \frac{e^{y_k}}{1+e^{y_k}} \in \{0...1\} \qquad (5\text{-}1).$$

The values y_k are fitted from channel occupancy measurements made in the UK over a 185 week period; the y_k given as

$$\begin{aligned} &A_k + B \,|\text{threshold value (dBm)}| + (C_0 + C_1 \bullet f_k) \bullet (SN) \\ &\quad + D \cos(2\pi \text{ week}/52) \bullet (SN) \\ &\quad + (E_0 + E_1 \bullet f_k) \cos(2\pi \text{ week}/52) + F \bullet f_k \cos(4\pi \text{ week}/52) \end{aligned} \qquad (5\text{-}2)$$

where A_k has 95 values associated with the 95 user channel allocations; the B, $C_{0,1}$, D, $E_{0,1}$, and F coefficients were derived by fitting the model to the measured data; f_k is the center frequency (in kHz) of each channel allocation; the parameter week takes values from 1 to 52, starting with the first week in January; and the parameter SN is the sunspot number for the week when congestion measurements were made. Ninety-five percent of the congestion values predicted by the model are within ±0.1 of the measured Q_k (Gott, et al., 1994). A slightly different set of coefficients for the model index function y_k was developed when measurements from the UK were combined with Swedish measurements; the new coefficients fitted to the combined data set differ from the original by about 10% (Gott, et al., 1994). Current measurement campaigns are extending the model occupancy research to include time of day dependency and inclusion of more measurement sites (Gott, et al., 1994). Figure 5-1 illustrates the congestion measured by Dutta and Gott (1982) for day and night. The congestion at the upper end of the HF band is low at night because the ionosphere can not support those propagation modes at the higher frequencies.

Numerous measurement campaigns conducted to characterize the terrestrial interference environment have indicated that international broadcasters only constitute a portion of the interference in a typical ground-based HF communication channel. Data collected by Vincent and Lott (1994) provide evidence that industrial, scientific, and medical (ISM) devices transmitting outside of their designated bands are a source of interference to users in authorized allocations. This out-of-band ISM interference has been detected across the entire HF spectrum, though international agreements limit the ISM channels to 6.78 MHz ± 15 kHz, 13.56 MHz ± 7 kHz, and 27.12 MHz ± 163 kHz. Measurements taken by Vincent and Lott in central Europe have shown ISM emissions are present in unauthorized channels at levels greater than 30 dB above the HF receiver's noise floor (the detected signal strengths were on the order of -100 to -90 dBm). Other interference signals were captured by the authors at various locations across the world, although their research did not extend to the development of a statistical model of the ISM interference characteristics.

The interference can be sporadic or periodic -- the sporadic emissions last on the order of tens of seconds, while the periodic signals detected repeat every three seconds (Vincent and Lott, 1994). While this may be considered very short-lived with respect to the integration time of an orbiting interferometer, this type of interference is the source of intermittent errors in HF communications. Signals have also been detected that appear to originate in Asia, with a time-frequency behavior that is characteristic of equipment used on an assembly line or automated manufacturing process. The interference levels varied with the diurnal variations of the ionosphere, and were not present during ionospheric storms. This has led Vincent and Lott to conclude that the sources were all beyond line of sight. Such interference is possible because skywave propagation can be very low loss under certain conditions. Measurements by Ward and Golley (1991) of the atmospheric noise (not interference) at HF also support this conclusion. Measurements of the atmospheric background noise at the Jindalee, Australia OTH radar site have found that increased ionization levels shifts the geographical regions from which noise (or interference) can propagate and also leads to increased absorption of the signal.

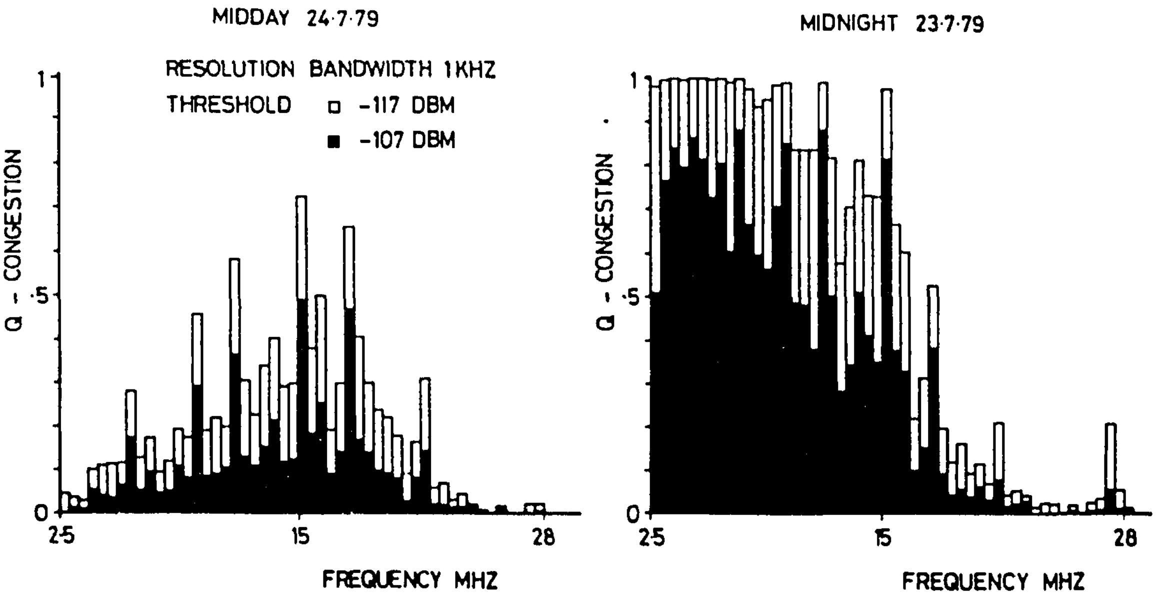

Figure 5-1 Spectral congestion in the HF band (from Dutta and Gott, 1982)

Most of the HF interference research has been concerned with the modeling of congestion. Simulations of interference signals have been less common. The research that has been conducted on interference simulation has primarily supported by military interest in experimental wideband HF (WBHF -- bandwidths ≈ 1 MHz) communications (Lemmon, 1991). Based on measurements taken using a WBHF communication link between

Homestead, FL, and Bedford, MA, Lemmon has found that the noise/interference is a narrowband process having a well-defined envelope and phase. His model is statistical in nature, the components of noise/interference have probability distribution functions describing various statistical characteristics. Lemmon has also created a physical model exhibiting the same characteristics. The Lemmon model of noise/interference has three components (Lemmon, 1991)

1. white Gaussian noise;
2. narrowband interferers (modeled as sine waves);
3. impulsive noise (modeled as filtered delta functions).

Within a wideband HF channel, contributions to the total noise/interference could come from many independent sources, so a Gaussian component would be present (by the central limit theorem). There are also a number of distinct, strong, narrowband interference sources that are dominant (and no longer included in the central limit theorem). The last component of the model accounts for the impulsive characteristics of atmospheric noise.

From the experimental channel measurements, Lemmon concluded that the frequency and phase for narrowband interferers are uniformly distributed. The signal amplitudes follow a probability distribution developed by Hall (1966). The narrowband interferers can be considered impulsive in the frequency domain, so the Hall probability distributions can be applied to model these amplitudes as well. Lemmon's measurements indicated that the impulsive noise tended to be separated by approximately 500 μseconds, which also implies a man-made origin. A detailed examination of the Hall probability models and their applications to wideband HF noise can be found in Lemmon (1989), which also presents earlier results of HF noise simulations. From Lemmon (1991), the time dependence of the simulated noise/interference signals are described using the signals' in-phase and quadrature (I and Q) components (this Q, for quadrature, should not be confused with the congestion probability Q):

$$I(t) = G_I(t) + \sum_{k=1}^{40} A_k \cos(\Delta\omega_k t + \varphi_k) + \sum_{j=1}^{50} B_j \frac{\sin 2\pi B(t-t_j)}{t-t_j} \cos\omega_0 t_j \tag{5-3}$$

$$Q(t) = G_Q(t) - \sum_{k=1}^{40} A_k \cos(\Delta\omega_k t + \varphi_k) + \sum_{j=1}^{50} B_j \frac{\sin 2\pi B(t-t_j)}{t-t_j} \sin\omega_0 t_j \tag{5-4}$$

where G_I and G_Q are independent, identically distributed Gaussian noise processes; $\Delta\omega k$ is uniformly distributed between ± 400 kHz, representing the distribution of random narrowband interferers within the receiver's bandwidth of 800 kHz; B is the baseband bandwidth used in the simulation (400 kHz); ω_0 is the carrier frequency, kept at 23.862 MHz for this simulation; and φ_k are the phases (uniformly distributed between 0 and 2π). The amplitudes A_k and B_j have probability density functions based on the Hall model:

$$p(s) = \frac{(\theta-1)\gamma^{\theta-1}s}{\left(s^2+\theta^2\right)^{(\theta+1)/2}} \tag{5-5}$$

where s is the random signal voltage and θ and γ are parameters describing the amplitude of the distribution. All narrowband interferers (A_k) kept the same values of θ and γ; likewise for the θ and γ parameters for the impulsive interferers (B_j). The simulated signal compared well with the measured data. The cumulative distribution functions of the power envelope of the narrowband interferers generated by the simulations also resembled the results published by Perry and Abraham (1988) and Moulsley (1985). Despite the encouraging results, the

Lemmon model is based on a limited data set. Lemmon (1991) identified two areas of further work: additional data collection from different sites and times of year; and detailed analysis of the nonstationarity of the HF channel. More recent developments on this interference modeling have not been published to date.

5.2 A New Terrestrial Interference Model

An HF interferometer in space will have different interference requirements than a terrestrial HF communication system. It is evident from the WIND observations that the primary terrestrial interference sources detectable in space are international broadcasters, unlike the intererence detected on Earth. A new terrestrial interference model is presented here, derived in part from the authorized broadcast frequency allocations. As a first generation model, only signals from the broadcast frequencies were included. Information on these sources is most readily available. The interference from ISM sources, while possibly significant, will not be modeled due to insufficient data on the statistical behavior of the signal amplitudes. ISM interference may not cause problems for an Earth-orbiting interferometer for two reasons:

1) the very short time duration of the ISM interference, while causing serious data transmission error rates on the ground, is insignificant with respect to the integration time of an orbiting interferometer ($\approx 10^6$ seconds);

2) the signal attenuation due to transionospheric propagation is much greater than the attenuation in skywave propagation; thus signal levels may be at or below galactic background emission levels at the Earth-orbiting receiver.

A new model is presented here that describes the HF interference as sums of narrowband interferers distributed across the HF channels, modified by propagation through the ionosphere. The total signal power at the Earth-orbiting receiver can be found using a modified Friis transmission formula, which includes a ionospheric transfer function term:

$$P_r = P_t \frac{G_t G_r \lambda^2}{(4\pi R)^2} T(f, SN, \theta^i, \phi^i, \Theta, \Phi) \tag{5-6}$$

where P_r is the received power, P_t is the transmitted power, G_t and G_r are the gains of the transmitting and receiving antennas, respectively, λ is the wavelength, and R is the range. The ionospheric transfer function T depends on the frequency, solar conditions (SN is sunspot number), ray launch angles (elevation θ^i and azimuth ϕ^i), and geographical coordinates (latitude Θ and longitude Φ). The motivation for using a transfer function for transionospheric propagation is discussed in Section 5.2.2, including a methodology for transfer function development using three-dimensional raytracing. Equation (5-6) represents the fundamental relationship between the total transmitted interference power and the power available at the Earth-orbiting interferometer. For simplicity, G_t and G_r are assumed to be uniform with frequency, elevation, and azimuth in the transfer function development. The actual receive antenna gain is later reintroduced when comparing the simulated interference spectrum with data from WIND.

For the transionospheric propagation of impulsive signals, the dispersive character of the ionosphere becomes a necessary part of the analysis. If a transmitter produces an impulse of U_0 joules/Hz, the total energy per steradian per Hertz radiated toward the receiver is

$$U_t = {}^{U_0 G_t}\!/_{4\pi} \tag{5-7}$$

where G_t is the gain of the transmitting antenna within the receiver noise bandwidth B_r. The total received power at a frequency f is (R. Massey, personal communication, 1994):

$$P_r = \left(\frac{G_t U_o}{4\pi} B_r\right)\left(\frac{G_r \lambda^2}{4\pi R^2}\right) T(f) \frac{1}{\sqrt{\tau_i^2 + \tau_f^2}} \tag{5-8}$$

The first quantity in parentheses is the energy per steradian transmitted within the receiver's bandwidth; the second quantity in parentheses describes the effective collecting area of the receiving antenna in steradians. T(f) describes the ionospheric contribution to the absorption of the signal; this is the same T used in equation (5-6), with the other function dependencies truncated for convenience. The last fraction in the received power expression accounts for the finite receiver bandwidth ($\tau_f = 1/B_r\sqrt{\pi}$ for a filter with a Gaussian frequency response) and ionospheric dispersion ($\tau_i = \sqrt{|\partial t_g/\partial\omega|}$, t_g is the group delay introduced by the ionosphere) (R. Massey, personal communication, 1994). When ionospheric effects dominate (i.e., $\tau_i >> \tau_f$), the received power can be rewritten as

$$P_r = P'\left(\frac{G_t G_r \lambda^2}{4\pi R^2}\right) D T(f) \tag{5-9}$$

where $P' = \pi U_o B_r^2$ and D can be called a dispersion "loss" term, $D \equiv {}^{1}\!/_{\pi B_r \tau_i}$. These effects are discussed in some detail in Massey (1993).

For the case of interference from broadcast transmissions, it could be safely assumed that the signals are not impulsive (i.e., their duration is on the order of tens of <u>minutes</u> rather than tens of milliseconds), so the dispersion loss term can be omitted.

5.2.1 Interference signal model

This section will describe a new model of the total power transmitted by the terrestrial interference sources, the P_t of equation (5-6). The total power transmitted through the ionosphere by the interference sources is a function of geographical location and frequency of the transmitters. The geographical dependence of HF channel usage is evident from the WIND spectrograms (Figures 4-3 and 4-4). A basic question to be answered in this research is how to model the spectrum of the total interference power at any given instant in time. The interference modeling approach developed here begins by grouping the sources into 5 broad geographical classes: Americas; Western Europe and Africa; Eastern Europe, Russia and neighboring states, India and neighboring states; Asia, Australia, and Indonesia; and the Pacific Islands. The frequency range of the model is 2.7 MHz to 13.8 MHz, in 100 kHz steps. There are a great many more HF channels within these broad frequency steps, but extremely fine detail is not necessary for a first generation model. Since the proposed 3-dB bandwidth of the LFSA receiver is 50 kHz, not much additional resolution would be required for a second-generation model. The upper frequency is limited to 13.8 MHz because of the lack of space-based interference measurements beyond that frequency. It should also be noted that there are only four broadcasters operating near the 25.55 - 25.67 MHz radio astronomy allocation. All of these are located in regions having high HF interference at the other observing frequencies of interest, so these regions would be have to be avoided anyway. The individual channels also differ greatly in type of broadcast and overall occupancy. The overall number of users for each channel is set to exact values at three occupancy levels: low (5 users), medium (22 users), and high (45 users). It should be noted that this is merely an approximation, since there is no way of knowing the exact number of users occupying a particular channel at any point in time. To get around this difficulty, the occupancy values have been estimated from the number of authorized broadcast users within each 100 kHz frequency bin. These general characteristics have been extracted from the 1994 edition of the *World Radio TV Handbook.* Many channels at frequencies above 6 MHz also have high power transmitters (200 kW and higher). The signals can be a combination of the three occupancy levels and two transmit power levels (low and high). The available information on the broadcast users indicates that any of the six combinations are possible within the channels modeled here.

The total transmitted interference power at each ith frequency step is some combination of the individual transmitter powers. The total interference power will vary greatly depending on whether the interference from individual transmitters combine coherently or incoherently or somewhere in between. Let us consider a general case, where the total interference can be represented as a random phasor sum:

$$S = Re^{j\theta} = \sum_{k=1}^{n} A_k e^{j\varphi_k} \tag{5-10}$$

If the phase φ_k is uniformly distributed between 0 and 2π, each phasor is independent from the others, and A_k is uncorrelated with φ_k, then $\langle R^2 \rangle = \langle SS^* \rangle$ (where $\langle \ldots \rangle$ corresponds to the expectation operator). $\langle SS^* \rangle$ can be expanded as (Beckmann, 1967)

$$\begin{aligned} &\left\langle \sum_{m=1}^{n} A_m \sum_{k=1}^{n} A_k e^{j(\varphi_m - \varphi_k)} \right\rangle \\ &= \sum_{m=1}^{n} \sum_{n=1}^{n} \langle A_m A_k \rangle \left\langle e^{j(\varphi_m - \varphi_k)} \right\rangle \end{aligned} \tag{5-11}$$

The summation is 0 for m≠k and 1 for m=k, reducing equation (5-11) to $\langle R^2 \rangle = \sum_k \left\langle A_k^2 \right\rangle$, which is simply the variance of the random phasor sum (assuming a zero mean random variable). If the quantity n is small, the Central Limit Theorem can not be satisfied (Beckmann, 1967). Splitting the random phasor sum into its real and imaginary components gives,

$$X = \sum_{k=1}^{n} A_k \cos \varphi_k$$

$$Y = \sum_{k=1}^{n} A_k \sin \varphi_k \qquad (5\text{-}12)$$

we know that $\langle X \rangle = \langle Y \rangle = 0$. With A_k and φ_k uncorrelated (and φ_k still uniformly distributed between 0 and 2π), $\langle X^2 \rangle$ and $\langle Y^2 \rangle$ can be expressed as

$$\sum_{k=1}^{n} \left\langle A_k^2 \right\rangle \left\langle \cos^2 \varphi_k \right\rangle = \frac{1}{2} \left\langle R^2 \right\rangle \qquad (5\text{-}13)$$

Individual realizations of the random variables X and Y are denoted by their lower case equivalents, x and y. From Beckmann (1967), we find the expression for the probability density of the realization, r, of the magnitude of the random phasor sum, R, to be

$$p(r) = \frac{2re^{-r^2/\alpha}}{\alpha} \left[1 + \frac{3}{8n} \left(\frac{\left\langle R^4 \right\rangle}{\left\langle R^2 \right\rangle^2} - 2 \right) \left(\frac{r^4}{2\alpha^2} - \frac{2r^2}{\alpha} + 1 \right) + \ldots \right] \qquad (5\text{-}14)$$

where $\alpha \equiv n\langle R^2\rangle$. As n → ∞, the distribution tends to a Rayleigh distribution. The terms in the square bracket in equation (5-14) are the correction for small n.

Using the assumption that the signals combine in a partially coherent manner, we must think in terms of the equivalent E fields summing up partly in phase. The phases are uniformly distributed between 0 and 2π, as in the discussion above. The amplitudes and phases of the individual signals are uncorrelated. If the individual signals were completely incoherent, then the resulting interference signal would be the variance of the random phasor sum. For the completely coherent case, the signals are all in phase, so the interference signal would be

$RR^* = R^2 = \sum_{k=1}^{n} A_k A_k^* = \sum_{k=1}^{n} A_k^2$, since both the individual amplitudes and the phasor sum would be strictly real. In this case, the variance of the total interference would become

$\left\langle R^2 \right\rangle = \left\langle \sum_{k=1}^{n} A_k^2 \right\rangle$. The total interference power for incoherent and coherent interference will vary according to the total number of individual interferers (the 'n' used in the summation). Returning again to the partially coherent case, the resulting equation for the total interference signal is:

$$E_i = \sum_{k=1}^{n} A_{k,i} \exp\{j\theta_k\} \qquad (5\text{-}15)$$

where E_i is the total field at the ith frequency; and n = 5, 22, or 45, corresponding to the low, medium, or high occupancy levels; $A_{k,i}$ is the random field of the kth individual interferer at the ith frequency bin; and θ_k is the random phase of the kth interferer. The individual interference fields ($A_{k,i}$) have the following probability density function:

(low power equivalent)
$$p(A_{k,i}) = U\{1941 \ldots 4341\} \qquad (5\text{-}16)$$

(high power
equivalent)

$$p(A_{k,i}) = U\{6140\ldots13729\} \qquad (5\text{-}17),$$

such that each individual interference value is uniformly distributed between the minimum and maximum values within the brackets. These signals are assumed to be well-represented by a uniformly distributed function within the equivalent low or high transmitter power ranges -- no statistical studies exist to indicate that these amplitudes follow a Hall probability model, such as the amplitudes modeled by Lemmon (1991). Another argument against using the Hall probability model is that the interference signals measured by Lemmon had already propagated through the ionospheric channel, so that ionospheric effects were superimposed upon the original interference behavior. The total interference flux density S_i is then simply

$$S_i = 20\log_{10}\left(\delta + Ex_i \cdot {|E_i|^2}\!\big/{Z_o}\right),\ \text{dB}\left[{W}\!\big/{m^2}\right] \qquad (5\text{-}18)$$

where δ is minimum (noise) signal, Ex_i is a binary function describing the existence (1) or absence (0) of a broadcaster in that frequency channel, and Zo is 377 Ω, the impedance of free space. With no signal present, S_i is at the minimum level of -77 dB (W/m^2) $\pm$ 3 dB (δ is nominally $2 \cdot 10^{-8}$ W/m^2). The nominal effective radiated power output for each of the low power transmitters varies from 1 kW to 50 kW; the output for each of the high power transmitters varies from 100 kW to 500 kW. This interference spectrum model is intended to reproduce some of the large-scale features of the worst case interference for an Earth-orbiting interferometric array. As such, variations in amplitude due to differences in antenna patterns, modulation formats, or broadcast schedules were not included in the model. This model essentially assumes that all interferers within each occupancy class are broadcasting simultaneously. This aspect also contrasts with the Lemmon model, which presents a time-dependent description of the interference detected by a HF receiver on the ground. From the point of view of an Earth-orbiting interferometer, short time scales (which are necessary for understanding the interference impacts on HF data transmissions) are not required to determine global channel "clearness" for interferometry.

The following methodology was used for creating the interference spectra:

1. Divide the spectrum into 100 kHz bins.
2. For the ith 100 kHz bin, determine whether any broadcasters use that frequency. Set Ex_i accordingly.
3. Create a K row × 2 column matrix, where K is the number of frequency bins under consideration. This matrix holds the occupancy and transmitter power information. If the ith bin is used by broadcasters, determine if the number of users is low, medium, or high; set the flag in the first column accordingly. Also determine whether the majority of the users are low or high power; set the flag in the second column to either low or high power accordingly.
4. Repeat the process for all of the frequency bins covering the band of interest.

Future refinements may add other types of interference sources to each frequency bin, modify the probability density functions for the transmitter powers (to include a time/schedule dependent behavior) or include antenna pattern effects. An alternate probability density function to consider for the individual interferer outputs is a bimodal distribution, using the previously described maxima and minima.

Sample spectra for the five different geographical regions modeled are shown in Figures 5-2 through 5-6. The flux densities from equation (5-18) are converted into power by assuming a 1 m^2 aperture. The spectra are plotted in terms of dBW versus frequency, so small scale fluctuations on this plot would correspond to larges excursions in power on a linear plot.

Given the dynamic range plotted in these figures, power fluctuations on the order of 10 to 20 dB are not clearly shown. In Chapter 6, the spectra produced by the new interference signal model will be modified by the ionospheric transfer function, then compared to spectra extracted from the WIND data set.

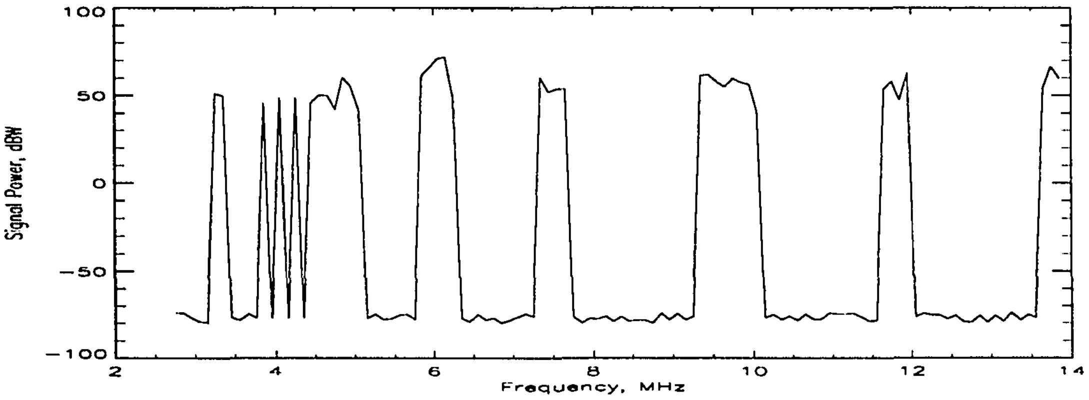

Figure 5-2 Simulated interference spectrum for North and South America

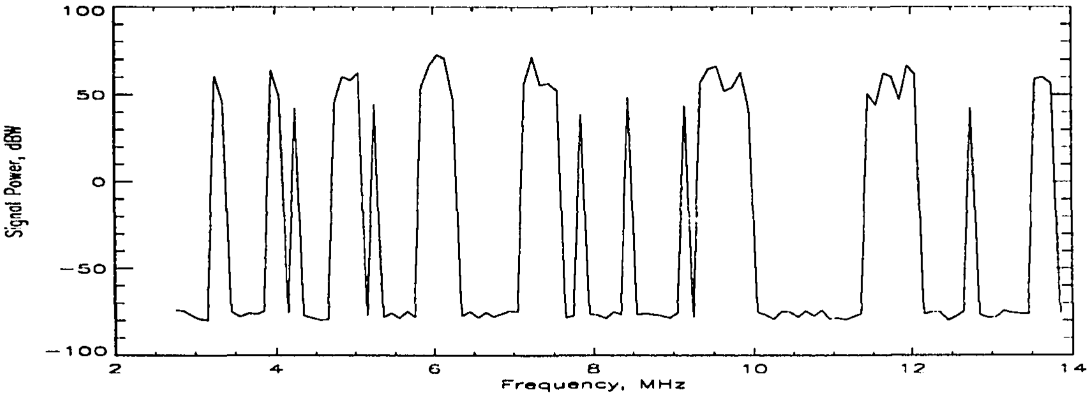

Figure 5-3 Simulated interference spectrum for Western Europe and Africa

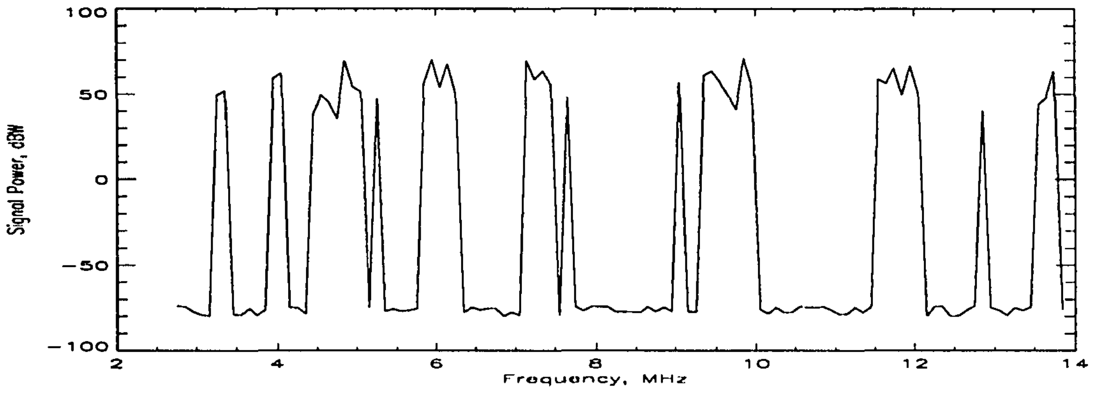

Figure 5-4 Simulated interference spectrum for Eastern Europe, Russia, and India

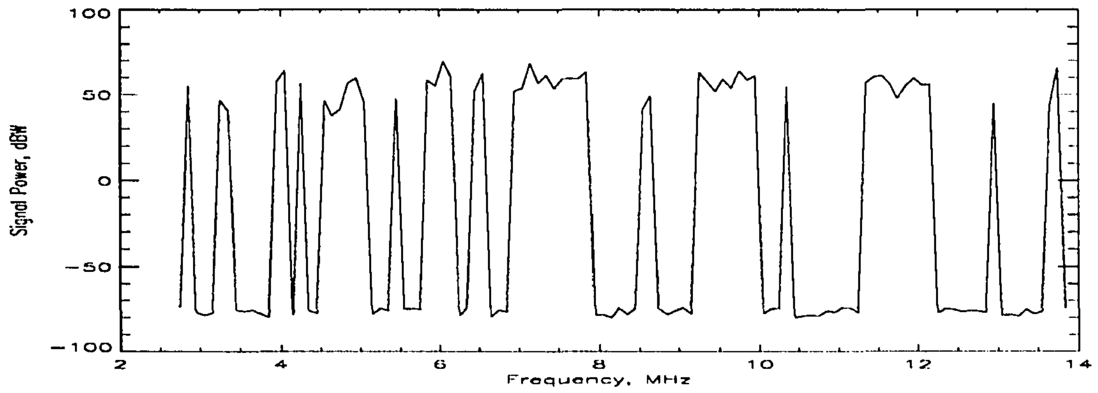

Figure 5-5 Simulated interference spectrum for Asia, Indonesia, and Australia

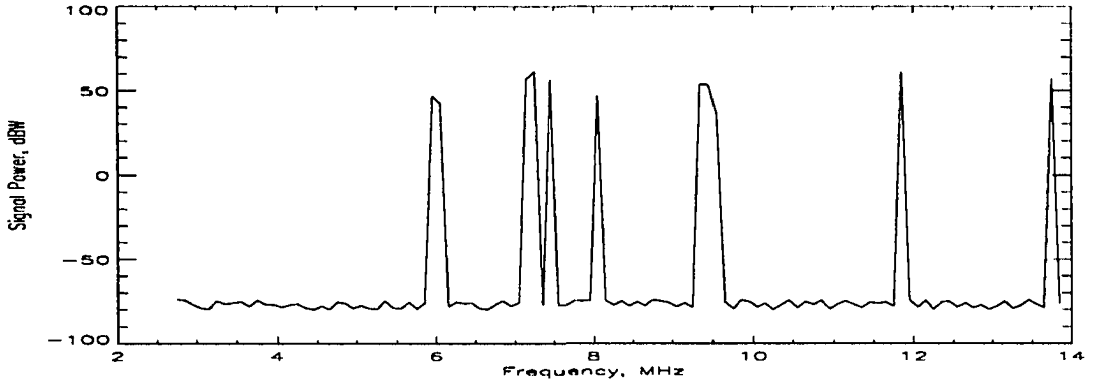

Figure 5-6 Simulated interference spectrum for the Pacific Islands (Guam)

In all the simulated spectra (Figures 5-2 through 5-6), there are gaps between the occupied channels. Some geographical regions clearly contain more of these "clear" bands than others. This indicates that for some regions, the HF spectrum is has a higher occupancy. The clear bands are outlined in Table 5-1.

The Pacific Ocean region contains the least number of interence sources, hence, it has the least occupied spectrum of the five regions studied. The few interference sources that do exist are primarily commercial broadcasters located on the island of Guam. This simulation is such that Europe, Africa, India, Russia, and Asia contain the most number of interferers, in accordance with the WIND interference measurements (Chapter 4) and spectrum occupancy measurements (Gibson and Arnett, 1994; Gott, et al., 1994; Lott, et al., 1994; Vincent and Lott, 1994; Goutelard and Caratori,1991; Ward and Golley, 1991; Laycock, et al.,1988; Mousley, 1985; Dutta and Gott, 1982; Wilkinson, 1982).

From the *Tables of Frequency Allocations*, the frequencies associated with the gaps in the spectrum are assigned to fixed and mobile communications services. Typically, these services use much lower transmitter powers than the broadcast services, so they may not be a source of interference for an Earth-orbiting interferometer. In the simulated spectra, these unoccupied areas only contain low level noise. The assumption that commercial broadcasters form the primary source of the HF interference in space will be tested in Chapter 6, when the simulated spectra are compared to spectra extracted from the WIND data set.

Table 5-1 "Clear" frequency bands: interference simulation

Geographical region	Clear frequency bands (MHz)
North/South America	5.0-5.7
	6.5-7.5
	8.0-9.2
	10.2-11.5
	12.0-13.5
Western Europe/Africa	6.3-7.2
	10.0-11.4
	12.0-12.5
Eastern Europe, Russia, India	6.2-7.0
	7.7-9.0
	10.0-11.5
	12.2-12.7
	11.0-11.5
Asia, Indonesia, Australia	8.0-8.5
	10.5-11.2
	12.2-12.7
Pacific islands (Guam)	2.8-6.0
	6.1-7.0
	8.1-9.1
	10.0-11.7
	12.0-13.7

5.2.2 Transionospheric transfer function

Interest in ground-to-satellite propagation of broadband signals has been the motivation for investigations into a theoretical transfer function for ionospheric radio propagation which incorporates dispersion, refraction, reflection absorption, and scattering effects. Full wave methods were considered for the numerical transfer function development, but were rejected as infeasible for the large-scale study required (see Appendix B for a discussion of the limitations of full wave methods with respect to the a large-scale interference simulation). The ionospheric transfer function (ITF) for midlatitude model ionospheres at VHF was developed at Los Alamos National Labs (Roussel-Dupré and Argo, 1992). For frequencies greater than 20 to 30 MHz, the transionospheric transfer function can ignore the effects of refractive bending (Roussel-Dupré, 1995). The analytically derived ITF was compared to an ITF derived from three-dimensional raytracing in model ionospheres (TRACKER). The benchmark cases studied by Roussel-Dupré and Argo were limited to unperturbed, spherically symmetric ionospheres. The two approaches were found to agree within five percent for moderate to high ray launch angles. The raytracing code tended to depart from the analytical resuls at very low ray launch angles (less than 10°) because of the difficulty in homing at these angles (Roussel-Dupré and Argo, 1992).

For frequencies below VHF, raytracing is the most efficient method for deriving ITFs, since three-dimensional raytracing can incorporate the propagation effects of departures from spherical symmetry. It is also the only method available to find ITFs for deterministically perturbed ionospheres. The deterministic ITF used in this research is derived from ray tracing through model ionospheres. Information from the rays that penetrate the ionosphere are collected and analyzed to produce a frequency and transmitter-receiver geometry dependent description of the ionospheric effects on the radio propagation. TRACKER (Argo, et al.,

1994) is used here to produce the raytracing-derived ITF for realistic model ionospheres under various conditions.

5.2.2.1 Ionospheric raytracing Raytracing is a method of simulation the propagation of waves in a medium whose refractive index varies continuously. Standard ray theory assumes that energy is conserved within a flux tube of rays; the energy density is inversely proportional to the cross-sectional area of the ray tube (Balanis, 1989). In regions known as caustics, the ray tube area approaches zero, and the energy density becomes infinite. Ray theory breaks down at caustics. Without higher order corrections, ray theory can only account for refraction from large-scale gradients in the background propagation medium (Argo, et al., 1994).

In an anisotropic medium (such as the Earth's ionosphere) the wave front and wave energy generally travel in different directions. If the medium is also inhomogeneous, the ray direction becomes a function of the medium variability as well. The subject of ray tracing in the ionosphere has been thoroughly researched over the last thirty years. Areas of recent development have involved more sophisticated algorithms, improved ionospheric models, or more functionality built into the ray tracing program.

The basis for most of the ionospheric raytracing methods currently in use is Hamilton's equations derived from a variational analysis applied to Fermat's principle (Roussel-Dupré and Argo, 1992; Haselgrove, 1963; Haselgrove, 1954). The Hamiltonian method, which requires continuous electron density models, avoids discontinuous ray paths. The original computer formulation of the Hamiltonian ionospheric raytracing equations was developed by Jones and Stephenson (1975); various versions of this original code are still in use today (M. Kaiser, personal communication, 1992).

By ignoring particle collisions, we effectively treat the ionosphere as a non-absorbing medium, with a real refractive index n. In this case, the ray path can be thought of as the locus of Fresnel zone centers between the ray origin and observation point, i.e., the path taken by the electromagnetic energy.

The Hamiltonian raytracing method involves numerically integrating the Hamiltonian equations for the ray position and wave vector, given the initial conditions for the ray (Argo, et al., 1994). Fermat's principle of least time is the starting point for the Haselgrove formulation of the Hamiltonian raytracing method (Kelso, 1964). A ray between two points is a curve such that the time of transmission is either maximum or minimum. Complete explanations of Haselgrove's method can be found in Kelso (1964) and Argo, et al. (1994). For the modern implementation of Haselgrove's method, the Hamiltonian function used depends on the ionospheric quantities as:

$$H = \mathrm{Re}\left\{\begin{array}{l} \left[(U-X)U^2 - Y^2U\right](ck)^4 + X\left(\vec{k}\cdot\vec{Y}\right)^2(ck)^4 + \\ \left[-2U(U-X)^2 - Y^2(2U-X)\right](ck\omega)^2 - X\left(\vec{k}\cdot\vec{Y}\right)^2(ck)^2 \\ +\left[(U-X)^2 - Y^2\right](U-X)\omega^4 \end{array}\right\} \tag{5-19}$$

where U, and X are defined in equation (2-5), Y is the normalized gyrofrequency defined in Chapter 2, c is the speed of light in free space, ω is the angular wave frequency, and k is the magnitude of the wave vector. In spherical coordinates, which are naturally suited to the geometry of raytracing over a spherical Earth, the differential equations to be solved are (Argo, et al., 1994):

$$\frac{dr}{d\tau}=\frac{\partial H}{\partial k_r},\quad \frac{d\theta}{d\tau}=\frac{1}{r}\frac{\partial H}{\partial k_\theta},\quad \frac{d\phi}{d\tau}=\frac{1}{r\sin\theta}\frac{\partial H}{\partial k_\phi} \tag{5-20}$$

$$\frac{dt}{d\tau}=-\frac{\partial H}{\partial \omega} \tag{5-21}$$

$$\frac{dk_r}{d\tau}=-\frac{\partial H}{\partial r}+k_\theta\frac{\partial\theta}{\partial\tau}+k_\phi\sin\theta\frac{\partial\phi}{\partial\tau} \tag{5-22a}$$

$$\frac{dk_\theta}{d\tau}=\frac{1}{r}\left(-\frac{\partial H}{\partial\theta}-k_\theta\frac{\partial r}{\partial\tau}+k_\phi r\cos\theta\frac{\partial\phi}{\partial\tau}\right) \tag{5-22b}$$

$$\frac{dk_\phi}{d\tau}=\frac{1}{r\sin\theta}\left(-\frac{\partial H}{\partial\phi}-k_\phi\sin\theta\frac{\partial r}{\partial\tau}-k_\phi r\cos\theta\frac{\partial\theta}{\partial\tau}\right) \tag{5-22c}$$

$$\frac{d\omega}{d\tau}=\frac{\partial H}{\partial t} \tag{5-23}$$

In equations (5-20) and (5-22), the quantities (r,θ,ϕ) are the Earth-centered spherical coordinates of a point on the ray path, (k_r,k_θ,k_φ) are the components of the wave vector $\bar{k}$, t is the propagation time of a wave packet, and τ is a variable that depends on the Hamiltonian. In this formulation, τ is chosen as $P' = ct$. Using P' in place of τ, the equations can be rewritten as

$$\frac{dr}{dP'}=-\frac{1}{c}\frac{\partial H/\partial k_r}{\partial H/\partial\omega},\quad \frac{d\theta}{dP'}=-\frac{1}{rc}\frac{\partial H/\partial k_\theta}{\partial H/\partial\omega},\quad \frac{d\phi}{dP'}=\frac{1}{rc\sin\theta}\frac{\partial H/\partial k_\phi}{\partial H/\partial\omega} \tag{5-24}$$

$$\frac{dk_r}{dP'}=\frac{\partial H/\partial r}{\partial H/\partial\omega}+k_\theta\frac{\partial\theta}{\partial P'}+k_\phi\sin\theta\frac{\partial\phi}{\partial P'} \tag{5-25a}$$

$$\frac{dk_\theta}{dP'} = \frac{1}{r}\left(\frac{1}{c}\frac{\partial H/\partial\theta}{\partial H/\partial\omega} - k_\theta\frac{\partial r}{\partial P'} + k_\phi r\cos\theta\frac{\partial\phi}{\partial P'}\right) \tag{5-25b}$$

$$\frac{dk_\phi}{dP'} = \frac{1}{r\sin\theta}\left(\frac{1}{c}\frac{\partial H/\partial\phi}{\partial H/\partial\omega} - k_\phi\sin\theta\frac{\partial r}{\partial P'} - k_\phi r\cos\theta\frac{\partial\theta}{\partial P'}\right) \tag{5-25c}$$

$$\frac{d(\Delta f)}{dP'} = -\frac{1}{2\pi}\frac{\partial H/\partial t}{\partial H/\partial\omega} \tag{5-26}.$$

The initial values for the ray at its starting point (r^i,θ^i,ϕ^i) and $(k^i{}_r,k^i{}_\theta,k^i{}_\varphi)$ are necessary in order to solve these six differential equations. Substituting the actual ionospheric expressions into the Hamiltonian function is a complicated process. The equations are worked out in detail in Argo, et al., (1994) and Jones and Stevenson (1975). When the refractive index is a complex value (i.e., particle collisions are included) the dispersion becomes complex, and thus the ray is traced with complex coordinates. To restrict the raytracing to real coordinates only, either the dispersion relation must not be exactly satisfied, or the Hamiltonian equations must not be exactly satisfied, or both (Jones, 1975). In this particular application we discard the imaginary part of the dispersion relation; for frequencies higher than about 3 MHz, $Im\{n\}$ (n is the index of refraction) is negligible and may be ignored during ray tracing (Budden, 1985). An alternative to ignoring the imaginary part of the refractive index is to use the real part of the refractive index for the raytracing and use the imaginary part to calculate the absorption (Argo, et al., 1994).

The raytracing program (TRACKER) used in the current ITF development is an offshoot of the original three-dimensional raytracing program developed by Jones and Stevenson (1975). The program differs significantly from the original Jones/Stevenson code in the inclusion of a realistic three-dimensional ionosphere, acoustic gravity wave perturbations, electron density enhancements and depletions, improved numerical integration routines, and graphical output. One of the difficulties associated with running the original Jones/Stephenson code was the integrator's (a Runge-Kutta/Adams-Moulton code) inability to handle sharp electron density gradients. For cases when such gradients were encountered, the program would time out after performing the maximum number of steps in attempting to calculate the ray path near the boundary. The TRACKER integration routines have significantly reduced the possibility of encountering such problems. The new routines are linear differential equation solvers developed by NIST and LANL. Ray focusing is handled using the formulation developed by Nickisch (1988), which does not require using five rays to determine the cross sectional area of the ray tube. Commands to perform multipath calculations and homing have been built into the software as well. Examples of the graphical output are displayed in Figures 2-6 through 2-9.

5.2.2.2 ITFs using three-dimensional raytracing The ITF used in this analysis was limited to longitudinal variations in receiver-transmitter location. The transmitter was kept at a constant height of 0 km above the Earth's surface. The receiver was at a constant height of 20,000 km above the surface of the Earth. Both receiver and transmitter latitudes were kept at 0°. The receiver and transmitter longitudinal separation were varied from 1° to 76°, simulating the path of a receiver in Earth orbit as its subsatellite point moves away from the interference source. The variations in transmitter-receiver geometry were limited to longitudinal separation because the interference signal model was limited to a longitudinal dependency. The ionosphere as created by ICED contained horizontal gradients which also affect the behavior of the ray paths. The procedure for creating an ITF is as follows:

1. Create the deterministic model ionosphere: select time of day, sunspot number;

2. Create the transmitter-receiver geometry: set heights and longitudinal separations;
3. Find a homed ray from transmitter to receiver at each frequency, in 0.5 MHz steps;
4. Collect information on free space loss, absorption, and focusing losses;
5. Change the receiver/transmitter separation by 5° longitude and repeat steps (1) through (4) until the transmitter is below the radio horizon.

The data on the propagation is collected and put into array form. This array is then processed to create the transmission matrix. The raw data matrix consists of frequency, elevation angle (which is a function of longitudinal separation), true propagation path length, group delay, and power loss. The data processing has been done through IDL.

The actual transmission matrices were generated for three sunspot numbers: low = 10; medium = 60; and high = 170. No auroral activity was included, since the ray paths did not traverse any polar regions. Eliminating the polar regions had the effect of speeding up the homing calculations, although the total process of ITF generation took a considerable amount of time. For cases where sources within the polar regions must be considered, the ITFs must be regenerated to allow the incorporation of auroral activity in the ionosphere. The geographical starting point for the analysis was set in the Americas. The transmission matrices for the North and South America analysis are plotted in terms of total loss in Figures 5-7 through 5-12. The ionospheric transfer functions for the other geographic regions are illustrated and discussed in Chapter 6, along with the interference predicted spectrum as seen be an Earth-orbiting interferometer. The longitudinal parameters for the ITF generation are listed in Table 5-2. The UT hour was set so that the receiver position at each region was at approximately 9:00 to 10:00 AM local time. This condition best represents the ionospheric conditions existing at the time of the WIND measurements.

Table 5-2 Ionospheric transfer function longitudinal ranges

Region	Rx longitude	Tx Longitude
North & South America	-65°	-66° (start), -142°(stop)
Western Europe & Africa	-30°	-25° (start), 25°(stop)
Eastern Europe, India, Russia	30°	35° (start), 90°(stop)
Asia, Indonesia, Australia	90°	95° (start), 150°(stop)
Pacific Islands (Guam)	155°	170° (start), -155°(stop)

The dark sections in the edges of the gray scale images correspond to locations where either the raytracing could not home to the receiver within the specified range or could not penetrate the ionosphere. In these areas, the receiver-transmitter separation in combination with the signal frequency is such that the transmitter is outside of the ionospheric "iris". The receiver is effectively shielded by the ionosphere for those combinations of frequency and longitudinal separation. The small, dark sections within the lighter areas of the image correspond to cases where the loss and focusing routines within the raytracing failed to find a solution, despite having a homed ray.

A fundamental assumption used throughout the ITF development has been that all propagation effects have been linear with respect to the transmitted power. In the actual ionosphere, a high power HF radio wave in the ionosphere will perturb the ionosphere; this will affect other radio waves propagating in the perturbed region. The E field of an alternating applied radio wave will raise the effective electron temperature within the perturbed region. A high power radio wave amplitude modulated at a frequency Ω will induce both constant and periodic (with modulation frequency Ω) plasma perturbations (Gurevich, 1978). The perturbations affect the total absorption and phase of the wave. At heights from

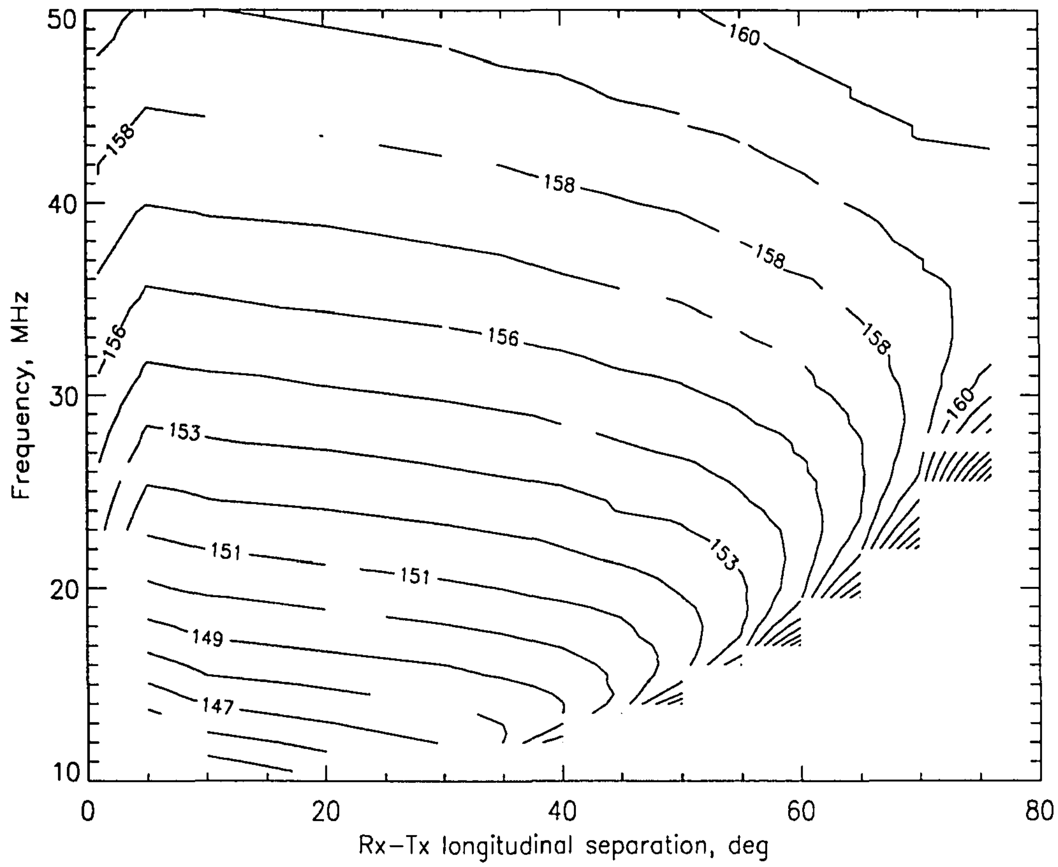

Figure 5-7 ITF for North & South America, low sunspot condition (contour)

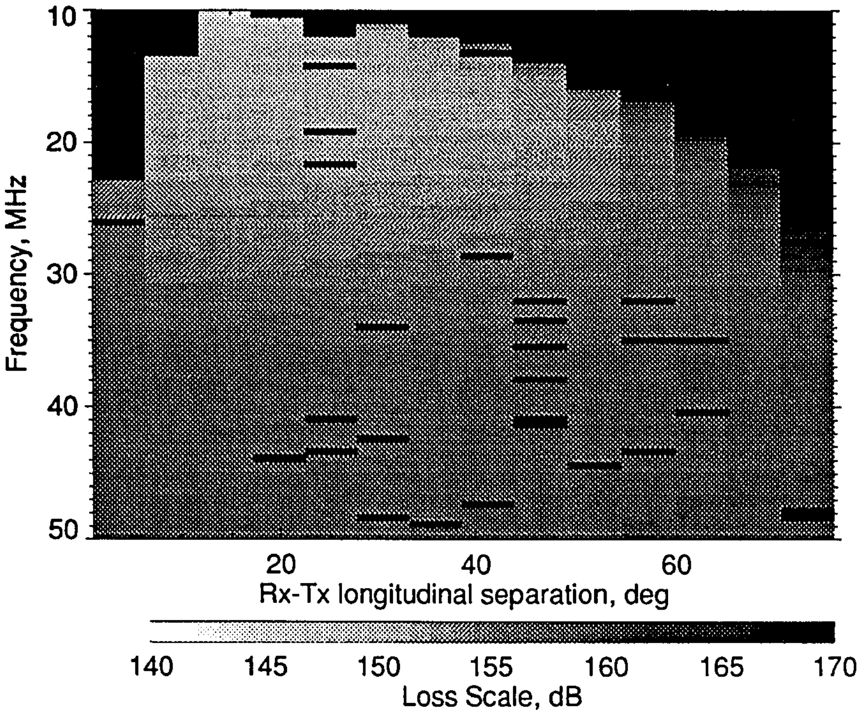

Figure 5-8 ITF for North & South America, low sunspot condition (gray scale image)

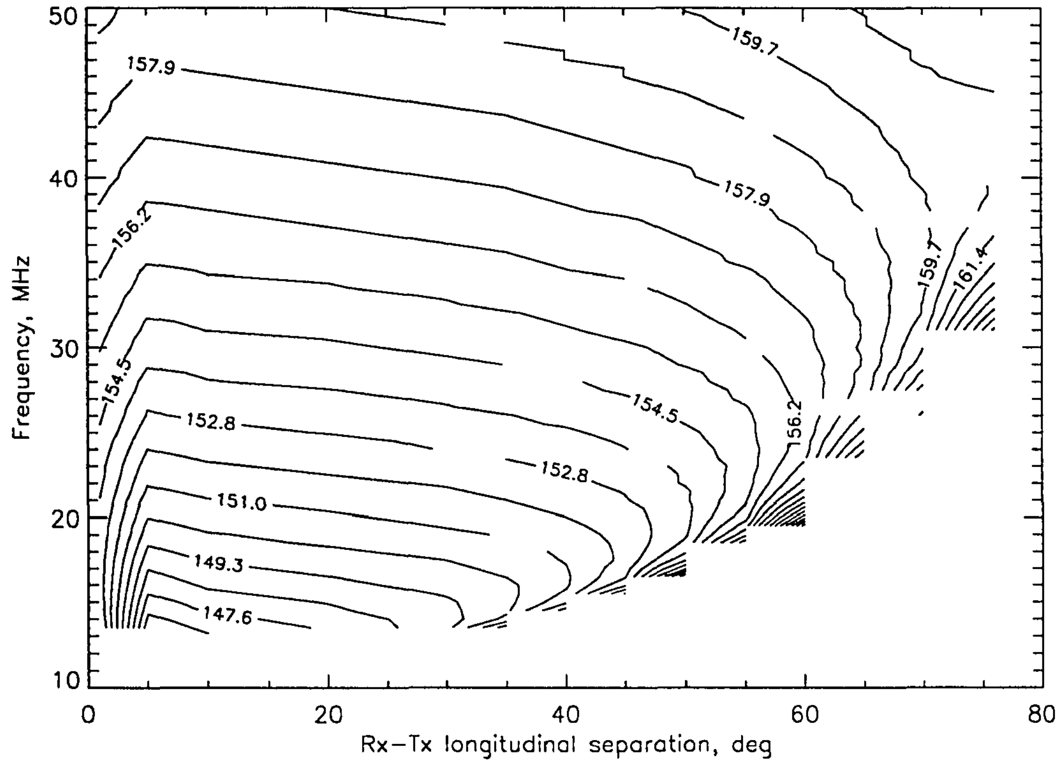

Figure 5-9 ITF for North & South America, medium sunspot condition (contour)

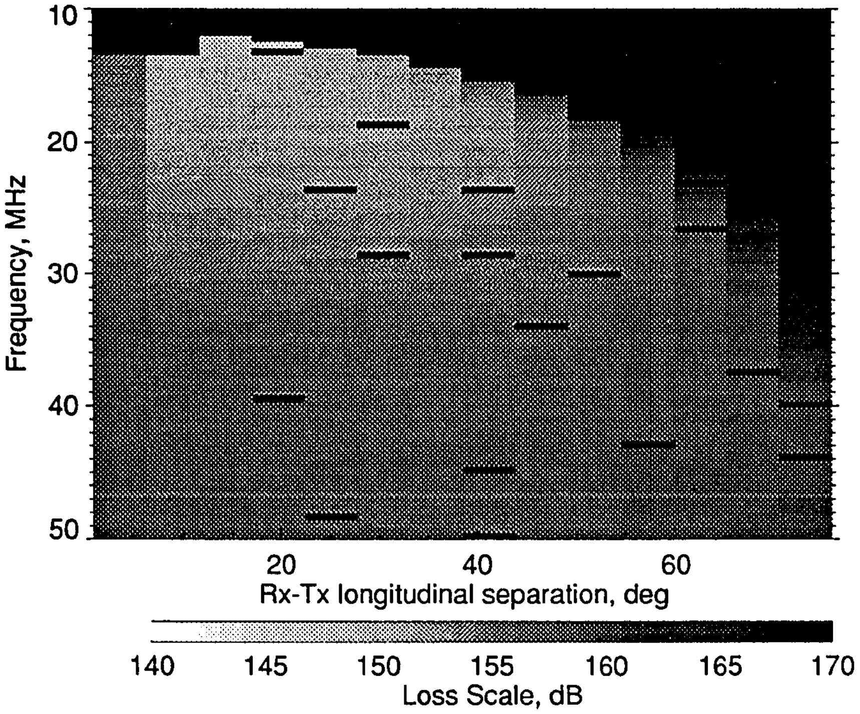

Figure 5-10 ITF for North & South America, medium sunspot condition (gray scale image)

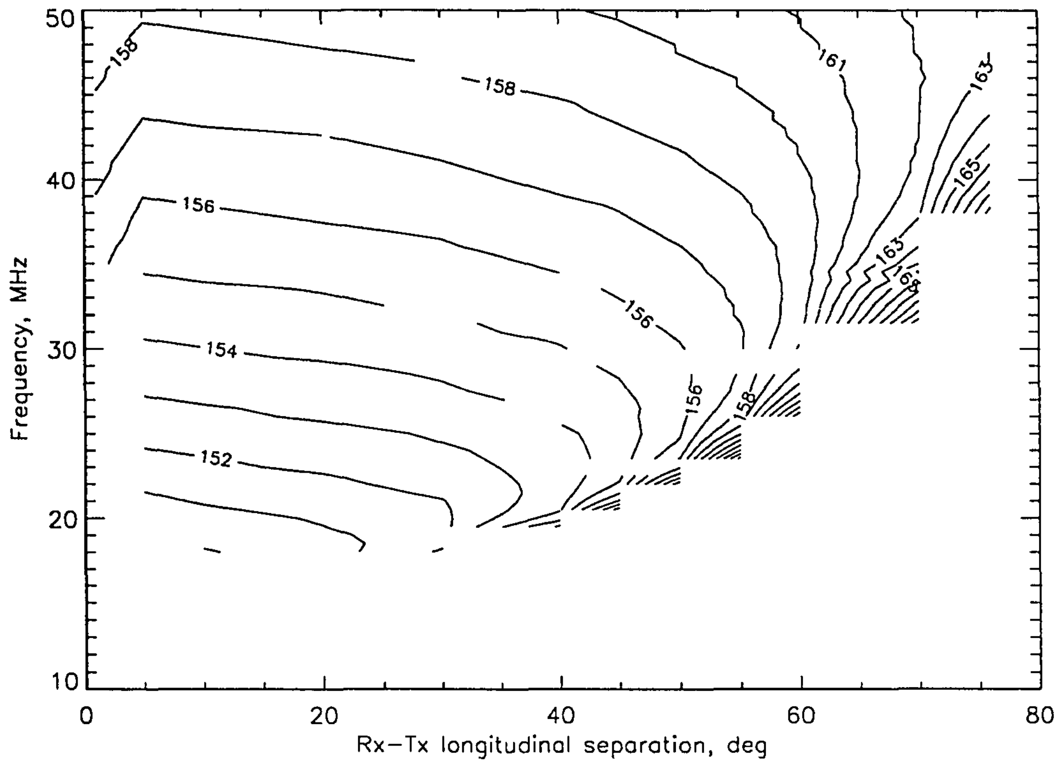

Figure 5-11 ITF for North & South America, high sunspot condition (contour)

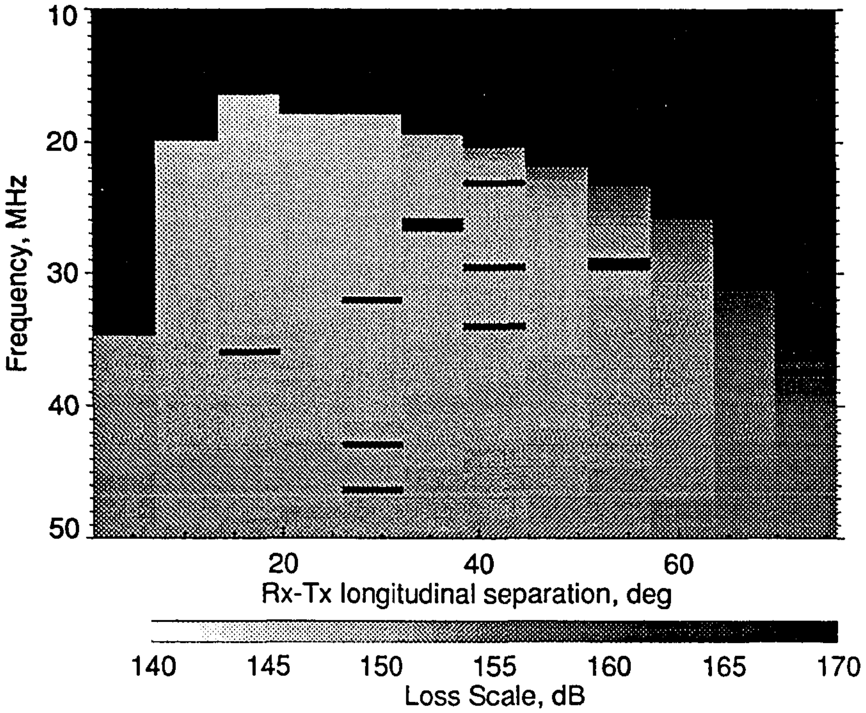

Figure 5-12 ITF for North & South America, high sunspot condition (gray scale image)

200 -- 350 km, the applied high power radio wave tends to produce an electron density decrease, given as (Gurevich, 1978):

$$\Delta N_e = -k_t \frac{N_o}{T_e} \Delta T_e \tag{5-27}$$

where ΔN_e is the change in electron density due to the applied radio wave, k_t is the thermal diffusion ratio, ΔT_e is the increase in electron temperature due to heating by the radio wave, N_o is the background electron density, and T_c is the unperturbed electron temeprature. The strongest influence is exerted by waves close to the critical frequency of the layer. Even so, the concentration of the perturbations are usually small, $\left| {}^{\Delta N_c}\!/_{N_o} \right| \approx 1\text{-}10\%$. Other radio waves propagating within that region would be defocused from the electron density depletions. For lower regions of the ionosphere, at frequencies within 1- 10 MHz, it is easy to get radio wave E field amplitudes that can lead to nonlinear effects (Gurevich, 1978). In these cases, the nonlinear processes can become significant, with much of the transmitted power going into heating the plasma. The reflected wave amplitudes would decrease with an increase in transmitter power. Th effect of obliquely propagating high power radio waves has recently been modeled (Hinkel-Lipsker, et al., 1993). This new model is a broad-based transport model to predict the temperature and density changes in the plasma due to the HF heating in the E and F layers. Simulations performed with this oblique propagation model using a transmitter power of 750 kW (greater than the typical international broadcast transmitter power) and frequency of 15 MHz indicated that the wave was reflected at an altitude of 180 km, which was lower than expected. Over 40% of the beam energy was absorbed in the D and E layers. Simulations by Hinkel-Lipsker, et al., have also shown that the heating produced an electron density enhancement of almost 18% over the background. The increase occurred over a time scale of minutes. The heating effect of a high power beam below the F layer is to create a "blob" of electron density enhancement, which acts as a divergent lens. The effect is to deflect the rays "outward" in elevation and azimuth.

The effect on terrestrial interference from these ionospheric nonlinearities is that high power transmitters at the most congested frequencies (below ~ 16 MHz) will tend to have more of their energy reflected from or absorbed within the ionosphere.

5.3 The Parabolic Equation and Phase Screen Diffraction Method

As illustrated in Figure 2-9, HF waves can be strongly distorted by the plasma density inhomogeneities. The large scale gradients can be accounted for satisfactorily by raytracing. Signal distortion caused by stochastic perturbations is more difficult to describe theoretically at HF than at other frequencies (Basler, et al., 1988). Solutions to the vector wave equations are impractical for the most part, although some progress has been made recently (Nickisch and Franke, 1993) with the recent advances in computational speed. The Finite Difference-Time Domain (FDTD) method has been used to study the accuracy of the parabolic equation method (PEM) at HF. Simulations have shown that the PEM approximations tend to overestimate the level of signal decorrelation (Nickisch, 1993).

The approach developed by Basler, et al., assumes that the scatter occurs around the mean ray path shaped by refraction. This assumption has also been followed by Nickisch (1993) and in the current research. The solution to the forward scatter problem involves the use of the parabolic wave equation in the Markov approximation (Nickisch, 1993). The channel scattering function developed by Basler and colleagues at Stanford Research Institute calculates the shape of the received signal in the range-Doppler-amplitude space. In assuming that the scatter occurs around the mean ray path, the basic calculations involve an integration along the mean ray path to find the phase structure function -- and thereby, the spatial decorrelation (tranverse to the ray path) of the wave field at the receiver. As discussed in Chapter 2, the daytime mid- and low-latitude ionosphere is much less perturbed than the nighttime ionosphere. The major perturbations encountered are TIDs of various scale sizes. Nevertheless, the background electron density does have a stochastic component.

The mutual coherence function Γ is used to describe the effects of propagation through random media. Research describing Γ for aspects of HF communications (Yeh and Liu, 1977; Knepp, 1983; Lin and Kiang, 1988; Liu, 1993) have focused on the two-frequency mutual coherence function to describe the perturbations to pulses propagating through a random medium. Pulse time of arrival and pulse width perturbations can be described by using temporal moments (Liu, 1993; Yeh and Liu, 1977) The effects of scintillation on systems which use signal phase have been widely studied for past 20 years -- one of the primary platforms for these studies has been the Defense Nuclear Agency's Wideband Satellite series, which has supplied a large quantity of information on the statistical characteristics of ionospheric irregularities and motivated an extensive modeling effort (Fremouw, et al., 1978; C. L. Rino, 1979a; C. L. Rino, 1979b; Rino and Owen, 1984).

The ionospheric medium can be described by its statistical properties. For stochastic perturbations to the background ionospheric electron density, the scale size of the ΔN_e perturbations has been shown to follow a power-law spectral density function (Yeh and Liu, 1977; Rino, 1979a). This assumption has been employed by Basler, et al. (1988) and Nickisch (1993), although Basler uses a single component to describe the perturbation spectrum, while Nickisch uses a two component power law spectrum. Two scales, inner (l_0) and outer (L_0), describe the spectrum of the irregularities. The outer scale is a somewhat arbitrary division between well-developed , stable structures (statistically homogeneous) and evolving structures that depend on the initial plasma configuration at the time of the instability onset (Rino, 1979a). Evidence shows that outer scale sizes are on the order of tens of kilometers. The inner scale size may be as low as five meters (Rino, 1979a). The fractional electron density perturbation, $\xi = \Delta N/\langle N \rangle$, is typically used, where ΔN is the random perturbation to the background electron density (Yeh and Liu, 1977). ξ can be described by its autocorrelation function B_ξ. B_ξ can take a three-, two, or one-dimensional spectrum, depending on the anisotropy of the irregularities (Yeh and Liu, 1977). V_ξ, the spectrum of B_ξ, is simply its Fourier transform:

$$V_\xi = \frac{1}{2\pi} \int_{-\infty}^{\infty} B_\xi \, e^{-j\kappa_x x} dx \tag{5-28}$$

where κ_x is the wave number. The power law form of describing the stochastic perturbations is applied to V_ξ, i.e., $V_\xi \propto \kappa_x^{-m}$, with $m \approx 2$. This form has been shown to be valid for scales on the order of tens of meters to tens of kilometers. The full form of V_ξ is much more complex, involving modified Bessel functions (Yeh and Liu, 1977). For $k_o << \kappa_x << 1/l_o$, it simplifies to

$$V_\xi(\kappa_x) = \frac{\sigma_n^2 \Gamma\left(\frac{m}{2}\right) k_o^{m-1}}{\sqrt{\pi}\, \Gamma\left(\frac{m-1}{2}\right)} \cdot \frac{1}{\left(k_o^2 + \kappa_x^2\right)^{m/2}} \tag{5-29}$$

where Γ in this equation is the gamma function; $\sigma_n{}^2$ is the variance of the fractional electron density perturbation, ξ; and L_o, the outer scale, is equivalent to $2\pi/k_o$. The overall behavior of equation (5-29) is that of κ_x^{-m}.

The phase screen diffraction method (PDM) is designed to solve the propagation problem with random electron densities or small-scale electron density perturbations, where the fundamental geometrical optics approximations in raytracing become invalid. The PDM technique is used to determine the mutual coherence of the wavefront that has propagated through the perturbed ionosphere. The two-position mutual coherence function $\Gamma(\mathbf{r}_1,\mathbf{r}_2)$ will describe the decorrelation of the interference from a single source at the the separate interferometer elements. Solutions for the mutual coherence (second moment equation) for strong and weak scattering have been obtained using the phase screen (Knepp, 1983; Rino, 1979a, 1979b) and temporal moment (Yeh and Liu, 1977) theories. The multiple phase screen approach has proved invaluable to the simulation of the effects of stochastic perturbations on transionospheric waves. The methodology employed here follws that of Nickisch (1993) in that the mutual coherence function is solved for directly using the parabolic equation method, rather than solving the for the wave fields in a random realization and then ensemble averaging.

Starting with the scalar Helmholtz wave equation,

$$\nabla^2 u(\bar{r}) + k_0^2 \varepsilon_r u(\bar{r}) = 0 \tag{5-30}$$

where $u(\bar{r})$ represents any component of the vector field, k_0 is the free space wave number, and ε_r is the relative dielectric constant of the plasma. Note that ε_r has a smooth component, due to the background electron density, and a superimposed random component, due to the random structure in the ionosphere:

$$\varepsilon_r = \langle \varepsilon_r \rangle [1 + \varepsilon_1] \tag{5-31}$$

where the $\bar{r}$ dependence has been dropped for convenience. $\varepsilon 1$ can be found from the ξ described above. Using the forward scatter assumption (where backscatter from the perturbations is neglected) and assuming that the propagation will be confined to small angular deviations from the mean ray path (determined by the background electron density), we can write the field as

$$u(\bar{r}) = U(\bar{\rho})e^{jkz} \tag{5-32}$$

with $\bar{\rho} = (\bar{x}, \bar{y})$, and U signifying a complex amplude. The (x,y,z) coordinate convention does not imply that a rectangular coordinate system has been adopted; they are used for simplicity in writing the coordinates. $U(\bar{\rho})$ is assumed to be slowly varying spatially. Substituting equation (5-26) into equation (5-24) and assuming that $\partial^2 U(\bar{\rho})/\partial z^2$ is negligible as long as the scale of the variation in $U(\bar{\rho})$ (along the direction of propagation) remains large with respect to the wavelength, we find that the scalar Helmholtz wave equation becomes

$$\nabla_{\perp}^2 U(\bar{r}) + 2jk\frac{\partial U(\bar{r})}{\partial z} + k^2 \varepsilon_1 U(\bar{r}) = 0 \tag{5-33}$$

where k^2 is $k_o^2 \langle \varepsilon_r \rangle$, and $\nabla_{\perp}^2$ is the Laplacian acting on the transverse coordinates (x,y) of the complex amplitude U. Equation (5-33) is the parabolic wave equation that forms the basis of the mutual coherence function. A derivation of the two-position mutual coherence function from the parabolic equation, using the Markov approximation, can be found in Chapter 19 of Ishimaru (1978).

The two position mutual coherence function implicitly assumes that the function does not depend on the absolute positions of the fields, but on their spatial separations (Nickisch and Franke, 1993; Ishimaru, 1978), i.e.,

$$\Gamma(\Delta\bar{\rho}, z) = \left\langle U(\bar{\rho} + \Delta\bar{\rho}, z) U^*(\bar{\rho}, z) \right\rangle \tag{5-34}$$

where the angle brackets signify ensemble averaging and U* is the complex conjugate of U.

The parabolic equation for the mutual coherence function can be written as (Nickisch, 1992):

$$\frac{\partial \Gamma}{\partial z} - \frac{j}{2}\frac{k_d^2}{k^2}\frac{1}{z^2}\left[\frac{\partial^2}{\partial \zeta_x^2} + \frac{\partial^2}{\partial \zeta_y^2}\right]\Gamma + A\left(\zeta_x z, \zeta_y z, t; z\right)\Gamma = 0 \tag{5-35}$$

where Γ has been previous defined as the mutual coherence function, $\zeta_x = x/z$ and $\zeta_y = y/z$. The variable A is known as a source term, representing the autocorrelation of the function of the irregularities.

The phase screen diffraction method simply replaces the continuous, irregular medium by a number of thin screens that impose phase fluctuations onto a signal propagating through the screens. These screens are taken to be orthogonal to the direction of propagation. The number of screens need not be high (L. J. Nickisch, personal communication, 1995). Simulations have shown that the numerical results using twelve screens are essentially indistinguishable from the exact solution of the parabolic equation (Nickisch, 1992a; Nickisch, 1992b). The computational disadvantage of using a large number of phase screens must be weighed with the need for flexibility in representing a complex, turbulent medium. Diffractive effects are ignored at the screens themselves, but developed in between the screens. For multiple screens, the source term A is

$$A(x,y,t;z) = \sum_{i=1}^{ns} A_i(\zeta_x, \zeta_y, t; z)\,\delta(z - z_i) \tag{5-36}$$

the variable ns refers to the number of screens used in the simulation; z_i is the location of the ith screen along the ray path. Define $z_{i,-}$ ($z_{i,+}$) as the propagation coordinate just before (after) the screen. Ignoring diffraction at the screen, the mutual coherence after the screen can be found as a function of both the mutual coherence before the screen and the source term:

$$\Gamma\left(\zeta_x,\zeta_y,t;z_{i,+}\right)=\Gamma\left(\zeta_x,\zeta_y,t;z_{i,-}\right)\cdot\exp\left\{-A\left(\zeta_x,\zeta_y,t;z_i\right)\right\} \tag{5-37}$$

In equation (5-37), z_i is the location of the ith screen. Between the screens, the source term A does not exist, and the mutual coherence function at the (i+1)st screen can be found by Fourier transforming the mutual coherence at the ith screen:

$$\tilde{\Gamma}\left(K\zeta_x,K\zeta_y,t;z_{i+1,-}\right)=\tilde{\Gamma}\left(K\zeta_x,K\zeta_y,t;z_{i,+}\right)\cdot\exp\left\{-j\omega\left[\left(K\zeta_x\right)^2+\left(K\zeta_y\right)^2\right]P_i\right\} \tag{5-38}$$

with P_i ,the free space propagation term, given by

$$P_i=\frac{1}{2c}\frac{1}{k^2}\left[\frac{1}{z_i}-\frac{1}{z_{i+1}}\right] \tag{5-39},$$

describing the propagation from the ith screen to the (i+1)st screen. The boundary condition at the bottom of the first screen is $\Gamma=1$. The solution to the mutual coherence function can then be found by applying equation (5-37), Fourier transforming the result, propagating to the next screen via equation (5-38), inverse Fourier transforming, and repeating the process until all screens have been encountered. Γ is then propagated to the end point of the ray path using equation (5-38). This process is generally done numerically, although analytic solutions can be found for quadratic forms of A (Nickisch, 1992a; Nickisch, 1992b).

This process has been implemented in a Fortran code that uses the information generated by raytracing to determine the Briggs-Parkin angle (see Chapter 2) and the location of the screens. The source term A can be taken as a quadratic (L. J. Nickisch, personal comunication, 1995), A(x,y) = Ao+A2x² + A2y², assuming the ionospheric irregularities are cylindrically shaped (approximating the geomagnetic field alignment). For each screen, A is

$$A_i(\zeta_x,\zeta_y,t;z) = S_{x,i}(\zeta_x - \upsilon_{xi})^2 + S_{y,i}(\zeta_y - \upsilon_{yi})^2 \qquad (5\text{-}40)$$

with υ representing a normalized plasma velocity. Each screen can have a different υ, allowing the plasma velocity to vary according to location and altitude. The plasma velocity model used in the current research is that of Richmond, et al. (1980). The $S_{x,i}$ and $S_{y,i}$ factors are functions of the A2's, the ionospheric thickness L, and the plasma wave number k_p (= $2\pi/f_p$). The structure parameters used are Lo = 30 km, m = 1.9, L|| (scale of the irregularity parallel to the geomagnetic field) = 100 km. From this, the variance of the angle of arrival in the x direction, which describes the variation in break through ray end points can be found as (Knepp, 1985):

$$\sigma^2_{\zeta_x} = \frac{-1}{k^2}\frac{\partial^2\Gamma(x,y,t=0;z=z_{sat})}{\partial x^2}\bigg|_{x=y=0} \qquad (5\text{-}41)$$

For the quadratic form of the structure function, $\sigma_{\zeta_x} \approx \sqrt{2}/(k\,l_x)$, where l_x is the correlation length in the x direction. When propagating orthogonal to the irregularities, such as might be encountered at middle and low latitude transionospheric rays, the irregularities can be considerd to be one-dimensional (Nickisch, 1992b). The variable y and factor A2y can both be set to 0. The transformation will then be strictly over x.

The nonuniform plasma velocity over the screens has been studied by Nickisch (1992b). Differences in the velocity profiles result in large differences in the scattering function (time delay versus Doppler frequency).

It is important to consider the regions of validity for the phase screen implementation of the parabolic wave equation. In the Finite-Difference Time Domain approach, the only approximations necessary to its development are the discretization of the spatial permittivity and the field components. However, two very critical assumptions were made in the steps leading from a vector wave equation to the parabolic wave equation: the assumption that polarization coupling was negligible, and that the wave is limited to small-angle, forward scattering. First, the assumption that the polarization coupling term ($\nabla(\nabla \cdot \bar{E})$) can be neglected is generally valid when the free space radio wavelength is much smaller than the ionospheric structure scale size. The forward scattering assumption ($\partial^2 U / \partial z^2 \approx 0$) also holds when the free space wavelength is smaller than the field correlation length. In this case, we assume that contribution of the scattered field at some observation point r comes mainly from scattering from irregularities in a small cone with its vertex at $\bar{r}$ and with an aperture of $\vartheta' = \lambda / l_o << 1$. Computer simulations performed by Nickisch and Franke (1993) compared the performance of the vector and scalar Helmholtz wave equations with the phase screen implementation of the parabolic equation. The numerical estimates of the correlation lengths for all three methods were of the same order of magnitude. However, as the simulation frequency decreased (making λ larger than the structure scale size and violating the two underlying assumptions of the parabolic equation), the FDTD estimates began to depart radically from the parabolic equation estimate. For modeling applications where the radio wavelength becomes much larger than the structure scale size, the phase screen method will tend to predict smoother, more coherent fields than actually exist.

CHAPTER 6
MODEL VERIFICATION AND PREDICTIONS

6.1 Model Predictions

In this chapter, we will compare and contrast the simulated interference spectra with the interference measured by the WIND spacecraft. All of the simulated interference spectra presented in this chapter have been normalized from power (in dBW) to flux density (in dB [W/m^{2}Hz]) using

$$S(f) = \frac{P_r(f)}{B A_c} \tag{6-1}$$

where S(f) is the flux density of the signal incident at the receive antenna; B is bandwidth in Hertz; and A_e is the effective aperture of the receive antenna. For a signal with a bandwidth $B_s << B_r$ (receiver RF bandwidth), the appropriate bandwidth to use in equation (6-1) is B_s. For wideband signals having $B_s \geq B_r$, the appropriate choice for B in equation (6-1) is B_r. An equivalent expression for the log of the flux density is easily calculated as

$$S(f)\ \left(\mathrm{dB}\ \frac{\mathrm{W}}{\mathrm{m}^2\ \mathrm{Hz}}\right) = P(f)\ (\mathrm{dBW}) - 10\log_{10} f\ (\mathrm{Hz})\ -\ 10\log_{10} A_c\ \left(\mathrm{m}^2\right) \tag{6-2}$$

with the units shown in parentheses next to each of the variables in the equation.

One of the fundamental assumptions in performing the interference study has been that the interference signals have a much narrower bandwidth (in this case, 1 kHz is assumed) than either the RAD2 receiver on WIND (see Chapter 4) or a receiver on board an orbiting interferometer (see Chapter 1). The effective aperture A_e (= $.75\lambda^2/\pi$) used for the normalization is that of an electrically short monopole, similar to the E_z spin-axis antenna on WIND.

The following subsections are organized by solar condition, i.e., low, medium, and high sunspot number. The low sunspot number subsection contains the most detailed presentation, in keeping with the data available for model verification. No plots of the predicted spectra are included for the medium and high sunspot number cases. An analysis of the ITFs for these cases(medium and high sunspot number) has shown that:

1. for medium sunspot numbers, the minimum breakthrough frequency is approximately 14 MHz;
2. for high sunspot numbers, 17 MHz is the minimum frequency to breakthrough the daytime ionosphere. This is clearly illustrated in Figures 5-11 and 5-12.

At frequencies above 17 MHz, it is commonly understood that the ionosphere provides very little shielding for any part of the solar cycle.

6.1.1 Low sunspot activity

This scenario is the most likely to match the WIND observations, since the data was collected near the minimum of the sunspot cycle. The spectra are organized by major world region, discussed previously in Chapter 5. In each case, the predicted, unmodified interference flux density is shown first. Then, the interference flux density as it has been modified by the ionospheric transfer function is shown. This spectrum is the predicted interference flux density (with respect to a nominal galactic background flux density of -190 dB [W/m^2 Hz]) at an altitude of 40,000 km above the earth's surface. Finally, two spectra from the WIND data set are included for comparison to the predicted interference. It is important to keep in mind that the WIND measurements were taken from a distance of 20 to 40 R_E, which introduces an additional 10 to 16 dB of attenuation.

6.1.1.1 *North and South America* The hemisphere containing North and South America, as viewed by the WIND spacecraft is illustrated in Figure 6-1. The simulated spectra before and after modification by the appropriate ionospheric transfer function are shown in Figures 6-2 and 6-3; the spectra as measured by WIND are shown in Figures 6-4 and 6-5.

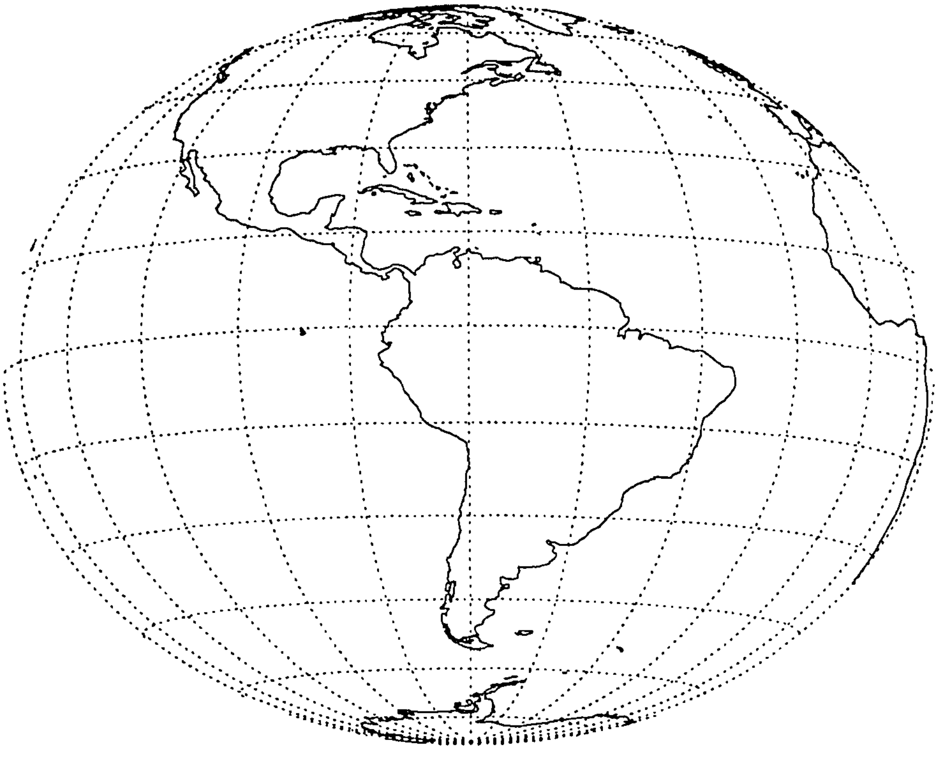

Figure 6-1 The American hemisphere as seen by WIND (14 hours UT)

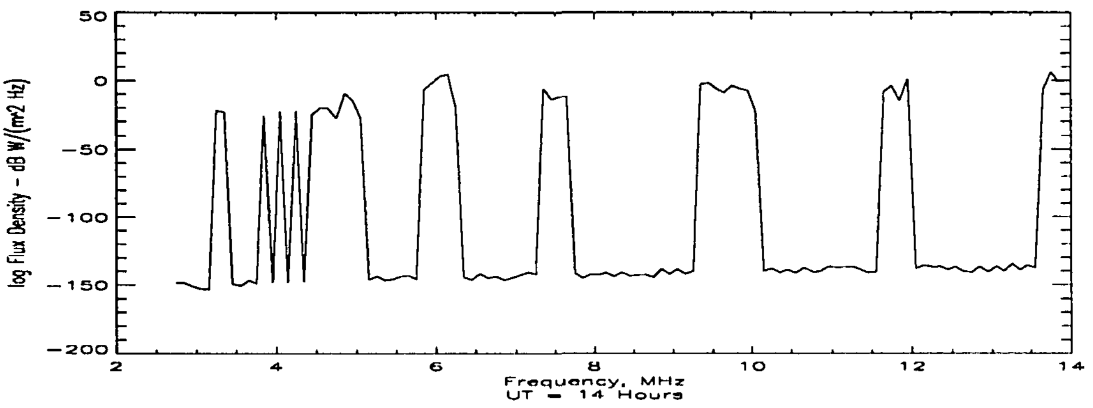

Figure 6-2 Simulated interference flux density prior to propagation through the ionosphere (North and South America)

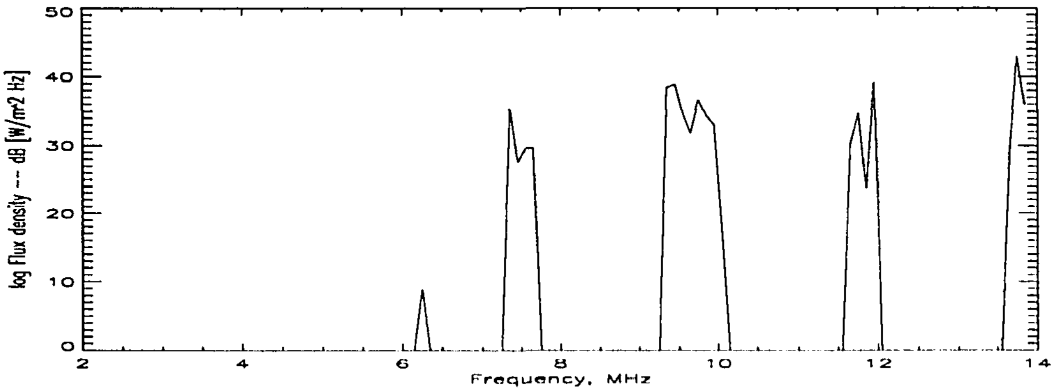

Figure 6-3 Simulated interference spectrum after modification by ITF (North and South America)

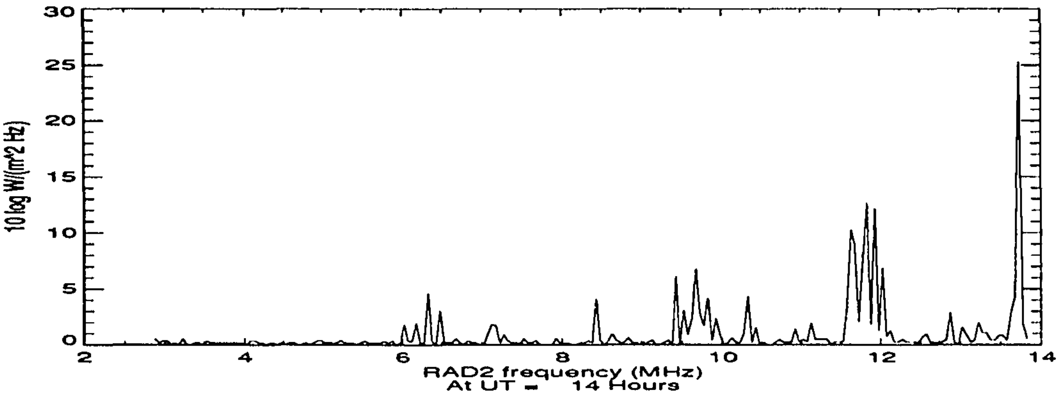

Figure 6-4 Corresponding spectrum measured by WIND (November 17, 1994 -- North and South America)

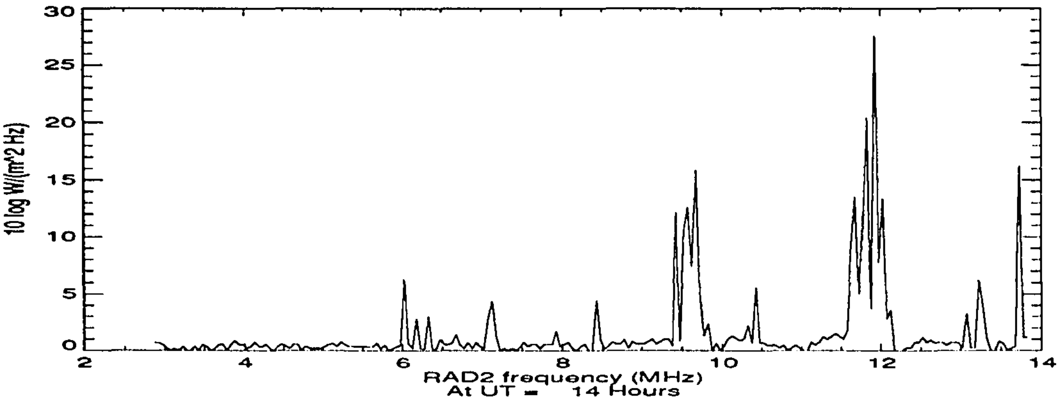

Figure 6-5 Corresponding spectrum measured by WIND (December 2, 1994 -- North and South America)

6.1.1.2 *Western Europe and Africa* The hemisphere containing western Europe and Africa, as viewed by the WIND spacecraft, is illustrated in Figure 6-6. Note that other geographical regions are within the spacecraft's field of view. The simulated spectra before and after modification by the ionospheric transfer function are shown in Figures 6-7 and 6-8; the spectra as measured by WIND are shown in Figures 6-9 and 6-10.

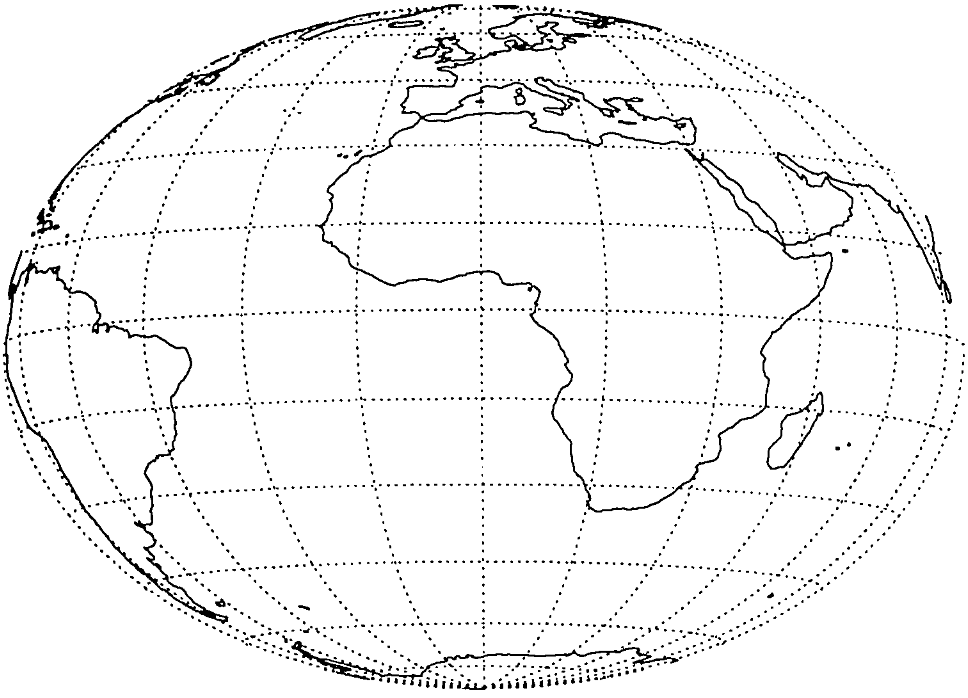

Figure 6-6 The hemisphere as seen by WIND (9 hours UT)

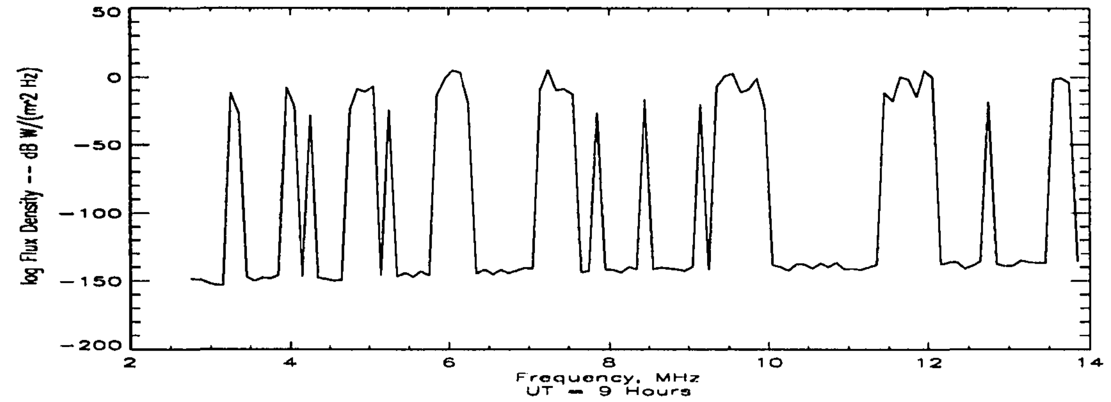

Figure 6-7 Simulated interference flux density prior to propagation through the ionosphere (Western Europe and Africa)

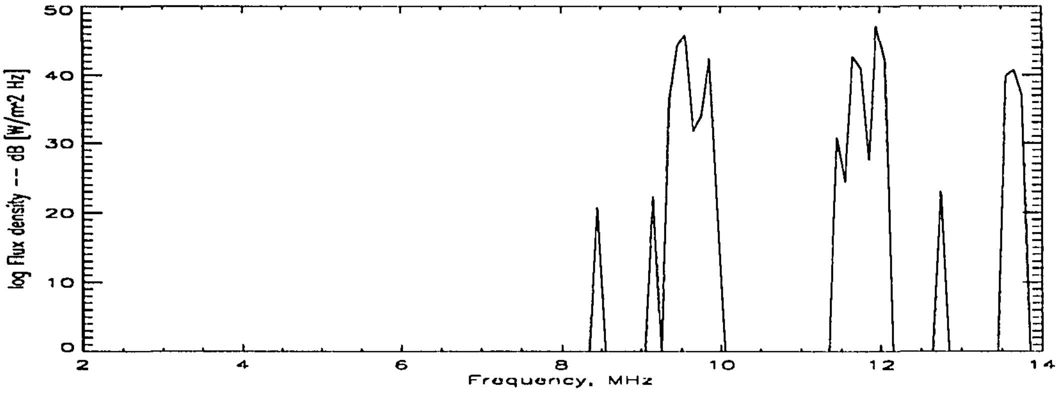

Figure 6-8 Simulated interference spectrum after modification by ITF (Western Europe and Africa)

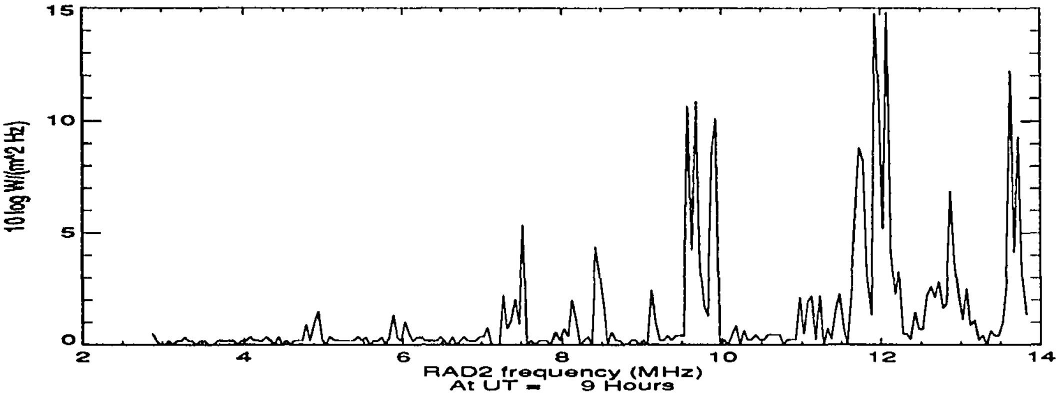

Figure 6-9 Corresponding spectrum measured by WIND (November 17, 1994 -- Western Europe and Africa)

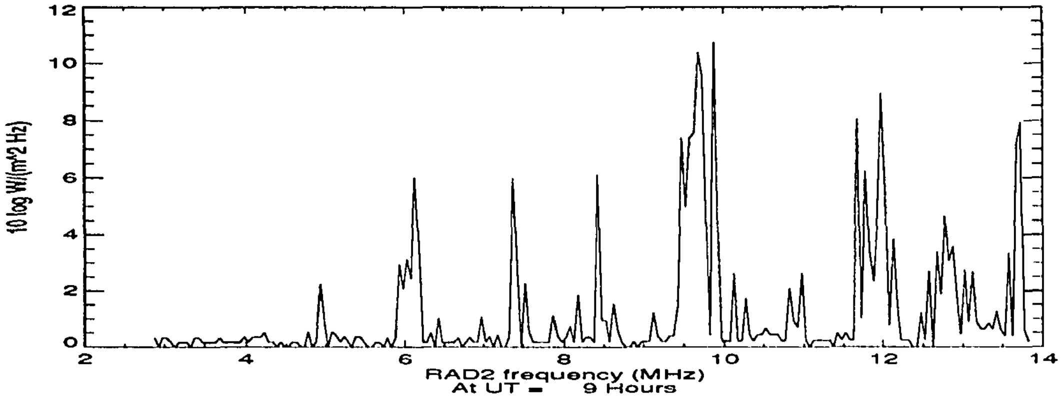

Figure 6-10 Corresponding spectrum measured by WIND (December 2, 1994 -- Western Europe and Africa)

6.1.1.3 *Eastern Europe, India, and Russia* The hemisphere containing Eastern Europe, Russia, and India, as viewed by the WIND spacecraft, is illustrated in Figure 6-11. As mentioned previously, other geographical regions are within the spacecraft's field of view. The simulated spectra before and after modification by the ionospheric transfer function are shown in Figures 6-12 and 6-13; the spectra as measured by WIND are shown in Figures 6-14 and 6-15.

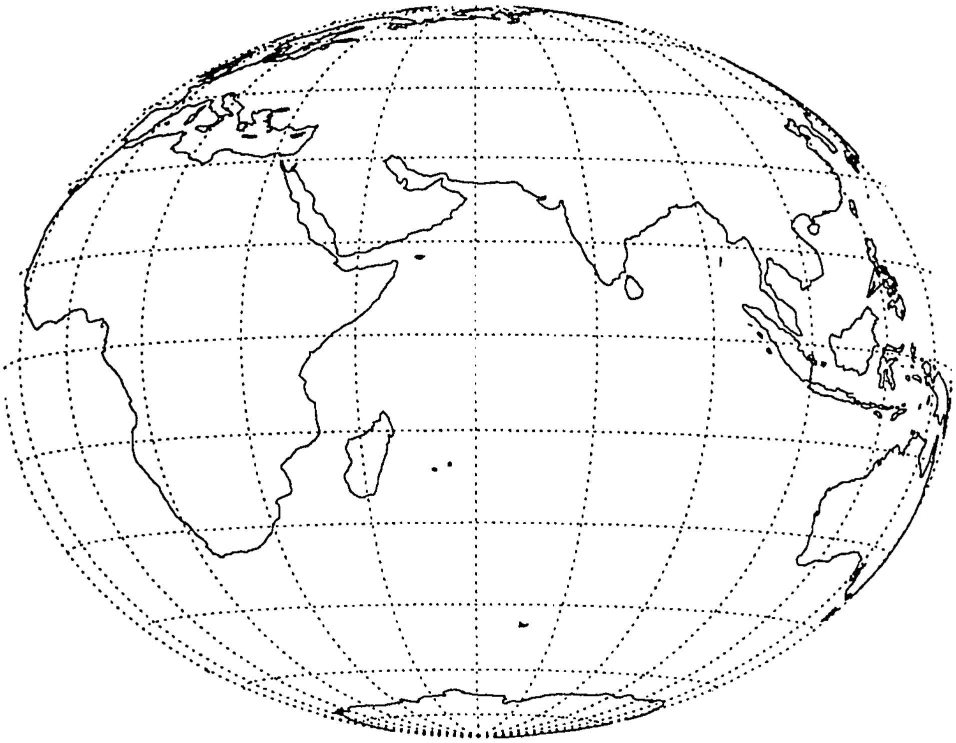

Figure 6-11 The hemisphere as seen by WIND (5 hours UT)

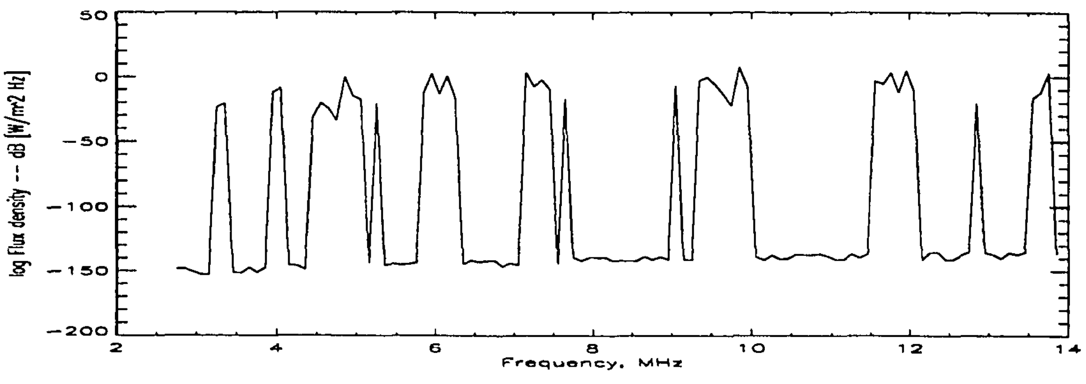

Figure 6-12 Simulated interference flux density prior to propagation through the ionosphere (Eastern Europe, Russia, and India)

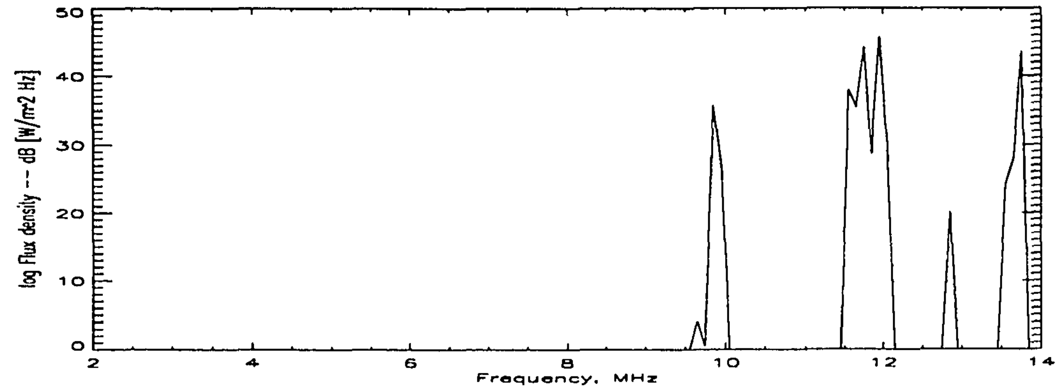

Figure 6-13 Simulated interference spectrum after modification by ITF (Eastern Europe, Russia, and India)

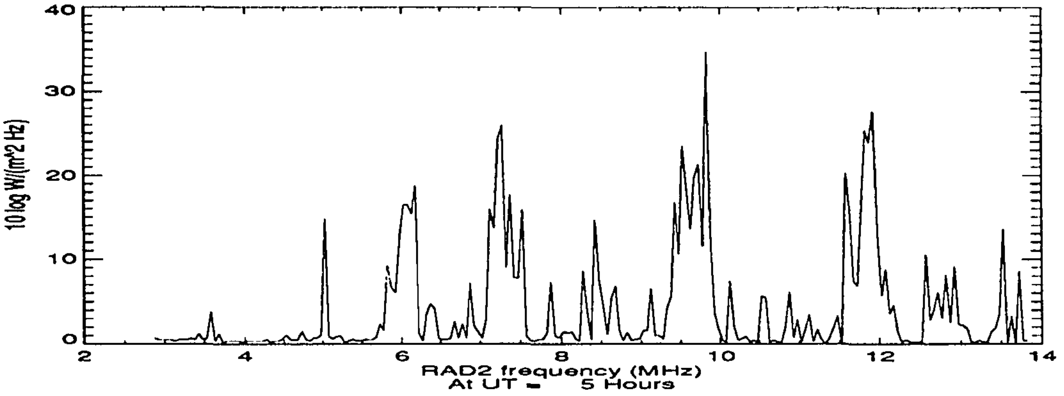

Figure 6-14 Corresponding spectrum measured by WIND (November 17, 1994 -- Eastern Europe, Russia, and India)

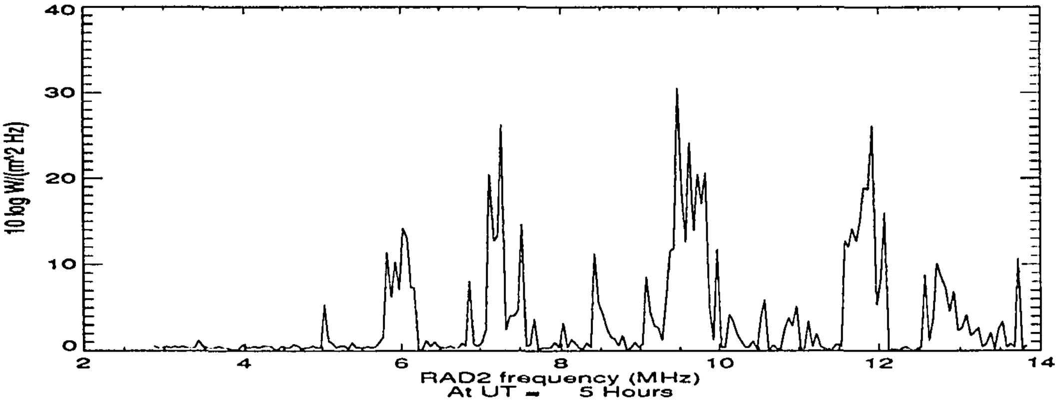

Figure 6-15 Corresponding spectrum measured by WIND (December 2, 1994 -- Eastern Europe, Russia, and India)

6.1.1.4 *Asia, Indonesia, and Australia* The hemisphere containing Asia, Indonesia, and Australia, as viewed by the WIND spacecraft, is illustrated in Figure 6-16. As mentioned previously, other geographical regions are within the spacecraft's field of view. The simulated spectra before and after modification by the appropriate ionospheric transfer function are shown in Figures 6-17 and 6-18; the spectra as measured by WIND are shown in Figures 6-19 and 6-20.

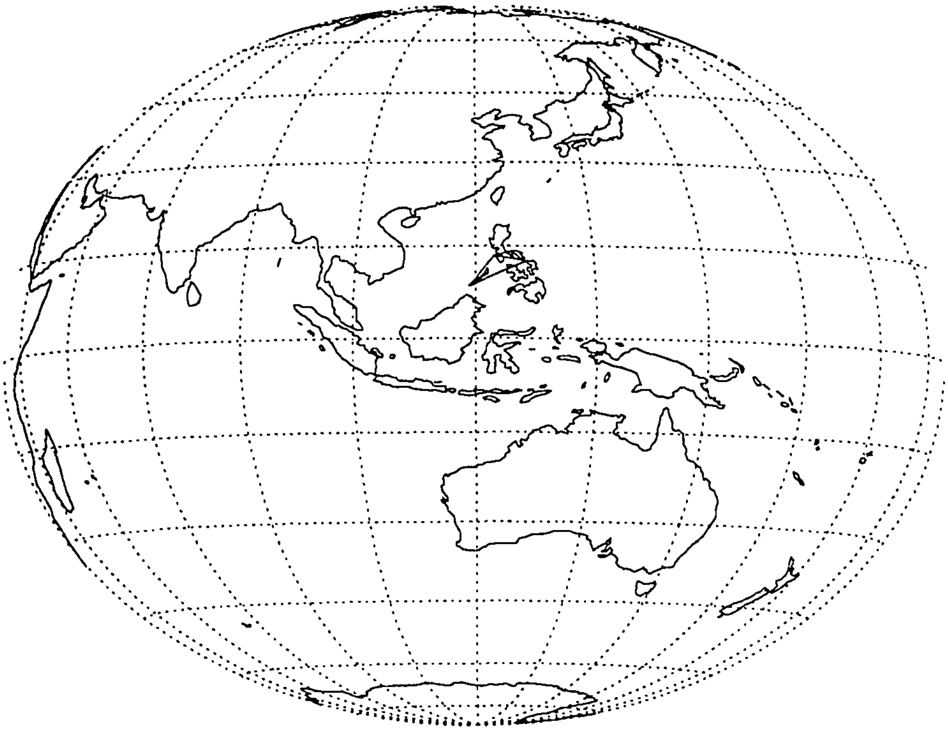

Figure 6-16 The hemisphere as seen by WIND (1 hour UT)

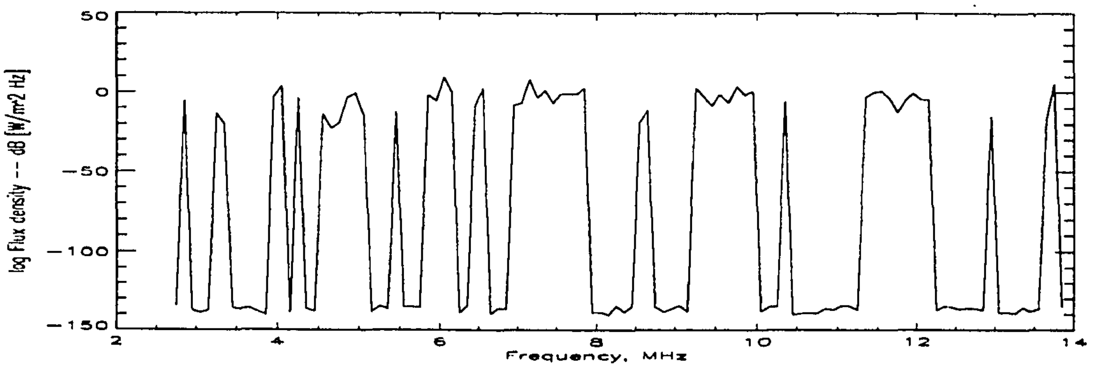

Figure 6-17 Simulated interference flux density prior to propagation through the ionosphere (Asia, Indonesia, and Australia)

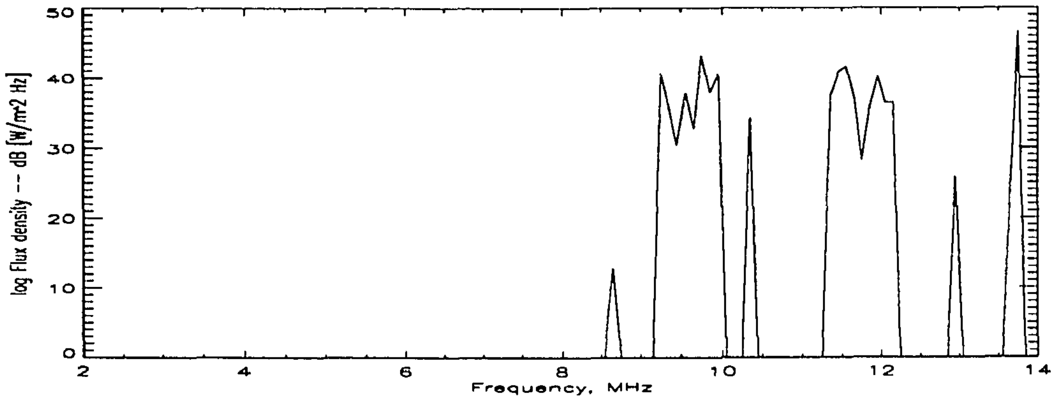

Figure 6-18 Simulated interference spectrum after modification by ITF (Asia, Indonesia, and Australia)

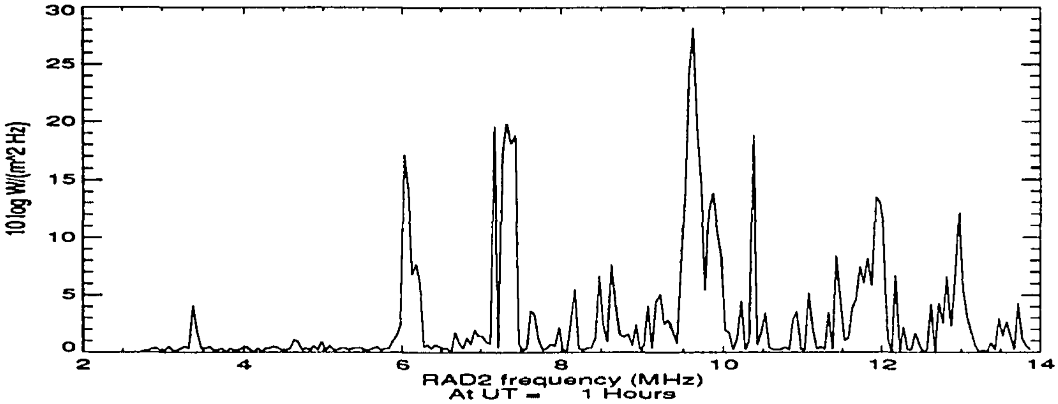

Figure 6-19 Corresponding spectrum measured by WIND (November 17, 1994 -- Asia, Indonesia, and Australia)

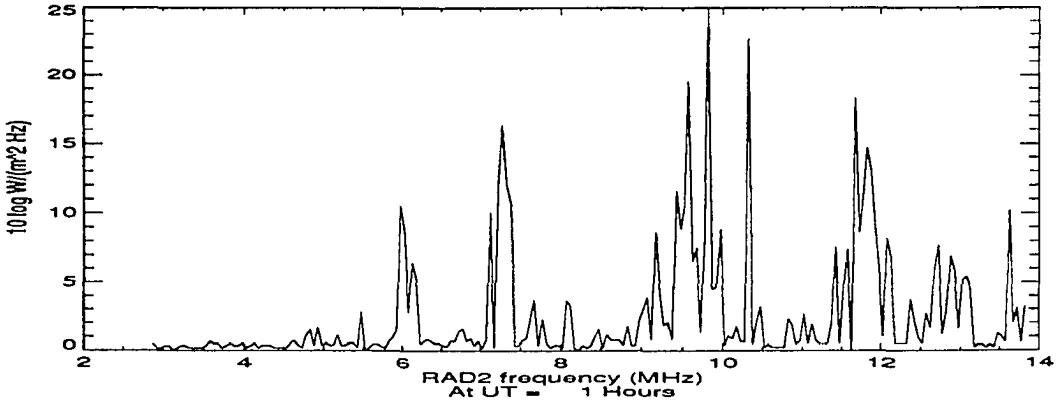

Figure 6-20 Corresponding spectrum measured by WIND (December 2, 1994 -- Asia, Indonesia, and Australia)

6.1.1.5 *Pacific Islands (Guam)* The hemisphere containing the islands of the Pacific, as viewed by the WIND spacecraft, is illustrated in Figure 6-21. Unlike some of the other regions, there is less overlap of the spacecraft's field of view with other geographical regions. The simulated spectra before and after modification by the appropriate ionospheric transfer function are shown in Figures 6-22 and 6-23; the spectra as measured by WIND are shown in Figures 6-24 and 6-25.

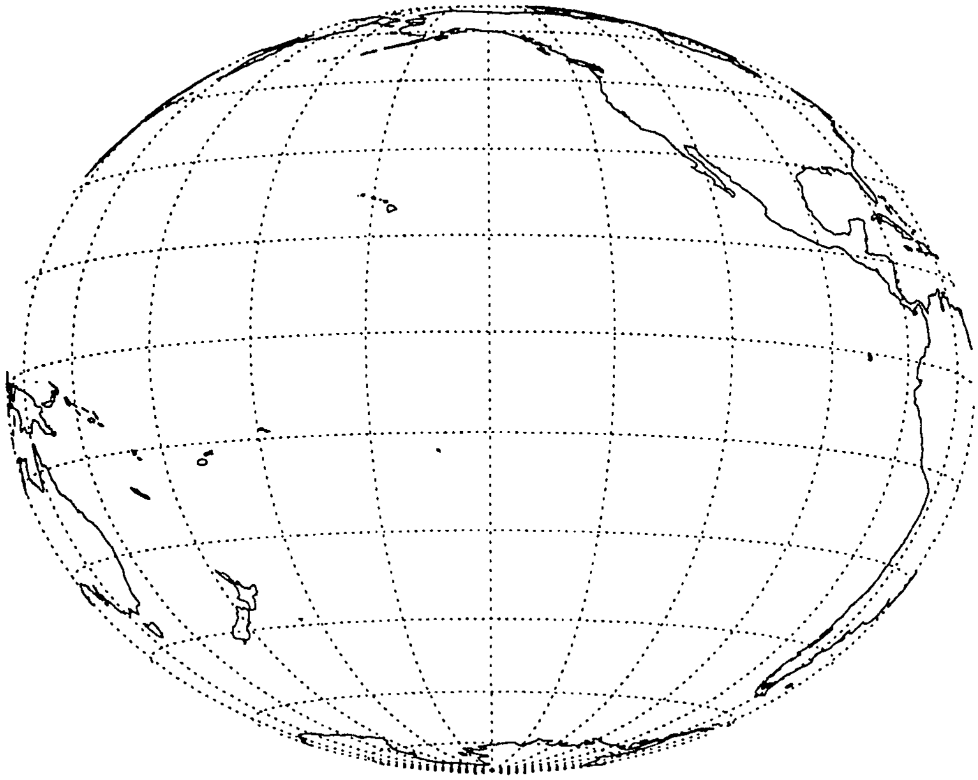

Figure 6-21 The hemisphere as seen by WIND (19 hours UT)

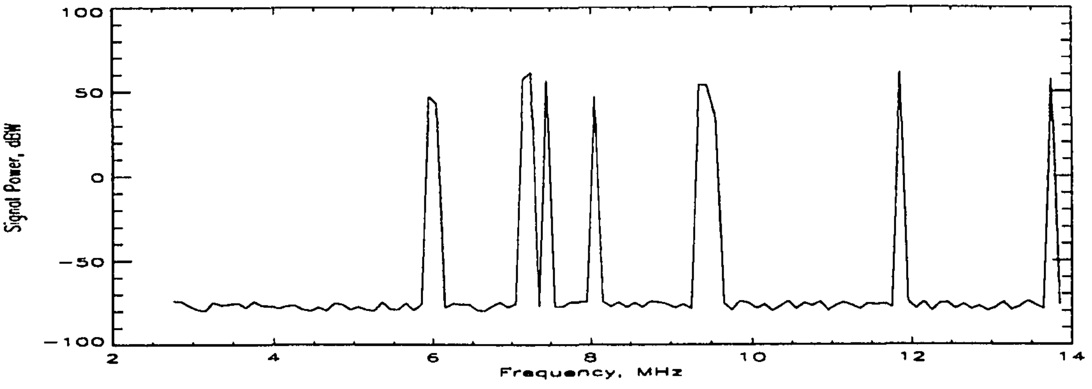

Figure 6-22 Simulated interference flux density prior to propagation through the ionosphere (Pacific Islands/Guam)

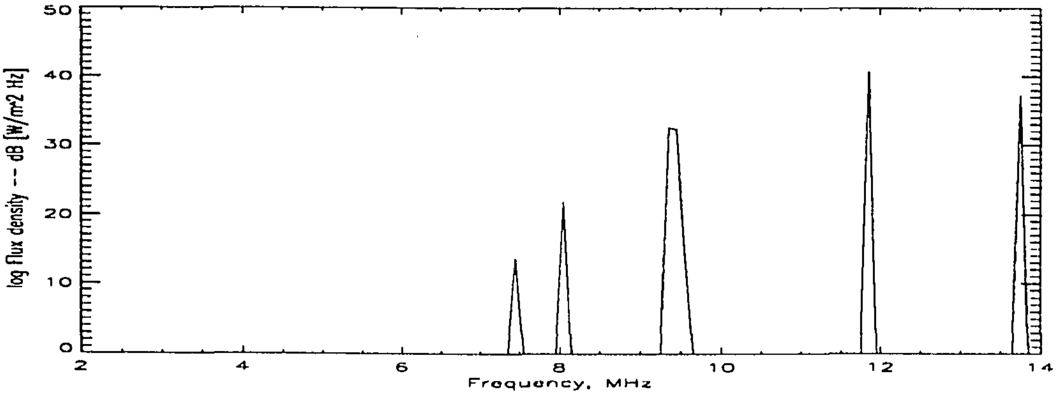

Figure 6-23 Simulated interference spectrum after modification by ITF (Pacific Islands/Guam)

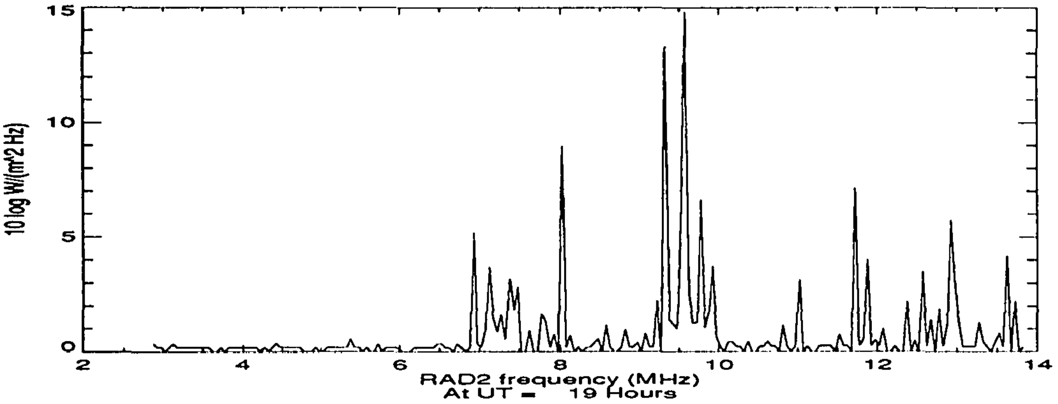

Figure 6-24 Corresponding spectrum measured by WIND (November 17, 1994 -- Pacific Islands/Guam)

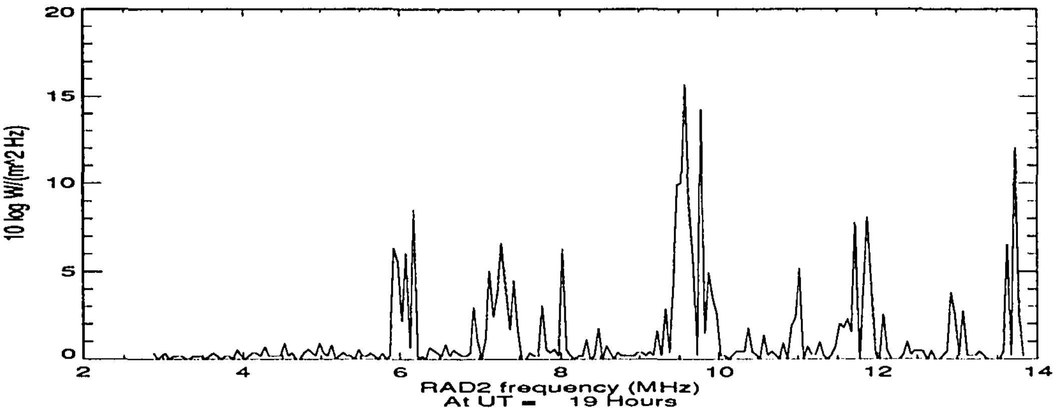

Figure 6-25 Corresponding spectrum measured by WIND (December 2, 1994 -- Pacific Islands/Guam)

6.1.2 Medium sunspot activity

For the case of a medium sunspot number, the low frequency end of the ITF shifts slightly upward, as can be seen by comparing Figures 5-7 and 5-9 or Figures 5-8 and 5-10. This shift of a few MHz may be sufficient to improve the observations at frequencies which were marginal before. However, this change in ITF is not as dramatic as that produced by the ionospheric conditions during the maximum of the solar cycle.

6.1.3 High sunspot activity

The ITFs illustrated for high sunspot activity indicate that during the daytime, the ionosphere will provide adequate shielding from terrestrial interference up to about 17 MHz.

6.2 Discussion

The predicted interference spectra (Figures 6-3, 6-8, 6-13, 6-18, and 6-23) show a general agreement with the overall shape of the spectra measured by WIND, except at the lower frequency edges. This clearly indicates an interference signal model based on international broadcast frequencies can represent the majority of the terrestrial interference encountered for frequencies greater than about 8 MHz. However, the predicted spectra do not fit the minimum frequency of ionospheric breakthrough. We will examine these discrepancies on a case-by-case basis. Also, when studying the WIND spectra, various spectral slopes can be seen in the data. Caution should be exercised in attributing these slopes solely to the transfer functions. Other frequency dependent effects may also contribute to these slopes. The transfer function slope is very shallow for frequencies greater than 8 MHz (for the model ionosphere at sunspot number equal to 10), so any discrepancies between the predicted spectra and measured spectra can not be attributed to the transfer function

The predicted spectrum of the interference over North/South America shows a minimum breakthrough frequency occurring near 6.2 MHz. The actual WIND measurements show the interference to starts slightly above 6 MHz. The location of peaks within the spectrum coincide nicely, with some exceptions. At 8.5, 10.2, and 13-13.5 MHz, the WIND measurements show the presence of signals that do not coincide with any documented broadcast frequencies. The differences in signal amplitudes for the frequencies between 6 to 10 MHz could be reconciled by the fact that actual broadcast powers may differ greatly from those modeled, either through fewer users in each channel or lower transmit powers or some combination of these two. Below 6 MHz, no interference signals were measured for both data sets (Figures 6-4 and 6-5).

Over Western Europe and Africa, the predicted spectrum ends at 8.5 MHz. This is far short of the minimum frequency of 5 MHz in the WIND spectra. For the 11/17/94 WIND spectrum, two small, almost equal amplitude peaks are seen at 5 and 6 MHz. The next peak, at 7.5 MHz, is 3.5 dB higher. The 12/2/94 spectrum is markedly different, although the peaks are at the same frequencies. Here, the 5 MHz peak is at the same amplitude as before. However, the 6, 7.5, and 8.5 MHz peaks all have the same amplitude. The next jump in interference amplitude occurs at 9.75 MHz. The difference in amplitudes between the 5 and 6 MHz interference signals could most likely be explained by the slope of the transfer function. The other jump in signal amplitude, between the 8.5 and 9.75 MHz signals, is too far away from the 'edge' of the transfer function to produce such a noticeable change. This slope is most likely the result of increased broadcast power. The amplitudes of both day's data at 9.75 MHz are similar. The simulated spectrum also failed to predict the signal occurring near 11 MHz for both 11/17/94 and 12/2/94. This frequency is not assigned to any broadcasters, yet the interference is not insignificant. The poor prediction of the lower frequency edge by the model is somewhat the result of the assumptions made during the ITF generation. These will be discussed in detail later.

The measured spectra for the region containing Eastern Europe, Russia, and India also show interference breakthrough at 5 MHz. Surprisingly, some low level of interference also appears to break through at 3.6 MHz in the 11/17/94 data. The only satisfactory explanation for the occurrence of a signal below the daytime critical frequency is that the signal propagates through a part of the ionosphere having a much lower critical frequency. The simulated spectra completely failed to predict the 5 MHz breakthrough. In Figure 6-13, the minimum frequency to reach the spacecraft is about 9.7 MHz. This could be explained by the assumptions made during the ITF generation, as mentioned earlier. Both WIND spectra (in Figures 6-14 and 6-15) appear to have a slope to their spectra between 5 and 7.3 MHz. In the 11/17/94 data set, the intensity of the spectrum increases by 11 dB between 5 and 7.3 MHz. On 12/2/94, the intensity increases by 21 dB over that same frequency range. This is due to the weaker 5 and 6 MHz interference signals. There is a 9 dB difference between the 2 days' data at 5 MHz and 5 dB difference at 6 MHz. The 7.3 MHz signal remains relatively unchanged over this time period. The difference in slope due to the changes in the amplitudes could readily be attributed to changes in transmitter powers, number of users, or the coherency of the combined interference signals. Additional signals occur at higher frequencies (at around 8.5 MHz and 10.5-11.5 MHz) that do not coincide with any known broadcast assignments. The amplitudes are non-negligible, so further study is warranted to determine to source of the interference.

The spectrum for the 11/17/94 WIND data over Asia presents another case where an interference signal at an unexpected frequency occurs. As in the Eastern Europe spectra, the interference breaks through at 3.5 MHz. This signal does not appear in the 12/2/94 data.

However, unlike the Eastern Europe spectra and the 12/2/94 spectrum for Asia, there is no signal present between 5-5.5 MHz. Examining these measured spectra we see that on 11/17/94, between 6 and 7.3 MHz, the amplitude difference is only 3 dB. On 2/2/94, this difference is 6 dB. The differences in slope between the two days' data can easily be attributed either to changes in the number of transmitters operating, or changes in the transmitted power, or both. For the 12/2/94 spectrum, the slope of 8 dB between the 5.5 and 6.0 MHz interference signals is similar to the spectral slope measured in a similar frequency range over Eastern Europe; this is likely due to the ionosphere. Given the large separation between the two regions, it appears unlikely that the 3.4-3.5 MHz interference signals measured in Eastern Europe and Asia come from the same source.

For the spectra measured over the Pacific Ocean, the minimum interference frequency measured is 6 MHz (on 12/2/94). This agrees with the unmodified simulated spectrum shown in Figure 6-22. On 11/17/94, the minimum interference frequency measured by WIND was 7 MHz. For the measured spectra, the amplitude difference between the 7 MHz spike and the 9.5 MHz spike was on the order of 9-10 dB for both data sets. On 12/2/94, the 6 MHz signal was stronger than the 7 MHz signal, producing an amplitude difference of 7 dB between 6 MHz and 9.5 MHz. The predicted spectrum at the spacecraft (in Figure 6-23), shows a minimum interference frequency of 7.5 MHz, missing the 6 MHz minimum measured on 12/2/94. The conditions in the ionosphere could not change enough over the two week period between measurements to produce the > 9 dB increase in attenuation. This can be explained by the ITF generation itself, since the homing tolerance may have excluded rays which could have reached the spacecraft. This is discussed in more detail below. Other interesting features to note is the presence of interference at frequencies not assigned to broadcasters in this region (at 10-11.5 MHz and again at 12-13.5 MHz) for both days' measurements. This may be due to either new frequency assignments or the presence of other types of interference not accounted for in the signal model. One could speculate that these signals are possibly caused by nonlinear ionospheric processes. However, the correlation analysis performed on the data does not support this speculation. Also, because of the frequency stepping arrangement in the receiver, the frequencies of second order nonlinearities fall in between channels in the receiver. (For additional discussion of the nonlinearities and the correlations performed, refer to Chapter 4.)

A number of factors contribute to the discrepancies between the simulated spectra and the measured data. Examining the various assumptions used in the modeling, we should be able to discern the contributing factors:

1) How does the ionosphere affect the predictions?
2) What assumptions in the signal model contribute to the discrepancies?
3) How do the assumptions used in the ITF contribute?

6.2.1 Ionospheric model assumptions

Let us look at the ionospheric conditions first. Sunspot indices retrieved from the National Geophysical Data Center database[1] show that the average sunspot number for the days selected from the WIND data set (November 17 and December 2, 1994) range from 9 to 11. These are fairly low sunspot numbers. The ITFs for the predicted spectra were generated using a sunspot number of 10. Even for nonexistent solar activity, the ionosphere would not sufficiently transparent. Model ionospheres were generated for a sunspot number of 0; the peak plasma frequency at 9:00 AM local time was 8 MHz; when the sunspot number was raised to 10, the overall ionospheric structure experienced very little change and the peak plasma frequency increased to 9 MHz for a very small part of the modeled region (less than

---

[1] Retreivable via the National Oceanic and Atmospheric Administration gopher site at gopher.ngdc.noaa.gov. Search using NGDC Public Data/Solar Terrestrial Physics/Solar Data/Sunspot Numbers.

10%). Ionospheric perturbations were not considered during the modeling. The most likely perturbations that would affect the lower frequencies would be ionospheric bubbles (see Chapter 2), but these only occur at night, when the plasma frequency is already very low. All valid WIND observations were always made during the daytime. The ITFs for all geographic regions were generated for local times corresponding to the WIND subsatellite point local time (9:00 - 10:00 AM). Consequently, the perturbation most likely to affect the data can not be a contributing factor. The raytracing through model ICED ionospheres has been independently verified for both bistatic and transionospheric propagation, so residual imperfections of the ionospheric model itself can not explain the discrepancies between predicted and measured spectra (Argo, et al., 1994; Argo, et al., 1992).

6.2.2 Signal model effects

The signal model is a likely component of the discrepancy, but it can only change the overall power offset, not the lower frequency slope of the spectrum. The part of the signal model that makes this a constant is the way the signals are combined to produce the total interference power. Also, since only broadcast frequencies were modeled, other interference sources that may be present are not included. The signals were combined in a partially coherent manner. We have assumed throughout that the sources combined the same way over the entire spectral range of interest, i.e., either all coherent, or all incoherent, or all partially coherent. The actual combination process may be more complex than that assumed here. The difference between the totally coherent and totally incoherent signal levels as much as 40 dB, where the maximum occurs at the high occupancy channels (refer to Chapter 5 for the discussion on random phasor sums). The difference alone between a incoherent and partially coherent process may account for the discrepancies in the predicted spectra. Table 6-1 compares the signal levels for a realization of a coherent and incoherent process and compares them to two WIND data sets. Five frequencies were selected that contained broadcast signals. The two extremes for the signal combination -- best case (incoherent combination) and worst case (incoherent combination) -- were compared against data from the 11/17/94 and 12/2/94 data sets.

Table 6-1 Simulated spectra compared with WIND data

Freq (MHz)	sim (incoherent)	sim (coherent)	WIND 11/17/94	WIND 12/2/94
5	0	0	1.5	2.5
6	12	57	1.5	6.2
7.5	13	55	5.5	6.2
9.7	13.5	55	11	10.5
12	8.7	45	15	9.0

Note: All spectral components are in log flux density -- dB [W/m^2 Hz] above the Galactic background

6.2.3 Transfer function effects

The ITF is a likely source of the disagreement between the measured and predicted spectra. This can partially be attributed to the generation of the ITF through raytracing. The ITFs created here overestimate the low frequency edge of the transfer function (predicted cutoff frequency > measured cutoff frequency). This is caused by the increased difficulty in homing from the transmitter to the receiver at the lower frequencies. In many cases, the ray will break through, but not be considered a "homed" ray because its positional error exceeds the homing error tolerance. For the ITF generation, the tolerance was set fairly "loosely" to 10 km. The dependence of the spectra on homing tolerance was tested by generating part of an ITF and varying the homing tolerance from 10 km up to 2000 km. The spectra that resulted from increasing the homing tolerance to 2000 km agreed much more closely with the resulted from increasing the homing tolerance to 2000 km agreed much more closely with the WIND data, having a minimum breakthrough frequency of 6 MHz. For ITF studies that must included the dispersive effects on a narrow pulse, the homing error must be set to no more than one wavelength. The 2000 km homing tolerance can be thought of as the diameter of a 'fan' of rays that would reach the spacecraft. For the raypaths contained within this region, the propagation losses are fairly uniform (varying by about ±0.5 dB). At the WIND spacecraft's location of 112,000 km (or greater) from the Earth, this ray fan diameter subtends a 1° (or smaller) arc. The antenna on the spacecraft can be treated as an electrically short monopole above an infinite ground plane (for the sake of simplicity). Its directivity is then similar to that of an electrically short dipole. The directivity has a $\sin^2 \theta$ dependence, where θ is measured with respect to a vertical axis through the spacecraft. There is no ϕ dependence in the directivity (if there were, spin-stabilization of WIND could be seen in the measurements). The spacecraft lies in the ecliptic plane, with its vertical axis pointing at the North pole of the ecliptic plane. The directivity peak occurs at $\theta = 90°$, so that the peak of the pattern is oriented toward the Earth. The angle subtended by the homing tolerance diameter (1° or less) is small enough that it lies within the peak of the receive antenna pattern.

Another factor to consider in interpreting the simulated spectra is that the WIND subsatellite point was always within a 9:00 - 10:00 AM local time, but the hemisphere as viewed by WIND included a part of the day/night terminator. On the nightside of this terminator, the ionospheric peak plasma frequency was at its lowest value (typically 1-2 MHz) for the diurnal cycle. The leakage of signals through this day/night boundary is a complex phenomenon, and it may contribute to some of the interference detected by the RAD2 at frequencies lower than 5 - 6 MHz. This particular phenomenon may be especially applicable in explaining the existence of the 3.4-3.5 MHz signals when the spacecraft was over Eastern Europe and Asia (see Figures 6-14 and 6-19). For a broader view of these signals, refer to Figure 4-3, where the diffuse "blur" at frequencies less than 5 MHz correspond to these signals.

A simulated spectrum created using the revised homing tolerance is illustrated in Figure 6-26. Its minimum breakthrough frequency, as mentioned earlier, is 6 MHz.

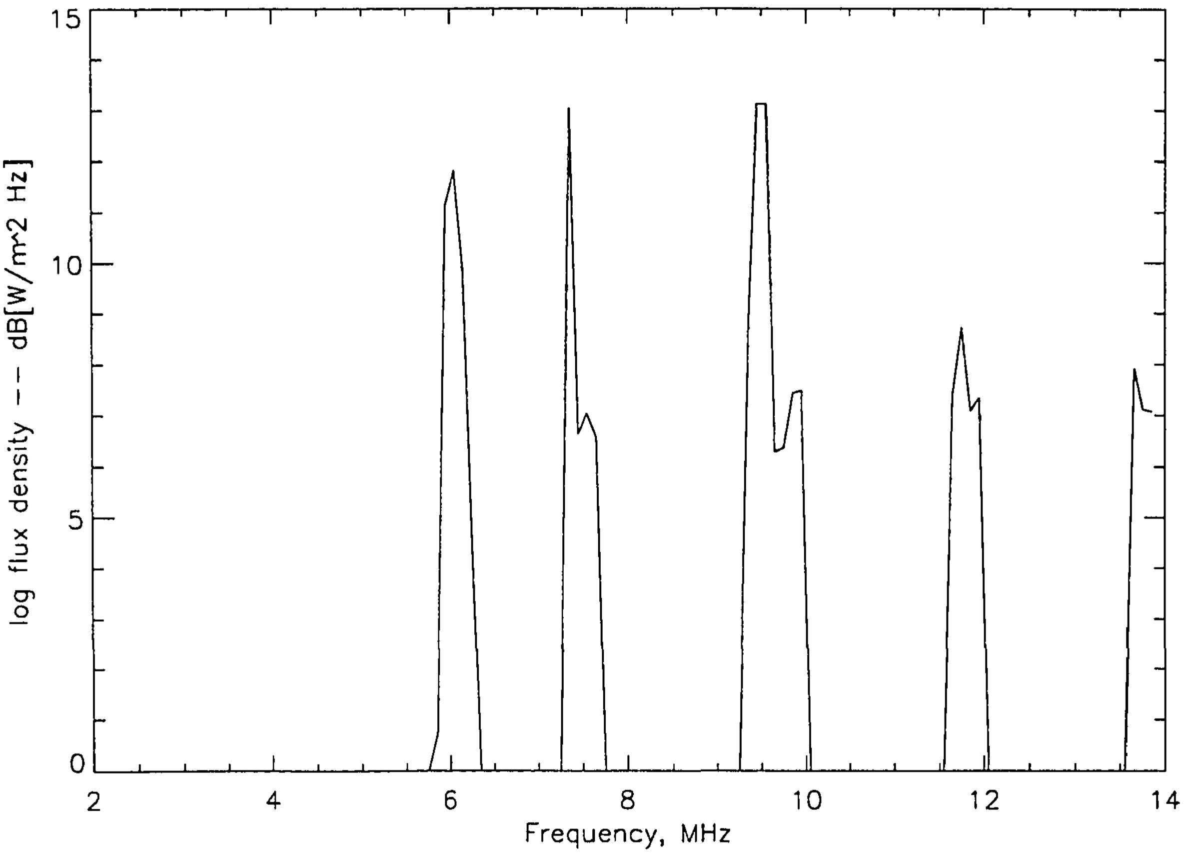

Figure 6-26 Revised interference spectrum for Western Europe and Africa.

Finally, residual discrepancies may be due to the following effects:

- modeling of the receive antenna as a monopole above ground;
- actual transmitter powers differing from the signal model;
- the slope of the transfer function with respect to sunspot number.

By modeling the receive antenna as a simple monopole above an infinite ground plane, instead of the monopole above a small ground plane that it really is, the frequency dependence of the actual effective aperture has been simplified. Since the ground plane of the antenna on WIND is of a finite size, as the frequency decreases, the ground plane becomes smaller with respect to the radio wavelength. This has the effect of decreasing the gain of the antenna. The discrepancy in spectral slope could easily be accounted for by changes in the actual transmitted power at each broadcast frequency. Changes in the coherency assumption, i.e., going from a partially coherent interference combining process to a totally incoherent combining process will drop the total interference power by 3 to 10 dB. In the signal model, no assumptions were made as to specific broadcast schedules for the individual interferers, so it is quite possible that the total interference power can differ from that modeled here. Also, as discussed earlier, the ICED ionospheric model has been too thoroughly tested that any errors in it could explain the gross differences in spectral slope. However, since no ionospheric model can ever exactly reproduce the ionosphere for a particular day, it is possible that some of the residual differences can be attributed to the departure of the model from the ionosphere as it was for the two days' measurements. The transfer function slope (with respect to sunspot number) is sufficiently flat for the transmitter-receiver geometry used in the interference spectra prediction so as not to be an issue.

The WIND receiver calibrations were also assumed to be sufficiently accurate that it can not account for the residual discrepancies between the measured data and simulations.

CHAPTER 7
SUMMARY AND CONCLUSIONS

In the material presented, we have seen that HF waves propagating through the ionosphere can undergo significant refraction and absorption. Signals incident at receivers separated by more than the correlation distance of the ionosphere (which covers a two order of magnitude range of tens of meters to kilometers) will not be correlated. This presents severe difficulties to ground-based HF interferometry. On the other hand, space-based HF interferometry encounters a different set of difficulties. In addition to a more complex calibration procedure, the space-based interferometer is subject to interference from terrestrial radio sources. The limits of harmful interference levels have been set by the CCIR to 10% of the system noise level of a receiving system. Harmful interference limits have been calculated, given proposed HF interferometer system parameters, to be on the order of 10 to 20 dB greater than the Galactic background radiation.

Past measurements of the HF terrestrial interference have indicated that the intensity of the interference has a strong geographical dependence. The RAE-1, DMSP, and AMPTE satellites have found that the noise peaks over populated areas. Eastern Europe and Asia were found to have significantly high levels of interference across the limited set of frequencies sampled by these experiments. The AMPTE spacecraft had a sufficiently high temporal resolution to determine that the interference had distinctive rise and fall times. The signals detected over Europe looked very much like broadcast transmissions. There was a strong local time dependence to the interference behavior as well. It was noted that very little interference was detected near local noon, when the ionosphere is most opaque. While the RAE, DMSP, and AMPTE measurements have highlighted the problem of terrestrial interference in space, the data itself is limited by the age, lack of accessibility, and limited spectral coverage.

In late October, 1994, a spacecraft was launched to study the characteristics of the Solar wind. This spacecraft, WIND, had an HF receiver on board. Prior to the spacecraft's moving to a point between the Earth and Sun, it completed a number of highly elliptical orbits around the Earth. During these orbits, the HF receiver was set to scan between 1.075 and 13.875 MHz in 256 steps. Significant measurements of the terrestrial interference were made over a three week period, when the sunspot number was low and the ionosphere relatively transparent. The data collected by WIND indicate that commercial broadcast transmissions are the most intense component of the interference in space. 18 second samples clearly show sharp rise and fall times, similar to those detected by the AMPTE receiver. Individual signals also appear to follow a set transmission schedule, since many emissions turn on and off at half-hour increments. The worst case flux densities are 30 to 40 dB above the Galactic background at a distance of 20 Earth radii. This implies that for an interferometer in orbit at an altitude of 40,000 km, the flux densities would be as high as 40 to 55 dB above the Galactic background. The exceptional spectral resolution of the HF receiver on board WIND made possible a search for quiet channels among the interference. A study of the data set has shown that, for the desired interferometer observation frequencies, both 1.4 and 4.4 MHz may be sufficiently quiet to perform high resolution interferometry from Earth-orbit. No information is currently available on the highest frequency of interest (25.5 MHz) for the Earth-orbiting interferometer. Additionally, the WIND data has pointed out the need to perform observations only while the interferometer on the Earth's day side. The night time ionosphere is so transparent that interference levels would "blind" the interferometer.

Given the knowledge now available on terrestrial interference, it is important to be able to predict how and when the ionosphere can shield an Earth-orbiting interferometer from terrestrial interference. The model of terrestrial interference presented here was based on a modified form of the Friis transmission formula. There are two significant components -- the interference power as a function of frequency and the ionospheric transfer function as a function of frequency and transmitter-satellite geometry.

The model of the interference power is a first generation model of the overall interference spectrum. The WIND data indicate that broadcast transmissions are the primary component of the detected signals. In accordance with this discovery, the model components have been limited to the frequencies occupied by broadcasters. The spectrum was discretized and a database compiled with information on the interference at each frequency step. If the frequency was occupied by a broadcaster, information on the type of transmissions (low or high power) and an estimate of the number of users was recorded. The interference signal at each step was found by a partially coherent summation of the individual interferers. The signal ranges for completely incoherent to totally coherent transmission were also found. In going from totally incoherent signal combination to totally coherent signal combinations, the overall shape of the spectra did not change. Only the absolute magnitudes between the two coherence extremes changed. The location dependence of the interference was handled by developing five different spectra, divided into geographical classes. This approach is supported by the interference measurements themselves. The RAE-1, DMSP, and WIND data show that the interference has a geographical component.

The ionospheric transfer function determines whether the interference signals from a particular transmitter-receiver geometry will reach the receiver. This transfer function is highly dependent on the state of the ionosphere. The behavior of the ionosphere itself is highly dependent on the sunspot number, local time, time of year, geographic location, and the geomagnetic field. The model of the ionosphere used in the transfer function development is currently one of the most sophisticated models available. It has been combined with a threedimension raytracing program to calculate the transfer functions for various transmitter-receiver combinations.

Raytracing has been used for many years in studying ionospheric propagation. It was proven to be the most numerically efficient approach to developing an ionospheric transfer function as well. The scale of this simulation was such that full wave methods proved to be infeasible (see Appendix B for a discussion of the numerical difficulties).

The numerical raytracing simulations have shown that the 'visibility' of the interference source is highly dependent on a number of factors. The dual conditions of the general state of the ionosphere and the transmitting frequency are very important in determining whether a ray will reach the receiver. Simulations for low (10), medium (60), and high sunspot (170) number conditions show that the transfer function is sensitive to gross changes in the state of the ionosphere. Smaller variations (< 10) in sunspot number produced no discernible changes in the transfer function. The minimum breakthrough frequency was at about 6.5 MHz for the low sunspot number case. As the sunspot number was increased, the minimum breakthrough frequency increased as well, to 17 MHz when the sunspot number was set to 170.

For any given model ionosphere generated, the transfer function proved to be very sensitive to frequency and transmitter-receiver geometry at the lower frequencies and larger separations. At any given sunspot number, local time, and transmitter-receiver separation, the total propagation loss would increase sharply (up to 11 dB over a span of 3 MHz) as the ray frequency approached the minimum breakthrough frequency from above. Below this minimum breakthrough frequency, the ray could not penetrate the ionosphere. The gross changes in the sunspot number increased both the absorption and the minimum breakthrough frequency for each longitudinal step in the transmitter-receiver geometry. Also, with higher sunspot numbers, the slope of the minimum breakthrough frequency with respect to transmitter-receiver longitudinal separation increased by greater than 30%. The change in the slope was especially noticeable between the medium and high sunspot transfer functions. (This is not applicable to the measured data used here.)

Some discrepancies were found when the simulated spectra were compared to the data measured by the HF receiver on WIND. For most of the different spectra simulated, the minimum frequency of the predicted breakthrough was higher than the actual minimum frequency measured by WIND by as much as 5 MHz. Several factors could cause this discrepancy, two of which appear to be the most likely source for the discrepancy. First, the actual interference power may differ from the predicted interference power of the signal model by greater than 15 dB. Second, a more generous homing tolerance (2000 km) drops the minimum 'homed' frequency down to about 6 MHz for a low sunspot ionosphere (which is applicable to the measured data used in the research). It is also important to bear in mind that the during the WIND observations, a small part of the Earth's night side was visible. Since the ionosphere is much more tenuous at the predawn hours (with typical critical frequencies near 1 to 2 MHz), some interference from these regions can propagate out to the spacecraft. The day-night terminator is a complex region to simulate, with very high electron density gradients over short longitudinal distances. This effect was not accounted for during the ITF generation.

In conclusion, this research has developed a first generation approach to describing the HF interference at satellite heights. The predictive aspect of the model is in its ability to generate case studies of different ionospheric conditions and examine the resulting interference spectra. At frequencies greater than about 8 MHz, it appears to have a generally good agreement with the WIND data. Below 8 MHz, the model is increasing sensitive to the assumptions used in generating the transfer function. Care should be exercised when applying these results at the lower frequency bounds.

This research has shown that:

- many of the frequency channels containing interference correspond to broadcast frequencies;
- at the higher end of the spectrum, the predicted signal amplitudes are within 15 dB of the measured signal amplitudes;
- in the frequency range of 5-7 MHz, the model closely predicted the low frequency cutoff when the homing tolerance was increased to 2000 km;
- except for the 3.4 MHz anomaly, the predicted cutoff frequency occurred below 5 MHz.

The results presented here can also be treated as a tutorial (or guide) on how to determine the impact of HF interference for future HF interferometer planning. One could use the following procedure to create the relevant interference model:

1) start with an updated version of the signal model described in Chapter 5 -- this model can be updated by referring to the most recent *World Radio and TV Handbook*;
2) generate the ITFs using three-dimensional raytracing for the various subsatellite points, local times, and sunspot numbers under consideration;
3) generate the interference spectra using the basic equations in Chapters 5 and 6;
4) apply the necessary corrections for antenna pattern and receiver bandwidth.

CHAPTER 8
FUTURE WORK

The interference environment in near-Earth space has been discussed in the previous chapters. Data gathered by the WIND spacecraft and others support the contention that the regions within 100 R_E are a hostile radio environment for sensitive, high resolution radio astronomy in the HF bands, at least for frequencies above the ionospheric cutoff.

The analysis presented is an initial attempt to quantify and predict the extent of the man-made component of the radio interference. A number of assumptions have been introduced to simplify the analysis and provide a starting point. Several areas will need to be addressed to continue developing the work presented here:

1. Improved interference data collection.

All of the measurements presented here have been limited by an upper frequency less than 15 MHz. A sizable portion of the shortwave broadcasters also transmit at frequencies up to 26 MHz, although none are adjacent to the 25.55 - 25.67 MHz band, the frequency allocation for radio astronomy.

The need for a comprehensive database of interference data has been addressed by others (Calvert, et al., 1994). Significant progress could be made in filling the gaps of knowledge by developing and orbiting a low cost, scanning receiver to make precise measurements of the radio interference at frequencies above 14 MHz. It is especially important to collect data on the occupancy and interference levels found in the protected bands. Additonal interference data will be collected by the WIND spacecraft when it makes additional Earth passes in August, 1995. We can expect the new data to extend the knowledge already gained from the data collected.

2. Ground truth data collection.

Sufficient work remains to be done on the analysis of WIND data that it could constitute a dissertation itself. It should be possible to combine "ground truth" measurements from ionosondes and other ionospheric measuring devices to develop a more complete picture of the ionospheric environment. In combination with "ground truth" measurements, a more thorough analysis of WIND data may reveal new information on the ionosphere.

3. New data analysis techniques.

An improved analysis of the data would be possible using new signal processing techniques, such as Hilbert techniques (Long, et al., 1995). The MATLAB analysis developed by Long and colleagues at the NASA Goddard Space Flight Center has been applied to water waves. The MATLAB code is available from Long, but it would be necessary to adapt this approach to the IDL programming environment used by the rest of the WIND investigators.

4. Improved ionospheric modeling:

The ionospheric model used in the ray-tracing part of the analysis, ICED, is no longer the most complete model available. Future development efforts should include an interface to PRISM, the latest ionospheric model to be released by the Air Weather Service. Along similar lines, a more sophisticated perturbation model could be developed by using the WBMOD irregularity model developed by NorthWest Research Associates (Secan and Bussey, 1994). This irregularity model was developed for use by the Air Force[1].

5. Improved interference source modeling.

The interference source modeling could be strengthened by incorprating data collected from a ground-based measurement campaign. A simple, low-cost receiver similar to the one mentioned in item (1) could be set up to automatically collect channel occupancy data with

---

[1] Dr. Santimay Basu, of the Phillibs Lab (Geophyscial Directorate) at Hanscom Air Force Base in Massachusetts, is the point of contact for permission to use WBMOD.

respect to time and frequency. Alternatively, the Rockwell Collins 95S-1 receiver described by Calvert (Calvert, et al., 1994) would be an ideal instrument for such an endeavor. This data could be used to complement both the WIND findings and future space-based measurements.

Finally, as this research has shown, the interference environment in space is hostile to the mission of an orbiting interferometer. Yet, a number of relatively quiet frequencies appear to be available where the interference is on the order of the galactic background radiation. Ground- and space-based measurements could be used to develop a database of spectrum occupancy. Such a database would fill in the many gaps in our knowledge of the terrestrial interference.

High sensitivity interferometry from earth orbit may be possible if the orbit parameters are such that the array always remains on the sunlit side of the Earth, thus using the ionosphere for shielding. This conclusion has been put forward by Erickson (1988); the data and simulations support this conclusion. An orbit that allows the array to stay in the Pacific region would also minimize the impact of terrestrial interference. At this point, the data collected is insufficient to rule out the possibility of observations from Earth-orbit. The WIND data does indicate that the "quiet" (i.e., protected) channels are not necessarily so. However, a search through the datasets has uncovered some frequencies which appear to be relatively free of terrestrial interference.

Other interference sources, such as broadband man-made and atmospheric noise have not been included in this first generation model. These sources may be nontrivial, so future observations and modeling attempts should endeavor to quantify the contributions of these sources to the overall interference environment.

REFERENCES

Afraimovich, E. L., G. A. Zherebtsov, V. N. Zvezdin, S. J. Franke, "Characteristics of small-scale ionospheric irregularities as deduced from scintillation observations of radio signals from satellites ETS-2 and Polar Bear 4 at Irkutsk", *Radio Science*, Vol. 29, No. 4, p. 830, 1994

Alexander, J. K., M. L. Kaiser, J. C. Novako, F. R. Grena, R. R. Weber, "Scientific instrumentation of the RAE-2", *Astronomy and Astrophysics*, Vol. 40, p. 365, 1975

Argo, P. E., D. DeLapp, C. D. Sutherland, R. G. Farrer, *TRACKER: A Three-Dimensional Raytracing Program for Ionospheric Radio Propagation [Technical Manual]*, Space and Atmospheric Sciences Group, Los Alamos National Laboratory, 1994

Argo, P. E. , T. J. Fitzgerald, R. Carlos, "NICARE I HF propagation experiment results and interpretation", *Radio Science*, Vol. 27, No. 2, p. 289, 1992

Balanis, C. A., *Advanced Engineering Electromagnetics*, John Wiley & Sons, New York, 1989

Basart, J. P.,S. A. Mandayam, J. O. Burns, "An inflatable antenna for space-based low frequency radio astronomy", *Proceedings of SPACE '94: Engineering, Construction, and Operations in Space IV*, eds. R. G. Galloway and S. Lokay, American Society of Civil Engineers, Albuquerque, NM, 1994

Basart, J. P., "The Boulder-Ames decameter wavelength VLBI experiment", *Proceedings on a Lunar Far-Side Very Low Frequency Array*, NASA Pub. 3039, p. 19, Wash., DC, 1988.

Basler, R. P., G. H. Price, R. T. Tsunoda, T. L. Wong, "Ionospheric distortion of HF signals", *Radio Science*, Vol. 23, No. 4, p. 569, 1988

Basu, Sa., Su. Basu, "Ionospheric structures and scintillation spectra", *Proceeding of the Conference on Wave Propagation in Random Media (Scintillation)*, eds. V. I. Tatarskii, A. Ishimaru, V. U. Zavotny, SPIE, Bellingham, WA, 1993

Beckmann, P., *Probability in Communication Engineering*, Harcourt, Brace, and World, New York, NY, 1967

Bilitza, D., "Solar-terrestrial models and software", *Planetary and Space Science*, Vol. 40, No. 4, p. 541, 1992

Bourgeret, J.-L., M. L. Kaiser, P. J. Kellogg, R. Manning, K. Goetz, S. J. Monson, N. Monge, L. Friel, C. A. Meetre, C. Perche, L. Sitruk, "WAVES: The radio and plasma wave investigation on board the WIND spacecraft", to appear in *Space Science Reviews*, Kluwer, Belgium, 1995

Brown, L. D., R. E. Daniell, M. W. Fox, J. A. Klobuchar, P. H. Doherty, "Evaluation of six ionospheric models as predictors of Total Electron Content", *Radio Science*, Vol. 26, No. 4, p. 1007, 1991

Budden, K. G., *The Propagation of Radio Waves*, Cambridge University Press, UK, 1985.

Calvert, W., W. J. Byrd, J. P. Basart, J. D. Iversen, A. L. Baker, W. S. Kurth, D. Tsintikidis (investigators), *Iowa Orbiting Wave Analyzer: A Proposed Satellite Investigation to Characterize the Radio Environment of the Earth*, Proposal in response to USRA Announcement of Opportunity No. USRA 1-94, Iowa Space Grant Consortium, Ames, IA, 1994

Carr, T. D., L. Wang, "Monitoring Jupiter's hectometric radiation", *Low Frequency Astrophysics from Space*, N. E. Kassim, K. W. Weiler, eds., Lecture Notes in Physics Vol. 362, Springer Verlag, New York , 1990.

Chatfield, C., *The Analysis of Time Series, An Introduction*, Chapman & Hall, New York, 1989

Daniell, R. E., Decker, D. T. , D. N. Anderson, J. R. Jasperse, J. J. Sojka, R. W. Schunk, "A global Ionospheric Conductivity and Electron Density (ICED) Model", *International Beacon Satellite Symposium Proceedings*, Cambridge, MA, 1992

Decker, R. A., C. E. Valladeres, Su. Basu, D. N. Anderson, R. A. Heelis, "Modeling daytime F layer patches over Söndrestorm", *Radio Science*, Vol. 29, No. 1, p. 249, 1994

Desch, Michael, "A quantitative assessment of RFI in the near-Earth environment", *Low Frequency Astrophysics from Space*, N. E. Kassim, K. W. Weiler, eds., Lecture Notes in Physics Vol. 362, Springer Verlag, New York , 1990

Dulk, G. A., "Solar radio astronomy at low frequencies", *Low Frequency Astrophysics from Space*, N. E. Kassim, K. W. Weiler, eds., Lecture Notes in Physics Vol. 362, Springer Verlag, New York , 1990

Dutta, S., G. F. Gott, "HF spectrum usage", *Second International Conference on HF Communication Systems and Techniques*, IEE, Savoy Place, London, UK, 1982

Erickson, W. C., *Radio Interference in the Near-Earth Environment*, NASA JPL Publication 88-30, 1988

Fejer, B. G., M. C. Kelley, "Ionospheric irregularities", *Reviews of Geophysics and Space Physics*, Vol. 18, No. 2, pp. 401-454, 1980

Fremouw, E. J., R. L. Leadabrand, R. C. Livingston, M. D. Cousins, C. L. Rino, B. C. Fair, R. A. Long, "Early results of the DNA Wideband satellite experiment -- complex-signal scintillation", *Radio Science*, Vol. 13, No. 1, p. 167, 1978

Gibson, A. J. , L. Arnett, "Measurements and statistical modeling of spectrum occupancy", *Sixth International Conference on HF Radio Systems and Techniques*, IEE, Edinburgh, Scotland, 1994

Goodman, J. M., *HF Communications: Science and Technology*, Van Nostrand Reinhold, New York, 1992

Gott, G. F. , S. K. Chan, C. Pantjiaros, J. Brown, M. Bröms, S. Boberg, "Recent work on the measurement and analysis of spectral occupancy at HF", *Sixth International Conference on HF Radio Systems and Techniques*, IEE, Edinburgh, Scotland, 1994

Goutelard, C., J. Caratori, "Time modeling of HF interferences", *Fifth International Conference on HF Radio Systems and Techniques*, IEE, Edinburgh, Scotland, 1991

Gurevich, A. V., *Nonlinear Phenomena in the Ionosphere*, Springer-Verlag, New York, 1978

Ha, T. T., *Solid-State Microwave Amplifier Design*, John Wiley and Sons, New York, 1981

Hall, H. M., "A new model of 'impulsive' phenomena: application to atmospheric noise communications channels", Electronics Laboratory Technical Report 3412-8, Stanford University, Palo Alto, CA, August, 1966

Haselgrove, J. "Ray theory and a new method of ray tracing", *The Physics of the Ionosphere*, p. 355, Phys. Soc., London, UK, 1954

Haselgrove, J., "The Hamiltonian ray paths", *Journal of Atmospheric and Terrestrial Physics*, Vol. 25, p. 397, 1963

Häusler, B., R. R. Anderson, D. A. Gurnett, H. C. Koons, R. H. Holzworth, O. H. Bauer, R. Treumann, K. Gnaiger, D. Odem, W. B. Harbridge, F. Eberl, "The plasma wave instrument on board the AMPTE IRM satellite", *IEEE Transactions of Geoscience and Remote Sensing*, Vol. GE-23, No. 3, p. 267, 1985

Herman, J. R., J. A. Caruso, R. G. Stone, "Radio Astronomy Explorer (RAE) - I. observations of the terrestrial radio noise", *Planetary and Space Science*, Vol. 21, p. 443, 1973

Herman, J. R., R. G. Stone, J. A. Caruso, "Radio detection of thunderstorm activity with an Earth-orbiting satellite", *Journal of Geophysical Research*, Vol. 80, No. 4, p. 665, 1975

Hinkel-Lipsker, D. E., M. M. Shoucri, T. M. Smith, T. M. Wagner, J. D. Hansen, G. J. Morales, "Modeling of High-Frequency oblique propagation and heating in the ionosphere", *Radio Science*, Vol. 28, No. 5, p. 819, 1993

Ishimaru, A., *Wave Propagation and Scattering in Random Media, Volume 2: Multiple Scattering, Turbulence, Rough Surfaces, and Remote Sensing*, Academic Press, New York, 1978

Jacobson, A. R., W. C. Erickson, "Wavenumber-resolved observations of ionospheric waves using the Very Large Array radiotelescope", *Planetary and Space Science*, Vol. 40, p. 447, 1992a

Jacobson, A. R., W. C. Erickson, "A method for characterizing transient ionospheric disturbances using a large radiotelescope array", *Astronomy & Astrophysics*, Vol. 257, p. 401, 1992b

James, H. G., "High frequency ducting in the high-latitude bottomside F region", *Radio Science*, Vol. 30, No. 2, p. 445, 1995

Jones, R. M. and J. J. Stephenson, *A Versatile Three-Dimensional Ray-Tracing Computer Program for Radio waves in the Ionosphere*, OT Report 75-76, October 1975

Kaiser, M. L., "Reflections on the Radio Astronomy Explorer program of the 1960s and 1970s", *Low Frequency Astrophysics from Space*, N. E. Kassim & K. W. Weiler, eds., Springer Verlag Lecture Notes in Physics, Vol. 362, New York, 1990

Kassim, N. E., R. A. Perley, W. C. Erickson, K. S. Dwarakanath, "Subarcminute resolution imaging of radio sources at 74 MHz with the Very Large Array", *The Astronomical Journal*, Vol. 106, No. 6, p. 2218, 1993

Kelley, M. C., *The Earth's Ionosphere, Plasma Physics and Electrodynamics*, Academic Press, New York, 1989

Kelso, J. M., *Radio Ray Propagation in the Ionosphere*, McGraw-Hill, New York, 1964

Kelso, J. M., "Ray tracing in the ionosphere", *Radio Science*, Vol. 3, No. 1, p. 1, 1968

Knepp, D. L., "Analytic solution for the two-frequency mutual coherence function for spherical wave propagation", *Radio Science*, Vol. 18, No. 4, p. 535, 1983

Knepp, D. L., "Aperture antenna effects after propagating through strongly disturbed random media", *IEEE Transactions on Antennas & Propagation*, Vol. AP-33, No. 10, p. 1074, 1985

LaBelle, J., R. A. Treumann, M. H. Boehm, K. Gewecke, "Natural and man-made emissions at 1.0-5.6 MHz measured between 10 and 18 R_E", *Radio Science*, Vol. 24, No. 6, p. 725, 1989

Laycock, P. J., M. Morrell, G. F. Gott, A. R. Ray, "A model for HF spectral occupancy", *Fourth International Conference on HF Radio Systems and Techniques*, IEE, Edinburgh, Scotland, 1988

Lemmon, J. J. , "Wideband noise and interference modeling", *Proceedings of the IEEE Military Communications Conference (MILCOM '89)*, Boston, MA, 1989

Lemmon, J. J., "Model for the simulation of wide band HF noise and interference", *Fifth International Conference on HF Radio Systems and Techniques*, IEE, Edinburgh, Scotland, 1991

Lin, J.-C., Y.-W. Kiang, "High-frequency beam wave propagation in a stratified random ionosphere", *Radio Science*, Vol. 23, No. 4, p. 685, 1988

Liu, C.-H., "Pulse statistics in random media", *Proceeding of the Conference on Wave Propagation in Random Media (Scintillation)*, eds. V. I. Tatarskii, A. Ishimaru, V. U. Zavotny, SPIE, Bellingham, WA, 1993

Lott, G. K., W. R. Vincent, S. Juaregui, "HF signal amplitude distributions and total spectrum power measurements", *Sixth International Conference on HF Radio Systems and Techniques*, IEE, Edinburgh, Scotland, 1994

Long, S. R., N. E. Huang, C.-C. Tung, M.-L. Wu, R.-Q. Lin, E. Mollo-Christenson, Y. Yuan, "The Hilbert techniques: an alternate approach for non-steady time series analysis", *IEEE Geoscience and Remote Sensing Society Newsletter*, No. 94, p. 18, 1995

MacDougall, J. W. , "Length measurements of mid-latitude scintillation irregularities", *Radio Science*, Vol. 27, No. 2, p. 275, 1992

Massey, R. S., "Impulse response function for a transionospheric signal through a gaussian filter", *Radio Science*, Vol. 28, No. 4, p. 643, 1993

McNamara, L. F., *The Ionosphere: Communications, Surveillance, and Direction Finding*; Orbit, Malabar, FL, 1991.

Moulsley, T. J., "HF data transmission in the presence of interference", *Third International Conference on HF Radio Systems and Techniques*, IEE, Edinburgh, Scotland, 1985

Nickisch, L. J., P. M. Franke, "Finite difference-time domain tests of random media propagation theory", *Proceedings of the Ninth Annual Review of Progress in Applied Computational Electromagnetics*, ACES, Monterey, CA, 1993

Nickisch, L. J., "Non-uniform motion and extended media effects on the mutual coherence function: an analytic solution for spaced-frequency, position, and time", *Radio Science*, Vol. 27, No. 1, p. 9, 1992

Nickisch, L. J., "Propagation effects in extended random media", *International Beacon Satellite Symposium Proceedings*, Boston, MA, 1992

Nickisch, L. J., "Focusing in the stationary phase approximation", *Radio Science*, Vol. 23, No. 3, p. 171, 1988

Novaco, J. C. , L. W. Brown, "Nonthermal Galactic emission below 10 MHz", *Astrophysical Journal*, Vol. 221, p. 114, 1978

Perry, B. D., L. G. Abraham, " A Wideband HF interference and noise model based on measured data", *Fourth International Conference on HF Radio Systems and Techniques*, IEE, Edinburgh, Scotland, 1988

Rawer, K. and W. R. Piggott, eds., *Development of IRI-90, Advances in Space Research*, Vol. 10, No. 11, Pergamon Press, New York, 1990

Richmond, A. D., M. Blanc, B. A. Emery, R. H. Wand, B. G. Fejer, R. F. Woodman, S. Ganguly, P. Amayenc, R. A. Behnke, C. Calderon, J. V. Evans, "An empirical model of quiet-day ionospheric electric fields at middle and low latitudes", *Journal of Geophysical Research*, Vol. 85, No. A9, p. 4658, 1980

Rino, C. L., "A power law phase screen model for ionospheric scintillation: 1. Weak scatter", *Radio Science*, Vol. 14, No. 6, p. 1135, 1979

Rino, C. L., "A power law phase screen model for ionospheric scintillation: 2. strong scatter", *Radio Science*, Vol. 14, No. 6, p. 1147, 1979

Rino, C. L., J. Owen, "Numerical simulations of intensity scintillation using the power law phase screen model ", *Radio Science*, Vol. 19, No. 3, p. 891, 1984

Roussel-Dupré, R., "Propagation and energy transfer", Chapter 7, *Introduction to Ultra-Wideband Systems*, ed. J. D. Taylor, CRC Press, Boca Raton, FL, 1995

Roussel-Dupré, R., P. E. Argo, "Deterministic transfer function for transionspheric propagation", *International Beacon Satellite Symposium Proceedings*, Boston, MA, 1992

Rush, C. M., J. Buchau, "Determining the F-region critical frequency from satellite-borne noise measurements", *Journal of Atmospheric and Terrestrial Physics*, Vol. 39, p. 277, 1977

Rush, C. M., A. L. Snyder, E. Ziemba, "HF noise in space", *Ionospheric Effects Symposium Proceedings*, Wash., D.C., 1978

Rush, C. M., A. L. Snyder, E. Ziemba, V. Patterson, T. Tascione, D. Nelson, "Satellite measurements of the HF radio noise environment in the topside ionosphere", *Radio Science*, Vol. 15, No. 6, p. 1127, 1980

Rush, C. M., "Ionospheric radio propagation models and prediction: A mini-review", *IEEE Transactions on Antennas & Propagation*, Vol. AP-34, No. 9, p. 1163, 1986

Rush, C. M. , J. S. Washburn, L. A. Berry, "A High-Frequency spectrum utilization model", *Radio Science*, Vol. 23, No. 3, p. 233, 1988

Secan, J. A. , R. M. Bussey, *An Improved Model of High-Latitude F-region Scintillation (WBMOD Version 13)*, NorthWest Research Associates Report NWRA-CR-94-R120, August, 1994

Sennitt, A. G. (editor), *World Radio TV Handbook, 1994 Edition*, Billboard Books, Amsterdam, The Netherlands, 1994

Soicher, H., "Traveling ionospheric disturbances (TIDs) at mid-latitudes: solar cycle phase dependence", *Radio Science*, Vol. 23, No. 3, p. 283, 1988

Spaulding, A. D., G. H. Hagn, "Worldwide minimum environmental radio noise levels (0.1 Hz to 100 GHz)", *Ionospheric Effects Symposium Proceedings*, J. M. Goodman, ed., Arlington, VA.,1978

Tascione, T., *Introduction to the Space Environment*, Second Edition, Krieger Publishing, Malabar, FL, 1994

Thompson, A. R., "The response of a radio-astronomy synthesis array to interfering signals", *IEEE Transactions on Antennas & Propagation*, Vol. AP-30, No. 3, p. 450, 1982

Tsunoda, R. T., "Magnetic-field-aligned characteristics of plasma bubbles in the nighttime equatorial ionosphere", *Journal of Atmospheric and Terrestrial Physics*, V42, p. 743, 1980

Tsunoda, R. T., R. C. Livingston, J. P. McClure, W. B. Hanson, "Equatorial plasma bubbles: vertically elongated wedges from the bottomside F layer", *Journal of Geophysical Research*, Vol. 87, No. A11, p. 9171, 1982

Tsunoda, R. T., S. Fukao, M. Yamamoto, "On the origin of quasi-periodic radar backscatter from mid-latitude sporadic E", *Radio Science*, Vol. 29, No. 1, p. 349, 1994

Vincent, W. R., G. K. Lott, "Measurements of extensive HF Industrial, Scientific, and Medical (ISM) interference far removed from the ITU allocated bands", *Sixth International Conference on HF Radio Systems and Techniques*, IEE, Edinburgh, Scotland, 1994

Ward, B. D., M. G. Golley, "Solar cycle variations in atmospheric noise at HF", *Fifth International Conference on HF Radio Systems and Techniques*, IEE, Edinburgh, Scotland, 1991

Weber, R. R., J. K. Alexander, R. G. Stone, "The Radio Astronomy Explorer satellite, a low-frequency observatory", *Radio Science*, Vol. 6, No. 12, p. 1085, 1971

Weiler, . W., B. K. Dennison, K. J. Johnston, R. S. Simon, W. C. Erickson, M. L. Kaiser, H. V. Cane, M. D. Desch, L. M. Hammarstrom, "A low frequency radio array for space", *Astronomy & Astrophysics*, Vol. 195, p. 372, 1988

Weiler, K. W., "Low frequency astrophysics with a space array", *Low Frequency Astrophysics from Space*, N. E. Kassim, K. W. Weiler, eds., Lecture Notes in Physics Vol. 362, Springer Verlag, New York , 1990.

Weiler, K. W., N. Kassim, A. Clegg, R. Foster, C. Lichtenberg, J. Spencer, J. O. Burns, J. P. Basart, N. Duric, J. Canaris, B. Dennison, G. Dulk, R. Perley, D. Frail, R. G. Stone, M. D. Desch, M. L. Kaiser, W. M. Farrell, R. Allen, Dwarakanath, A. Rogers, W. C. Erickson (investigators), *A Low Frequency Space Array: A Concept for Low Frequency Astrophysics from Space*, Proposal in response to NASA NRA OSS-15, December 7, 1994

Wilkinson, R. G., "A statistical analysis of HF radio interference and its application to communications systems", *Second International Conference on HF Communication Systems and Techniques*, IEE, Savoy Place, London, UK, 1982

Yamamoto, M., N. Komoda, S. Fukao, R. T. Tsunoda, T. Ogawa, T. Tsuda, "Spatial structure of E region field-aligned irregularities by MU radar", *Radio Science*, Vol. 29, No. 1, p. 337, 1994

Yeh, K. C., C. H. Liu, "An investigation of temporal moments of stochastic waves", *Radio Science*, Vol. 12, No. 5, p. 671, 1977

APPENDIX A

IDL ANALYSIS ROUTINES

A.1 Spectrogram program listing

```
***************************RAD2DSP.PRO ---  Produces spectrograms
*************************** written by Michael L. Kaiser -- NASA GSFC LEP code 695
openr, 10, /f77_unformatted,'/usr2/data/waves/rad2_s_fluxtable.dat'
cal_data= fltarr(256,256)
readu,10,cal_data
close,10
start:
rad2=lonarr(256)
ymd=0l
hms=0l
yymmdd=0l
status = 0l
fmap=lindgen(256)
read,' Enter YYMMDD :',yymmdd
lz_name='/usr2/data/waves/rad2_19'+strtrim(string(yymmdd),1)$
+'.dat'
openr,1,/f77_unformatted,lz_name
yymmdd=19000000+yymmdd
hour1=' '
hour2=' '
read,' Enter start time in hours [0]',hour1
read,' Enter stop time in hours [24]',hour2
if (hour1 eq '') then begin
        hour1=0
endif else begin
        hour1=float(hour1)
endelse
if (hour2 eq '') then begin
        hour2=24.
endif else begin
        hour2=float(hour2)
endelse
        mhz1=' '
        mhz2=' '
read,' Enter low frequency in MHz [1.075]:',mhz1
read,' Enter high frequency in MHz [13.825]:',mhz2
```

```
if(mhz1 eq '') then begin
        mhz1=1.075
endif else begin
        mhz1=float(mhz1)
endelse
if(mhz2 eq '') then begin
        mhz2=13.825
endif else begin
        mhz2=float(mhz2)
endelse
cspace = ' '
read,' Channel spacing 1 or 4? [1]: ', cspace
if (cspace eq '') then begin
   cspace = 1l
endif else begin
   cspace = 4l
endelse
print, cspace
chan1=fix((mhz1-1.075)/.05)/cspace
chan2=fix((mhz2-1.075)/.05)/cspace
ydim=chan2-chan1+1
av_interval=' '
read,' Enter averaging interval in seconds [90]:',av_interval
if(av_interval eq '') then begin
        av_interval=90
endif else begin
        av_interval=fix(av_interval)
endelse
xdim=fix((hour2-hour1)*3600/av_interval)
array=fltarr(xdim,ydim)
back = 0l
count=fltarr(xdim,ydim)
while not eof(1) do begin
readu,1,ymd,hms,status,rad2
;readu,1, ymd,hms, rad2
if (status eq 1) then begin
  fmap = rad2
  channel = fmap/cspace
  goto, next_record
endif
if (ymd ne yymmdd) then goto, next_record
hour=float(hms-40*(hms/100)-2400*(hms/10000))/3600.
if (hour lt hour1) then goto, next_record
if (hour gt hour2) then goto, plot_data
index=fix((hour-hour1)*3600/av_interval)
if(index gt xdim-1) then goto,plot_data
array(index,channel)=array(index,channel)+rad2
```

```
count(index,channel)=count(index,channel)+1
next_record:
endwhile
plot_data:
close,1
no_zero=where(count ne 0)
array(no_zero)=array(no_zero)/count(no_zero)
for ind = 0, ydim-1 do begin
  backgrounds, array(*,ind), back,1
  array(0:*,ind)=cal_data(ind,array(0:*,ind))/$
  cal_data(ind,back)
endfor
non_zero = where(array ne 0)
array(non_zero) = 10.*alog10(array(non_zero))
scale1 = 0.
scale2 = 50.
nticks = 10
date = yymmdd
hour=findgen(xdim)*av_interval/3600.+hour1
freqlo=findgen(ydim)*.05*cspace+mhz1
colors=indgen(255)
bar=intarr(255,5)
for j=0,4 do begin
 bar(*,j)=colors
endfor
bar2=rebin(bar,510,20)
set_plot,'x'
loadct,18
; colortable 18 = gsfc_color
!p.background=255
!p.color=0
erase
main:
iplt=wmenu(['RAD2 MENU','Screen','Hardcopy','Zoom',$
'New scale','New Day','Quit'],$
title=0,init=1)
; ***** New Plot ***********************************
if(iplt eq 1) then begin
replot:
erase
contour,bar2,position=[.2,.075,.8,.1],$
xrange=[scale1,scale2],xticks=nticks,$
xstyle=1,ystyle=4,xtitle='intensity scale (dB)',/nodata,/noerase
px=!x.window*!d.x_vsize
py=!y.window*!d.y_vsize
sx=px(1)-px(0)+1
sy=py(1)-py(0)+1
```

```
tv,poly_2d(bytscl(bar2),[[0,0],[510/sx,0]],[[0,20/sy],$
[0,0]],0,sx,sy),px(0),py(0)
contour,array,hour,freqlo,position=[.1,.2,.9,.5],$
/noerase,/nodata,xstyle=4,ystyle=4
px=!x.window*!d.x_vsize
py=!y.window*!d.y_vsize
sx=px(1)-px(0)+1
sy=py(1)-py(0)+1
arrayb=bytscl(array,min=scale1,max=scale2,top=254)
tv,poly_2d(arrayb,$
[[0,0],[xdim/sx,0]],[[0,ydim/sy],$
[0,0]],0,sx,sy),px(0),py(0)
contour,array,hour,freqlo,position=[.1,.2,.9,.5],$
/noerase,/data,xstyle=1,ystyle=1,$
xtitle='spacecraft event time (hrs)',xticks=6,$
xrange=[hour1,hour2],yrange=[mhz1,mhz2],title=date,$
ytitle='MHz',ticklen=-.01,/nodata
goto,main
endif
;***** Hardcopy ******************************************
if(iplt eq 2) then begin
jplt=wmenu(['HC MENU','B & W','Color'],title=0,init=1)
set_plot,'ps'
if jplt eq 1 then begin
device,/landscape,bits_per_pixel=8,scale_factor=1.
!p.background=0
!p.color=0
rev=255
endif else begin device,/color,/landscape,bits_per_pixel=8,$
scale_factor=.73
loadct,23
; colortable 23 = iowa_color
!p.background=255
!p.color=0
rev=0
endelse
erase
contour,bar2,position=[.2,.075,.8,.10],$
xrange=[scale1,scale2],xticks=nticks,font=0,$
xstyle=1,ystyle=4,xtitle='intensity scale (dB)',/nodata,/noerase
tv,abs(rev-bar2),!x.window(0),!y.window(0),$
xsize=!x.window(1)-!x.window(0),ysize=!y.window(1)-!y.window(0),/norm
contour,array,hour,freqlo,position=[.15,.2,.85,.5],$
/nodata,/noerase,xstyle=4,ystyle=1,$
xrange=[hour1,hour2],yrange=[mhz1,mhz2],$
ytitle='MHz',ticklen=-.01,font=0
arraybb=bytscl(array,min=scale1,max=scale2,top=254)
```

```
tv,abs(rev-arrayb),!x.window(0),!y.window(0),$
xsize=!x.window(1)-!x.window(0),ysize=!y.window(1)-!y.window(0),$
/norm
contour,arrayb,hour,freqlo,position=[.15,.2,.85,.5],$
/noerase,/nodata,xstyle=1,ystyle=4,xrange=[hour1,hour2],$
xtitle='spacecraft event time (hrs)',font=0,$
yrange=[mhz1,mhz2],title=date
;if (jplt eq 1) then lw
;if (jplt eq 2) then paintjet
set_plot,'x'

loadct,18
!p.background=255
!p.color=0
erase
goto,main
endif
;***** Zoom *****************************************************
if(iplt eq 3) then begin
zoom,Interp=1
goto,main
endif
;***** New Scale ************************************************
if(iplt eq 4) then begin
print,'enter new min and max in dB'
read,scale1,scale2
scale=scale2-scale1
if(scale le 10) then nticks=scale
if((scale gt 10) and (scale lt 20)) then begin
scale=2*fix(scale/2+.9)
scale2=scale1+scale
nticks=scale/2
endif
if(scale ge 20) then begin
scale=10*fix(scale/10+.9)
scale2=scale1+scale
nticks=10
iplt=2
endif
goto,replot
endif
;***** New Day ******************************************
if(iplt eq 5) then goto, start
;***** Quit *****************************************************
if(iplt eq 6) then goto,exit
exit:
end
```

```
;*******************************************************
; Program to compute calibration of backgrounds
; for RAD2 data
; written by M. McCoy -- Iowa State University
;*******************************************************
pro backgrounds, data, back, binsize
back = 01
sum = 01
non_zero = where(data gt 0)
if (non_zero(0) eq -1) then goto, return
n_values = n_elements(non_zero)
hist = fltarr(256)
index = fix(data(non_zero)/binsize)
for i = 0,n_values -1 do begin
  ii = index(i)
  hist(ii) = hist(ii) + 1
endfor
test = n_values/30
for i = 0,255 do begin
  sum = sum + hist(i)
  if (sum lt test) then goto, next
  back = i*binsize
  goto, return
  next:
endfor
return:
return
end
```

A.2 Time series program listing

```
;********Beginning of program**************************
; Program to analyze a signal from particular channel over
; time and produce signal statistics
; written by M. McCoy -- Iowa State University
;*******************************************************
; set all parameters required to read in the data sets
openr,10,/f77_unformatted,'/usr2/data/waves/rad2_s_fluxtable.dat'
cal_data = fltarr(256,256)
readu,10, cal_data
close,10
start:
        rad2=lonarr(256)
        ymd=0l
```

```
        hms=0l
        yymmdd=0l
        status = 0l
        fmap = lindgen(256)
read,' Enter YYMMDD :',yymmdd
lz_name='/usr2/data/waves/rad2_19'+strtrim(string(yymmdd),1)$
+'.dat'
openr,1,/f77_unformatted,lz_name
y1mmdd=yymmdd
yymmdd=19000000+yymmdd
; default times -- select specific times later
        hour1 = 0.
        hour2 = 24.
; default frequencies -- will select specific frequency later
mhz1=1.075
mhz2=13.825
cspace = ' '
read, 'Channel spacing 1 or 4? [1]: ',cspace
if (cspace eq '') then begin
  cspace =1l
endif else begin
  cspace = 4l
endelse
;print, cspace
chan1=fix((mhz1-1.075)/.05)/cspace
chan2=fix((mhz2-1.075)/.05)/cspace
ydim=(chan2-chan1)+1

;********Averaging intervals********************
average_interval:
av_interval=' '
read,' Enter averaging interval in seconds [90]:',av_interval
 if (av_interval eq '') then begin
        av_interval = 90.
 endif else begin
        av_interval = float(av_interval)
 endelse
maxdim=fix((hour2-hour1)*3600./av_interval)
;print, 'xdim = ', xdim
array=fltarr(maxdim,ydim)
back = 0l
count=fltarr(maxdim,ydim)
while not eof(1) do begin
;*******Read in data*****************************
  readu,1,ymd,hms,status, rad2
  if (status eq 1) then begin
    fmap = rad2
```

```
    channel = fmap/cspace
    goto, next_record
  endif
  if(ymd ne yymmdd) then goto, next_record
  hour=float(hms-40*(hms/100)-2400*(hms/10000))/3600.
  if (hour lt hour1) then goto, next_record
  if (hour gt hour2) then goto, time_data
  index=fix((hour-hour1)*3600./av_interval)
  if(index gt maxdim-1) then goto,time_data
  array(index, channel)=array(index,channel)+rad2
  count(index,channel)=count(index,channel)+1
next_record:
endwhile
time_data:
close,1
no_zero=where(count ne 0)
array(no_zero)=array(no_zero)/count(no_zero)
for ind = 0,ydim-1 do begin
   backgrounds, array(*,ind),back,1
   array(0:*,ind)=cal_data(ind,array(0:*,ind))/$
   cal_data(ind,back)
endfor
non_zero=where(array ne 0)
array(non_zero) = 10.*alog10(array(non_zero))

;*********Select desired channel*************
freq:
read,' Enter frequency in MHz [1.075 - 13.875]:', mhz
  mhz = float(mhz)
 chan=fix((mhz-1.075)/.05)/cspace
print, 'Selected Channel # =', chan, ' Out of ',ydim
time_pick:
phour1 = ' '
phour2 = ' '
read, 'Enter analysis start time in hours [0]: ', phour1
read, 'Enter analysis stop time in hours [24]: ', phour2
if (phour1 eq '') then begin
        phour1 = 0.
endif else begin
        phour1 = float(phour1)
endelse
if (phour2 eq '') then begin
        phour2 = 24.
endif else begin
        phour2 = float(phour2)
endelse
pdim = fix((phour2-phour1)*3600./av_interval)
```

```
pstart = fix(phour1*3600./av_interval)
arrayt = fltarr(pdim)
for i =0,pdim-1 do arrayt(i)=array(i+pstart,chan)
arrayt =arrayt+.001
if (min(arrayt) lt .001) then begin
  arrayt(where(arrayt lt .001))=.001
endif
nticks=10
date = yymmdd
chans=string(format='(i3)',chan)
phour=findgen(pdim)*av_interval/3600.+phour1
set_plot,'x'
;******Main plotting routine****************
loadct, 18
; color table 18 = gsfc_color
!p.background=255
!p.color=0
erase
main:
; create menu of choices
iplt=wmenu(['RAD2 MENU','Screen','Hardcopy','Zoom',$
          'New Parameters','Data Analysis','Quit'],$
          title=0,init=1)
if (iplt eq 1) then begin
  replot:
  erase
  plot, phour,arrayt,xtitle='spacecraft event time (hrs)',$
       title=date,ytitle='10 Log W/(m^2 Hz)',$
          subtitle='Channel number '+chans
          goto, main
endif
;*******Hard Copy***************************
if (iplt eq 2) then begin
   jplt=wmenu(['HARD COPY MENU','B&W','Write to file','Go Back'],$
         title=0,init=1)
   if (jplt eq 1) then begin
      set_plot, 'ps'
      device,/portrait,bits_per_pixel=8,scale_factor=1.
      !p.background=0
      !p.color= 0
      rev = 255
   endif
   if (jplt eq 2) then begin
          days  = strtrim(string(y1mmdd),1)
          out_file = days+'_'+chans+'t.dat'
          openw, 2, out_file
       for ii = 0,pdim-1 do begin
```

```
               printf, 2, hour(ii), arrayt(ii)
       endfor
          close,2
          goto, main
   endif
   if (jplt eq 3) then goto, main


;******Now plot data************************
 plot, phour,arrayt,xtitle='Spacecraft event time (hrs)',$
      font=0,ytitle=' 10 log W/(m^2 Hz)',yrange = [0,40.],$
      subtitle='Channel Number '+chans
;         if (jplt eq 1) then lw
;         if (jplt eq 2) then paintjet
 set_plot,'x'
 loadct, 18
 !p.background=255
 !p.color=0
 erase
 goto, main
endif
;******Zoom in on waveform******************
 if (iplt eq 3) then begin
          zoom, Interp=1
          goto, main
 endif

;******Change plot parameters****************
 if (iplt eq 4) then begin
          kplt=wmenu(['PARAMETERS MENU','New Time',$
          'New Frequency', 'New Day'],title=0,init=1)
          if (kplt eq 1) then goto, time_pick
          if (kplt eq 2) then goto, freq
          if (kplt eq 3) then goto, start
endif
;******Data analysis*********************
if (iplt eq 5) then begin
          mplt = wmenu(['DATA ANALYSIS MENU','Autocorrelation',$
       'Crosscorrelation','Histogram'],title=0,init=1)
          if (mplt eq 1) then begin
                    M = fix(pdim/3)     ; range of corr. array
                    rxx  = fltarr(M)    ; autocorrelation array
                    xp = fltarr(pdim)   ; xp = x-avg(x)
                    x1 = fltarr(pdim)
                    x1 = arrayt
                    xim = fltarr(pdim)
                    mx =  total(x1)/n_elements(x1)
```

```
        for i = 0,pdim-1 do xp(i) = x1(i) - mx
        s = total (xp*xp)
        for k = 0, M-1 do begin
         for i = 0, pdim-k-1 do xim(i)= xp(i)*(x1(i+k)-mx)
         rxx(k) = (total(xim))/s
        endfor
        erase
        plot, rxx, xtitle='Correlation lag k',$
         ytitle='Rxx(k)',title=date,$
         subtitle='Autocorrelation of Time Series @ chan '+chans
        ans_plot = ' '
        Read, 'Do you want a hardcopy of this plot [YES]? ',ans_plot
        if (ans_plot eq '') then begin
          set_plot, 'ps'
        device,/portrait,bits_per_pixel=8,scale_factor=1
        !p.background=0
        !p.color=0
        rev = 255
          plot, rxx,xtitle='Correlation lag k',$
          ytitle='Rxx(k)',title=date,$
          subtitle='Autocorrelation of time series @ chan'+chans
          set_plot,'x'
          loadct,18
          !p.background=255
          !p.color=0
        endif
        hard_ans = ' '
        read, 'Do you want to write to file [YES]? ',hard_ans
        if (hard_ans eq '') then begin
         days = strtrim(string(y1mmdd),1)
         name_file=days+'_'+strtrim(chans,2)+'ta.dat'
         openw, 32, name_file
         for ij = 0,M-1 do begin
               printf,32,rxx(ij)
         endfor
         close,32
         goto, main
        endif
  goto, main
endif
if (mplt eq 2) then begin
print,'CROSSCORRELATION OF RAD2 DATA'
ans1= ' '
ans2= ' '
read, 'Perform cross-correlation within the same day [YES]? ',$
   ans1
if (ans1 eq '') then begin
```

```
; cross correlate within same data set at different frequencies
        newfreq= ' '
        read,'Enter frequency to correlate [13.825]: ',newfreq
        if (newfreq eq '') then begin
                newfreq = 13.825
        endif else begin
                newfreq = float(newfreq)
        endelse
        newchan = fix((newfreq-1.075)/.05)/cspace
; read in the other channel data
        arrayc = fltarr(pdim)
        for i = 0,pdim-1 do arrayc(i)=array(i+pstart,newchan)
; now do cross correlation
        M = pdim        ; range of cross corr.
        cxy = fltarr(pdim)
        cimx = fltarr(pdim)
        cimy = fltarr(pdim)
        cim  = fltarr(pdim)
        rxy = fltarr(pdim)        ; cross corr. array
; find sample means and variances
        mx = total(arrayt)/n_elements(arrayt)
        my = total(arrayc)/n_elements(arrayc)
        for ii = 0,M-1 do begin
                cimx(ii) = arrayt(ii)-mx
                cimy(ii) = arrayc(ii)-my
        endfor
        cxx = total( cimx*cimx)
        cyy = total( cimy*cimy)
        for k = 0, M-1 do begin
          for i = 0,M-k-1 do cim(i) = cimx(i)*cimy(i+k)
          cxy(k) = total(cim)
        endfor
        rxy = cxy/sqrt(cxx*cyy)
        plot, rxy,xtitle='correlation lag k',$
          ytitle='Rxy(k)',title=date,yrange=[-1,1],$
        subtitle='Crosscorr. @ chan '+chans+'&'+string(format='(i3)',newchan)
        ans_plot=' '
        read,'Do you want hardcopy? [YES] ',ans_plot
        if (ans_plot eq '') then begin
                set_plot,'ps'
                device,/portrait,bits_per_pixel=8,scale_factor=1.
                !p.background=0
                !p.color=0
                rev = 255
                snewchan = string(format='(i3)',newchan)
                plot, rxy,xtitle='correlation lag k',$
                ytitle='Rxy(k)',title=date,yrange=[-1,1],$
```

```
        subtitle='Crosscorr. @ chan '+chans+' & '+strtrim(snewchan,2)
        set_plot,'x'
        loadct,18
        !p.background =255
        !p.color =0
        erase
        endif
        hard_ans = ' '
        read, 'Do you want to write to file? [YES] ', hard_ans
        if (hard_ans eq '') then begin
                days = strtrim(string(y1mmdd),1)
                name_file=days+'_'+strtrim(chans,2)+'tc.dat'
                openw,33,name_file
                for ij = 0,pdim-1 do begin
                        printf,33,rxy(ij)
                endfor
                close,33
        endif
        goto, main
endif
endif

        if (mplt eq 3) then begin
                read,'Enter binsize for histogram   ', bins
                ; subtract baseline amplitude
                ;arrayb = arrayt
                amp_hist = histogram(arrayt, binsize=bins)
                plot, amp_hist
                goto, main
        endif
endif
;***** Quit *********************************
if (iplt eq 6) then goto, exit
 exit:
 end
```

APPENDIX B

FULL WAVE PROPAGATION METHODS

It is well recognized that the raytracing and phase screen methods used in this research employ a number of approximations. These approximations limit the regions of validity for the analysis. For example, raytracing is simply geometrical optics applied to the ionosphere. As such, the raytracing becomes invalid when the inhomogeneous medium contains gradients on a scale smaller than a wavelength. Similarly, phase screen solutions using the parabolic equation (PE) method also contain approximations which may limit the regions of validity for the solutions. Two very critical assumptions were made in the steps leading from a vector wave equation to the parabolic wave equation: the assumption that polarization coupling was negligible, and that the wave is limited to small-angle, forward scattering. First, the assumption that the polarization coupling term $\left(\nabla(\nabla \cdot \bar{E})\right)$ can be neglected is generally valid when the free space radio wavelength is much smaller than the ionospheric structure scale size. The forward scattering assumption $\left(\partial^2 E/\partial z^2 \approx 0\right)$ also holds when the free space wavelength is smaller than the field correlation length. Numerical simulationshave shown that for modeling applications where the radio wavelength becomes much larger than the structure scale size, the phase screen method will tend to predict smoother, more coherent fields than actually exist.

Full wave methods, which directly solve either the Maxwell curl equations or the vector wave equation for a particular medium representation, encounter no such restrictions, other than those imposed by the discretization of the field components and medium necessary for numerical solutions. The Finite Difference Time Domain (FDTD) technique has recently been extended to solve wave propagation in dispersive media (Nickisch and Franke, 1992;

Nickisch and Franke, 1993). Ultimately, the accuracy is of the numerical simulation is limited only by the grid resolution used.

The FDTD technique has been applied to solve propagation through small ionospehric perturbations. The simulated scattered fields are illustrated in Nickisch and Franke (1992). In these simulations, the total two-dimensional medium studied measured 400 meters × 400 meters. The resolution grid employed for these modeling efforts was $\lambda/16$. For the interference seen by an Earth-orbiting interferometer, the region of interest is that area that would have sources 'visible' to the orbiter. The area is determined by the 'iris' of the ionosphere, i.e., sources located within a certain geographical area that would allow the transmitted signal to reach the satellite. Raytracing simulations have shown the size of this area to be dependent on transmitter frequency, local time, and sunspot number. At HF, in the daytime and with a low sunspot number, the visible sources could be located within ±50° longitude and ±25° latitude of the subsatellite point. The actual field solution must use a three-dimensional representation of the propagation medium (containing the ionosphere), which corresponds to physical dimensions of 9900 km (x) by 19,900 km (y) by 40,000 km (z). If the interference from only a single source is to be modeled, the propagation medium dimensions would depend on the amount of refraction experienced by the wave vector and the radius of the first Fresnel zone of the wave. These quantities would not be known ahead of time without additional raytracing simulations. The minimum resolution step required for the FDTD technique is $\lambda/2$, where λ is the free space wavelength of the field component. At HF the wavelengths under consideration range from about 10 meters to 100 meters. For the physical dimensions of the ionospheric 'section' described here, the resolution cells required would be (at best) 198,000 (x) by 396,000 (y) by 800,000 (z). The FDTD technique, being a time domain technique, also requires a minimum time step to avoid instabilities caused by numerical dispersion. At 3 MHz, the period, T, of the wave is 333 nanoseconds. The minimum time step is T/2, or 166.7 nanoseconds. The total propagation time for an Earth-space transmission is 133 milliseconds; the minimum number of time steps at 3 MHz would be 800,000. If perturbations with scale sizes smaller than one wavelength exist, the resolution grid must be modified accordingly to accurately model the scattering. The Nickisch and Franke FDTD simulations were performed on a MicroVax 3300 and a 25 MHz T800 Transputer (Nickisch and Franke, 1992). The MicroVax required .25 msec/point-step (where one point-step is a single time step at a single grid point); the T800 reduced the time to .16 msec/point-step. A sixteen processor T9000 could reduce the time to 1μsec/point-step. Considering the times required for these machines, a truly large scale simulation is infeasible. 1000-wavelength-square arrays or 50-wavelength cubic arrays could be solved at ten points per wavelength using the Los Alamos National Labs Connection Machine (which has 65,536 parallel processors). At 10 psec/point-step, it would take a Connecttion Machine on the order of a half million hours to solve the FDTD problem for the very large scale required.

Applying Boundary Integral Equation (BIE) methods to large-scale ionospheric propagation is equally problematic. Integral equation methods are commonly applied to electromagnetic scattering problems (Miller, 1988). The problem is one of solving for the fields outside of a penetrable medium (the ionosphere) due sources located on the other side of that medium. The fields due to the interior sources are formulated using the appropriate Green's function for the medium (which may be difficult to calculate for a realistic ionosphere). The integral equations are typically some type of Fredholm integral equation. Their numerical solution requires a conversion of the integral to summations using known weighting fucntions, with the appropriate discretization to both source functions, unknown fields, and weighting functions. The ionospheric propagation medium must again be discretized with a minimum resolution of $\lambda/2$. Given the dimensions and scope of the medium under study, such an approach is inappropriate for the large-scale study of interference breakthrough.

While full wave methods are accurate, they are not yet practical for such a large-scale study of ionospheric propagation. The FDTD technique has proven useful in studying the breakdown of the PE and raytracing approximations for specific cases (see Nickisch and Franke, 1992), but computing power has not developed to the point where it can be applied to model the total interference spectrum and power from HF terrestrial sources.

REFERENCES

Miller, E. K., "A selective survey of computational electromagnetics", **IEEE Transactions on Antennas & Propagation**, Vol. AP-36, No. 9, p. 1281, 1988

Nickisch, L. J., P. M. Franke, "Finite-difference time-domain solution of Maxwell's equations for the dispersive ionosphere", **IEEE Antennas and Propagation Magazine**, Vol. 35 (5), 1992

Nickisch, L. J., P. M. Franke, "Finite-difference time-domain tests of random media propagation theory", **Proceedings of the Ninth Annual Review of Progress in Applied Computational Electromagnetics**, ACES, Monterey, CA, 1993